Doctoral Dissertation

Development of Multifunctional Composite Materials Using Green Tea Extract

(緑茶抽出物を用いた多機能性複合材料の開発)

WEN HANYU

January 2022

Graduate School of Engineering

Osaka University

Contents

General Introduction

Membrane technology has been increasingly applied in diverse industrial processes, for example, water treatment and gas separation[1], the chemical and pharmaceutical industry[2], the food and beverage industry[3], hemodialysis, or textile processing[4] (**Figure 1**). Polymers derived from traditional petro-materials contribute considerably to progressive improvements in the quality of modern life.[5] Many kinds of petroleum-based polymers are used as packaging materials due to their excellent properties such as mechanical capacity, processability, and low price.[6] However, petroleum-based materials present several drawbacks such as being nonbiodegradable and less sustainable, the creation of petroleum-based packaging materials depletes fossil fuels, which also leads to the release of chemicals that further damage the environment. Society becomes increasingly concerned about its impact on the environment, innovations that mitigate the damage done and improve yesterday's methods continue to emerge. One of these innovations is bio-based packaging, which has been received attention and research for its environmental-friendly, biodegradable, and made of materials derived from renewable plant or animal feedstocks. Thus, the use of bio-based packaging is slowly displacing the use of petroleum-based packaging in the industry.[7–9]

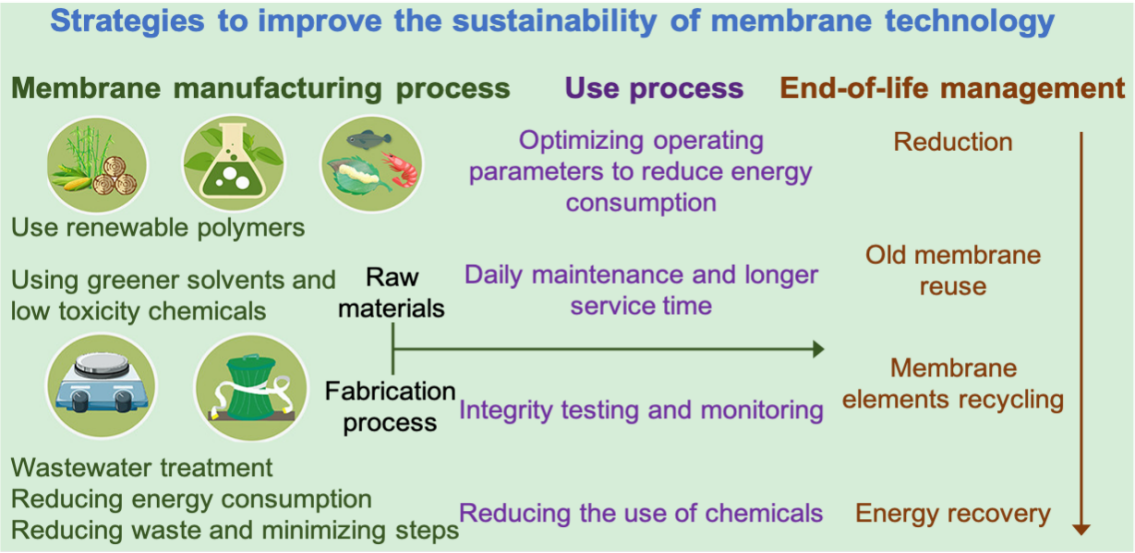

Figure 1. Strategies to improve the sustainability of membrane technology.

At present, renewable and biodegradable biocomposite materials have drawn much

attention as promising green materials in different domains of application such as intelligent food packaging,[10] biomedical and drug delivery,[11] bio-membranes,[12] automotive,[13] as well as in industrial composting applications.[14] The annual production of raw materials from plants and crustacean animal residues offers another common source to produce sustainable biomass materials.[15,16] All this information indicates that these raw materials and their residues are abundant renewable sources around the world for the production of sustainable biomass materials (**Figure 2**). The current review deals with the advances in preparation methods and technical applications of these biocomposites. Nowadays, researchers focus on the modification of polymer and nanomaterials surfaces, via active/bioactive agents targeted for various medicinal and industrial applications. Different biomass materials obtained from renewable resources such as coffee grounds, tea residues, nanocellulose, and date stones are developed to be used as smart reinforcing agents in biodegradable biopolymers for improving their overall properties. Among them, green tea waste is a cheap and abundant biomass source.[17] The amount of world green-tea production in 2015 was 1.8 billion kilograms for consumption[18], and the green-tea waste contains 3.5–7% inorganic components, as well as 93.0–96.5% organic components[19,20].

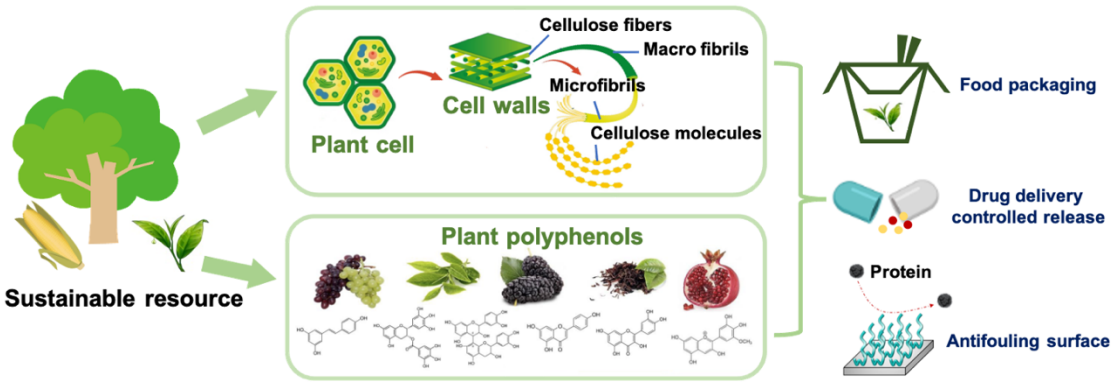

Figure 2. Sustainable Biomass Materials for diverse applications.

The biopolymers such as proteins and polysaccharides, lipids are widely being employed to produce biodegradable and environment-friendly packaging films in the food industry. Biodegradable polymer blending with additives is one of the most effective methods to have new material with desired properties. Furthermore, they may operate as carriers for

incorporating a wide variety of additives, such as antioxidants and antimicrobials agents.[21,22] The increased demand for natural additives has resulted in research based on natural compounds, such as plant extracts which are safe. Since food quality and safety are major concerns in the food industry, the development of biodegradable polymers combined with plant extracts appears as one of the most interesting short-term strategies. Plant extracts have received greater attention as they contain high concentrations of phenolic components that possess strong antioxidant activities.[23,24] Properties of biodegradable films can be affected by the incorporation of plant extracts (**Table 1**). The literature reported that the different components from plant extracts resulted in different types and levels of modification in biopolymers. The extent of changes in techno-functional properties depends on the type and concentration of extract. Films formed by incorporating plant extracts into polymers usually resulted in modified physicochemical, mechanical and barrier, antioxidant and antimicrobial properties compared to films made of individual components and have been used for a wide variety of functions in polymers.[25–27]

Table 1 Effect of plant extracts on techno-functional properties of films.

Type of Extract	Type of Polymer	Elongation at break (%)	Tensile stress (MPa)	Water vapor permeability	Thickness (μm)	Reference
Grapeseed	Grapeseed isolate	-	4.72-10.74	-	33.02-77.89	Sivarooban et al. (2008)[28]
Ginseng	Alginate	19.32-27.95	8.05-22.20	1.72-2.28[a]	70-132	Norajit et al. (2010)[27]
Green tea	Chitosan	54.62-60.73	23.66-28.35	0.09-0.26[b]	-	Siripatrawan (2010)[21]
Grapefruit	Whey protein isolate	24.31-35.80	3.36-26.40	1.42-2.84[c]	-	Lim et al. (2010)[29]
Blueberry	Soy protein isolate	1.29-1.82	2.20-3.53	10.57-15.85[d]	-	Zhang et al. (2010)[30]
Grapefruit	Chitosan	4.72-96.8	8.84-54.9	-	27.9-55.5	Tan et al. (2015)[22]
Green tea	Gelatin	44.62	20.79	1.81[e]	148.00	Li et al. (2014)[29]
Grapeseed		30.86	14.64	2.49[e]	156.67	
Gingko leaf		58.67	15.70	2.62[e]	156.67	

a:($x10^{-7}$gm/m^2dayPa); b:(g mm $m^{-2}d^{-1}$ kPa^{-1}); c:(ng m/m^2sPa); d: (g.m/m^2 h Pa) ($x10^{-5}$); e:(g m/m^2d kPa).

Green tea is one of the most popular and extensively used dietary supplements in the world, it is an evergreen plant that grows primarily in tropical and temperate regions of Asia which mainly include China, India, Sri Lanka, and Japan.[31] It is also cultivated in several African and South-American countries. Diverse health claims have been made for green tea as a trendy ingredient in the growing market for nutraceuticals and functional foods. During the past few decades, the use of natural antioxidants and plant-derived extracts has received increased interest due to concerns over possible adverse health effects caused using synthetic antioxidants. Green tea extract (GTE), a natural source of antioxidants, has been successfully used not only to enhance flavor but also to extend the shelf-life of various food products. GTE is rich in flavanols and their gallic acid derivatives, namely, (+)-catechin (1.4 %), (−)-epicatechin (5.8 %), (+)-gallocatechin (1.4 %), (−)-epicatechin gallate (12.5 %), (−)-epigallocatechin (17.6 %), and (−)-epigallocatechin gallate (53.9 %).[32] GTE can also be used in lipid-bearing foods to delay lipid oxidation and to enhance the shelf-life of various food products. Tea polyphenols, mainly flavonoids, are well-known for their antioxidant properties. The antioxidant activity of green tea polyphenols is primarily attributed to the combination of aromatic rings and hydroxyl groups that assemble their chemical structure and consequently bind and neutralization of lipid-free radicals by these hydroxyl groups. Numerous studies have demonstrated that polyphenols and tea catechins are exceptional electron donors and effective scavengers of physiologically relevant reactive oxygen species in vitro, including superoxide anions, peroxyl radicals, and singlet oxygen.[32–36]

In addition, the plant extraction technique is one of the practical methods that has widely been used for producing metallic nanoparticles (NPs) including silver, iron platinum, and gold.[37,38] NPs and their applications are widely used in the fields of biomedical, pharmaceutical, cosmetic, environmental, and food sectors.[39] Silver is a fascinating material and has been utilized for various day-to-day applications since ancient times. Silver nanoparticles (AgNPs) have been extensively studied due to their superior physicochemical, biological, and antimicrobial properties.[40] Properties of AgNPs primarily depend on their size, shape, distribution, and surface characteristics which can be tuned during green synthesis via

modulating the concentration of reducing agents, stabilizers, metal precursors, and reaction conditions.[41] Green synthesis of AgNPs have growing demands especially in food, biomedical, and therapeutic applications as the process avoids the use of toxic and hazardous synthetic chemicals.[42,43] Amounts of tea polyphenol presented in waste tea extract offer the possibility of direct silver ion reduction because of their strong antioxidant effects.[44] The presence of other organic compounds including caffeine, polysaccharide, and tannic acid allows stabilizing emerging suspensions with no adding other reagents that inhibit the growth of silver agglomerates.[45] Moreover, prepared AgNPs to act as a redox catalyst in the degradation of dyes by electron relay effect between donor and acceptor molecules due to the high surface area.[46,47] AgNPs can demonstrate light absorption and significant visible light catalytic activity due to their narrow bandgap energy to the many colorant/textile combinations under visible or sunlight illumination.[48,49] The high absorption property of Ag-based NPs in the visible light region, together with preventing the recombination of electron and hole pairs within the photocatalytic process, drew enormous attention in the application of silver nanoparticles for the catalytic field (**Figure 3**).

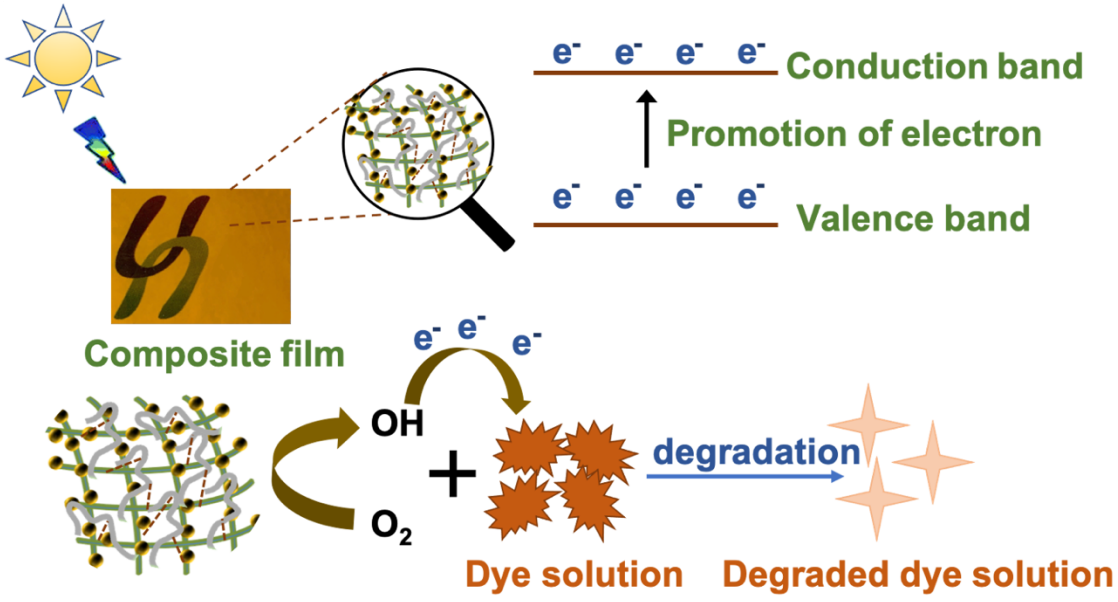

Figure 3. Photocatalytic degradation of various organic dyes using AgNPs.

This aspect of AgNPs makes them an excellent choice for multiple roles in the industrial area.[50] Incorporation of plant-mediated AgNPs into biopolymer-based nanocomposite films and

coatings may lead to improve mechanical, barrier, thermal, and antimicrobial properties of these films.[51] Such improved films and coatings have been evaluated for food packaging applications, and they have been reported to be effective in prolonging the post-harvest life of numerous perishable foods such as fresh produce, dairy, fish, and meat products. Although many methods have been reported plant-mediated AgNPs into biopolymer-based nanocomposite films may lead to improve mechanical and antibacterial activities. In order to ensure the prevention of any toxicity in the packaged food, the potential release of AgNPs from composite in food preservation and the recovery efficiency in photocatalyst degradation test is still needed to be studied.

For obtaining multifunctional properties toward diverse applications, surface modification of composite materials plays a crucial role in modern physical, chemical, biological, and materials science.[52–54] An effective and environmentally benign strategy for tethering functional polymers on various substrates is highly desirable, especially for the introduction of multiple surface functionalities. Most recently, catecholamines (like dopamine) found in mussels, provided the remarkable solution to effectively modify composite surfaces by forming surface-adherent films virtually on any material.[55–57] After polymerization, as a majority of naturally occurring melamine materials, polydopamine (PDA) possesses many striking properties in optics, electricity, and magnetics and most importantly excellent biocompatibility.[58–62] Surface biofouling, which is defined as the undesired adhesion and accumulation of biomolecules and organisms with sizes ranging from nanometer to centimeters,[12,63] has been a persistent problem for centuries. The process of biofouling involves the attachment of a range of micro-and macroorganisms in natural and artificial underwater surfaces, constituting a diverse settled community that causes serious problems and large investments to the maritime industry worldwide.[64,65] To date, surface modification of bifunctional polymer coatings has been proven as an effective strategy for inhibiting or preventing biofouling on substrate surfaces.[66–68] In particular, surface coatings with both antifouling and antimicrobial efficacies exhibit improved antiadhesion performance and increased service life of materials and devices used in the biomedical,[69,70] clinical[71], and maritime fields. Recently, tannic acid (TA), a natural-occurring

polyphenol extracted from green tea, has been investigated as an alternative surface anchor to dopamine or polydopamine.[72–74] TA consists of 15 phenol groups uniformly located on its five arms, which provides sufficient coordination sites for surface anchoring and postmodifications. As such, TA is potentially an ideal and sustainable scaffold for fabricating multifunctional coatings on substrate surfaces. In addition, the stability, durability, and low cytotoxicity of the TA-scaffolded multifunctional composite material suggested the feasibility of its extended applications in aquatic and healthcare environments. Chen et al.[75] reported a universal approach was performed to construct anti-fouling materials surface inspired from tannic acid and zwitterionic polymer (**Figure 4**). This simple preparation of the antifouling surface could be extended to modify various materials' surfaces, even a complex 3D material surface. The chemical long-term stability of antifouling coatings is mandatory and can be greatly improved by terminating end groups on surface-coated polymers with functional group-terminated polymers.[76] Thus, in order to have the antifouling property on the composite surface, polyphenol-terminated polymer graft on the composite materials will provide a new design for functional antifouling films, which would help to better understand antifouling behavior and design more effective antifouling materials and surfaces.

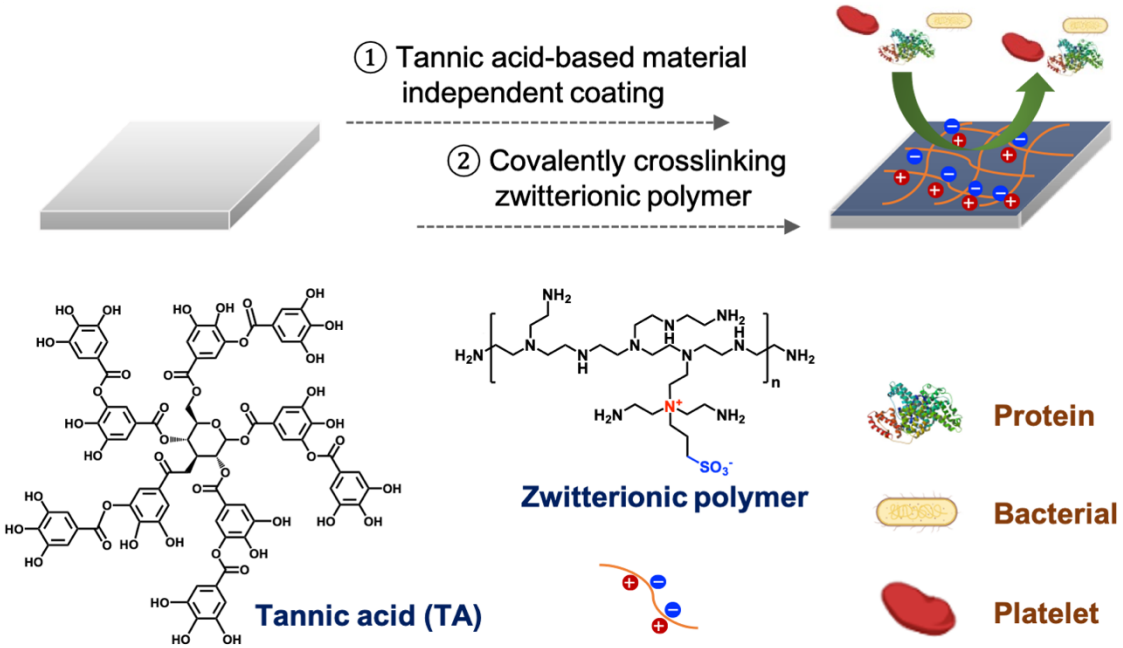

Figure 4. Schematic of the preparation of antifouling surface by TA-inspired approach.

In recent years, oil spills and organic pollutant discharges have posed serious hazards to the marine environment and human health.[77,78] Cellulose-based fabrics have been used as a good oil/water separation material due to their porosity, renewable properties, and excellent flexibility. The researchers focused on studying superhydrophobic surfaces (water contact angle above 150°) taking their inspiration from lotus leaves, geckos, and rose petals in nature. [79-80] Inspired by the strong adhesion of polyphenol and reducing the capacity of free catechol/pyrogallol groups in polyphenol, Bu et al. [81] developed a nature-inspired polyphenol chemistry method to prepare the robust superhydrophobic surfaces for the selective removal of oils or organic solvents from water (**Figure 5**). Sun et al. [82] achieved dual superhydrophobic properties on fabric surfaces using a chemical vapor deposition strategy by coordinating the synergistic effects of hydrophobic and hydrophilic components in the surface chemistry. However, superhydrophobic cellulose-based materials also have some disadvantages. For example, when cotton is subjected to superhydrophobic modification, it is usually susceptible to environmental influences, such as acid and alkali, high temperature, and UV light, which cause the structure of the product to be unstable and affect its long-term use. [83] Tea polyphenol, which has high antioxidant activity, makes the material less susceptible to the influence of ultraviolet light and improves its stability. Therefore, using polyphenols with high antioxidant properties to modify the material surfaces will provide a new design for obtaining superhydrophobic materials with UV-resistant and self-cleaning properties.

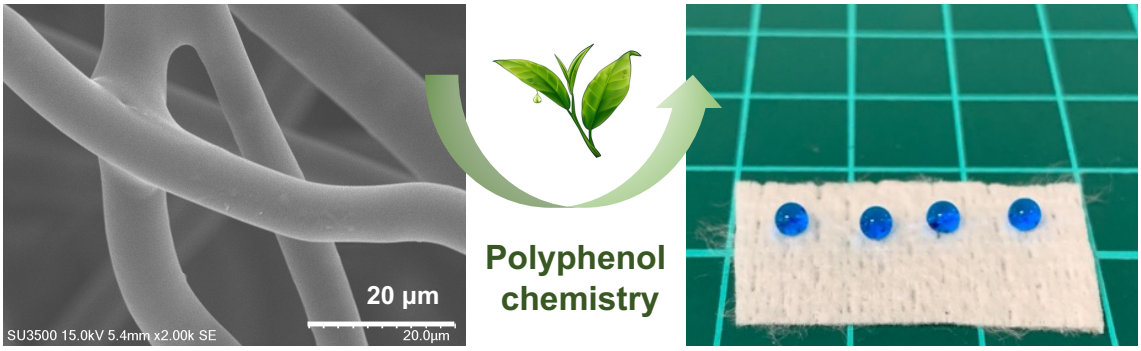

Figure 5. Schematic of the superhydrophobic surface by nature-inspired polyphenol method.

In this thesis, the author aimed the develop efficient strategies for multifunctional

composite materials using green tea extract as antioxidants, reducing agents, and sustainable scaffold. Phenolic compounds are plant-derived ingredients with a variety of biological activities, particularly antioxidant and pH-sensitive properties. Green tea is rich in gallic acid, catechin, and other phenolic compounds, which result in the excellent antioxidant capacity of GTE. In Chapter 1, owing to the good biological activities of GTE, an active food packaging film using GTE biomass compounded with poly(vinyl alcohol) (PVA) has been successfully prepared. In Chapter 2, a simple, one-step green approach was developed for the synthesis and immobilization of AgNPs using GTE, which acted as the reducing agent. Tea cellulose (TC), which was obtained from tea residue, was converted into (TEMPO-tea cellulose) TTC via TEMPO-mediated oxidation that was subsequently employed as a substrate and a stabilizer to immobilize AgNPs onto transparent, flexible composite films. In Chapter 3, a new functional poly(methyl methacrylate) (PMMA) antifouling film has been prepared. The surface of a PMMA film was modified by poly(ethyleneimine) (PEI) and grafted with strongly hydrophilic gallic acid (GA)-terminated poly(2-ethyl-2-oxazoline) (PEtOx-GA). The PEtOx-GA-PEI-S functional film prevented protein adsorption, as demonstrated by water contact angle testing and an adsorption experiment with bovine serum albumin (BSA) protein. These films formed by incorporating plant extracts into polymers in this thesis may guide the future develop sustainable packaging based on biodegradable materials and the polyphenol from plant extract also provides a fresh and universal route to construct antifouling surface applying for multifunctional composite materials. In Chapter 4, a new environmentally friendly material with good ultraviolet light resistance and high oil/water separation efficiency has been obtained. Cellulose non-woven fabric (CNWF), which has high porosity and low cost, has been used as the base material. In order to make the material unaffected by ultraviolet light, the surface of the CNWF was modified with poly(catechin) (pCA). Subsequently, the superhydrophobic material PDMS-pCA@CNWF was obtained by the condensation reaction between modified CNWF (pCA@CNWF) and hydrolysis PDMS, which could play an important role in oil/water separation in the future.

Outline of this thesis

In this thesis, the author aimed at developing efficient methods for multifunctional composite materials using GTE provides a fresh and universal route in diverse applications. This thesis includes 4 Chapters.

Chapter 1

In this Chapter, an active food packaging film using GTE biomass compounded with PVA was successfully developed. The SEM images obtained indicated that PVA, GTE, and glycerol were homogeneously mixed in the GTE-PVA biocomposite films established in this study. The tensile strength and surface hydrophobicity of the biocomposite films was found to increase with an increasing concentration of GTE. The increased concentration of GTE caused a significant reduction in the water solubility, water vapor permeability, and elongation at the break of the established films. The GTE-PVA biocomposite films showed superior UV-vis light barrier properties compared to those exhibited by pure PVA control film. This characteristic may be attributed to the UV absorption ability of the phenolic compounds in GTE, a property that can be used to protect food from UV light. Owing to the abundant phenolics found in GTE, the GTE-PVA biocomposite films showed high levels of antioxidant activity and pH-sensitive abilities.

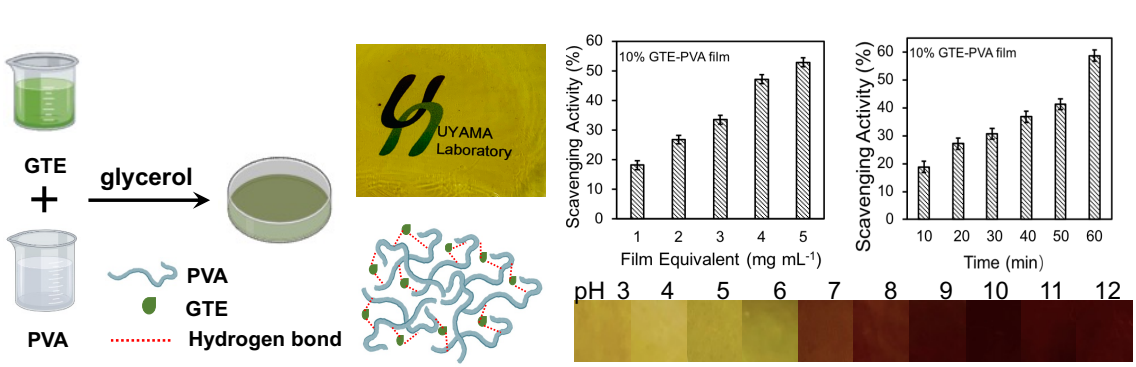

Scheme 1. Schematic of the preparation of pH-sensitive GTE-PVA biocomposite films.

Chapter 2

In this Chapter, a simple, one-step green approach was developed for the synthesis and immobilization of AgNPs using GTE, which acted as the reducing agent. TC, which was

obtained from tea residue, was converted into TTC via TEMPO-mediated oxidation that was subsequently employed as a substrate and a stabilizer to immobilize AgNPs onto the flexible and transparent Ag-TTC-PVA composite film. The Ag-TTC-PVA composite film featured improved mechanical and thermal properties. In addition, the presence of TTC inhibited the fast release of AgNPs from the TTC-derived films, thereby reducing the cytotoxic effects of the AgNPs. Ag-TTC-PVA composite film possessed high antioxidant activity and photocatalytic performance, which is beneficial for decreasing the agglomeration of nanoparticles and simultaneously improving the photocatalytic efficiency.

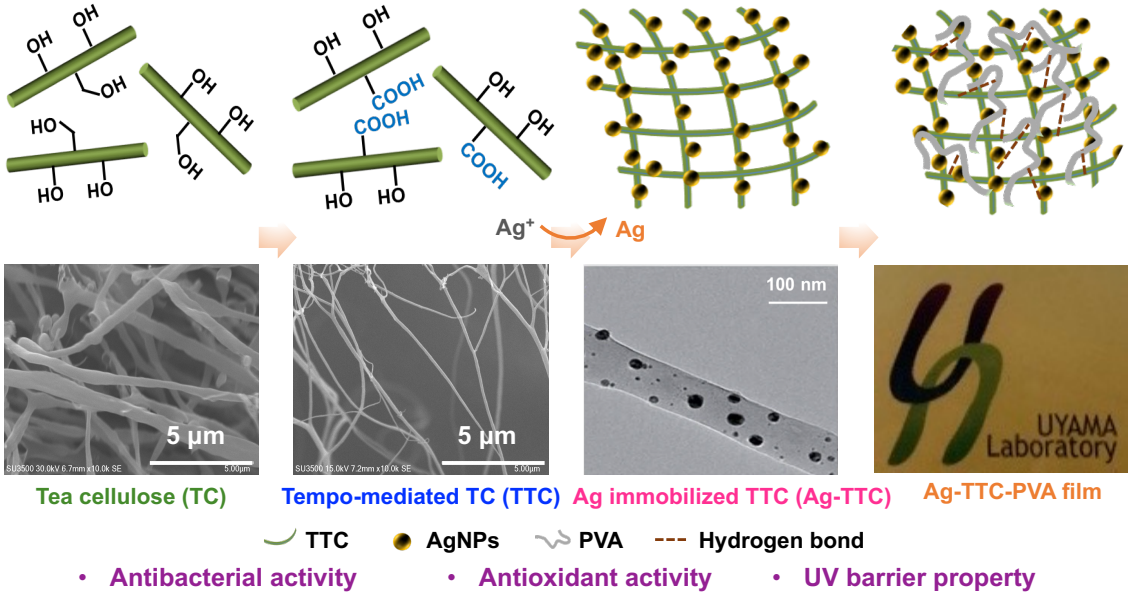

Scheme 2. Schematic of the preparation of Ag-TTC-PVA composite film.

Chapter 3

In this Chapter, a PEtOx-GA-PEI-S functional film with good protein adsorption prevention properties was developed and the functional film was formed by reacting galloyl group modified polymer onto the surface. This new PEtOx-GA polymer was first synthesized via a simple and convenient method for the direct esterification of GA with PEtOx using $Yb(OTf)_3$ as the catalyst. Furthermore, $Yb(OTf)_3$ can be recovered by extracting the reaction mixture with water, and the solvent (CH_3NO_2) can be recycled by distillation and simple drying treatment. The morphology, surface chemical structure, and composition of the PMMA

substrate, PEI-S, and PEtOx-GA-PEI-S functional films were characterized by scanning electron microscopy (SEM), atomic force microscopy (AFM), Fourier transform infrared spectroscopy (FTIR), and X-ray photoelectron spectroscopy (XPS), respectively. The effects of the PMMA substrate, PEI-S, and PEtOx-GA-PEI-S functional films on the adsorption of proteins were also investigated. Therefore, this galloyl group terminated polymer plays a fresh and universal route to construct antifouling surface applying for multifunctional composite materials.

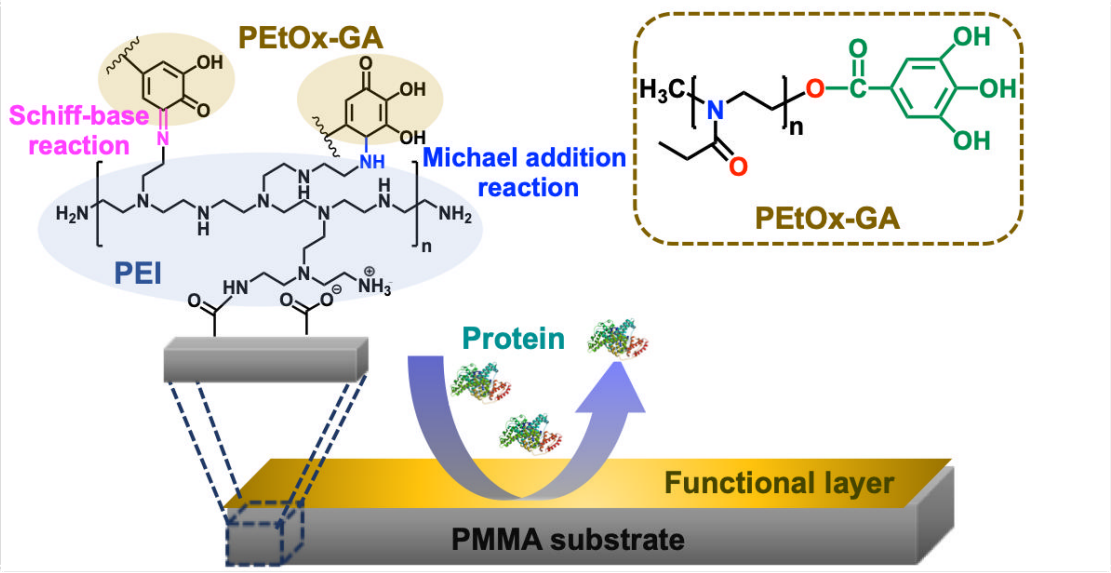

Scheme 3. Schematic of the preparation of antifouling surface by PEtOx-GA-grafted approach.

Chapter 4

In this Chapter, a facile and feasible approach for highly efficient oil/water separation was developed. Owing to the high flexibility, low density, high porosity, and low cost, CNWF is expected to be a promising high-efficiency material. pCA was used to modify the CNWF to be unaffected by ultraviolet light because it has strong antioxidant and antibacterial properties. Subsequently, the superhydrophobic material PDMS-pCA@CNWF was obtained by the condensation reaction between modified CNWF (pCA@CNWF) and hydrolysis PDMS. PDMS-pCA@CNWF with self-cleaning properties enhances UV resistance and is proven as an environmentally friendly material for oil in oil/water mixtures (both light and heavy oils). The morphology, surface chemical structure, and composition of CNWF, pCA@CNWF, and

PDMS-pCA@CNWF were characterized by scanning electron microscopy (SEM), Fourier-transform infrared spectroscopy (FTIR), and X-ray photoelectron spectroscopy (XPS). The separation efficiency and mechanical durability of the PDMS-pCA@CNWF composite were also investigated. This superhydrophobic material could play an important role in oil/water separation in the future.

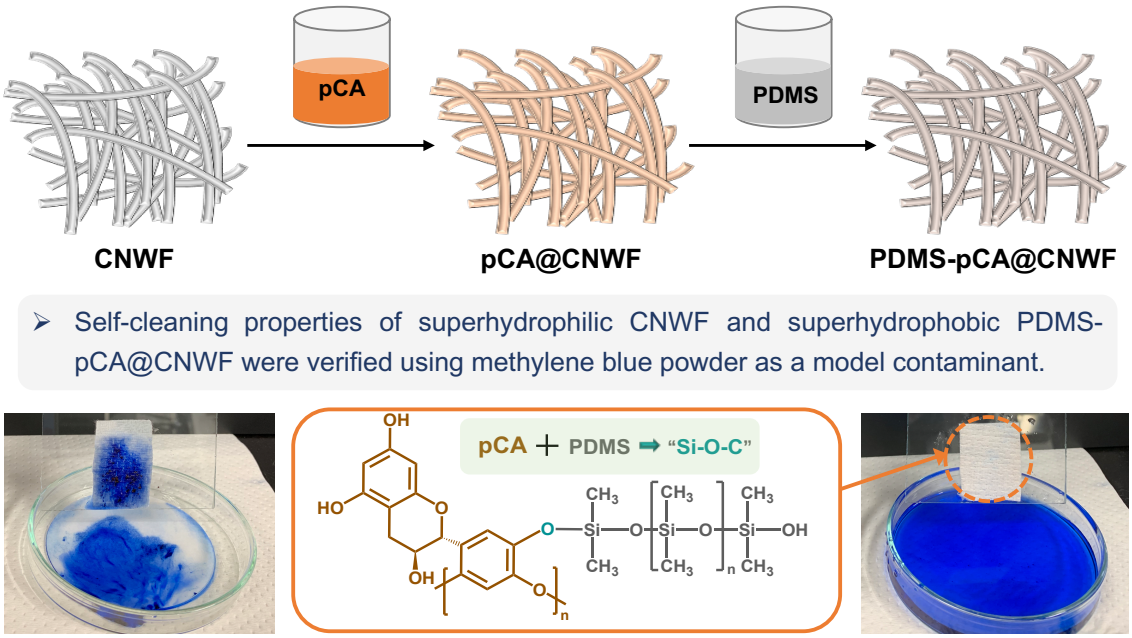

Scheme 4. Schematic of the preparation of superhydrophobic PDMS-pCA@CNWF.

References

1. Y. Zhang, X. Tong, B. Zhang, *J. Memb. Sci.*, 2018, **548**, 32–41.
2. Z. Xu, J. Liao, H. Tang, *J. Memb. Sci.*, 2018, **561**, 59–68.
3. S. Nunes, P. Emecen, M. Ulbricht, *J. Memb. Sci.*, 2020, **598**, 117761.
4. W. Xie, T. Li, J. Crittenden, *ACS Sustain. Chem. Eng.*, 2021, **9**, 50–75.
5. Y. Li, *ACS Biomater. Sci. Eng.*, 2019, **5**, 2079–2092.
6. M. Felix, A. Romero, A. Guerrero, *J. Polym. Environ.*, 2017, **25**, 91–100.
7. K. Goh, F. Zhang, R. Wang, *ACS Appl. Mater. Interfaces*, 2016, **8**, 9994–10004.
8. D. Dehnad, S. Jafari, S. Dadashi, *Carbohydr. Polym.*, 2014, **105**, 222–228.
9. M. Makaremi, M. Lee, S. Milioto, *ACS Appl. Mater. Interfaces*, 2017, **9**, 17476–17488.
10. H. Moustafa, A. Youssef, N. Darwish, *Compos. Part B Eng.*, 2019, **172**, 16–25.
11. K. Monfard, A. Fathi, S. Rabiee, *Int. J. Adv. Manuf. Technol.*, 2016, **84**, 2649–2657.
12. S. Krishnan, C. Weinman, C. Ober, *J. Mater. Chem.*, 2008, **18**, 3405–3413.
13. O. Akampumuza, A. Ahmed, W. Li, *Polym. Compos.*, 2017, **38**, 2553–2569.
14. P. Makvandi, S. Iftekhar, F. Pizzetti, *Environ. Chem. Lett.*, 2021, **19**, 583–611.
15. Y. Chen, J. uan, S. Phang, *Carbohydr. Polym.*, 2016, **151**, 1210–1219.
16. G. Pahla, F. Ntuli, E. Muzenda, *south african J. Chem. Eng.*, 2017, **24**, 168–175.
17. C. Tuck, R. Sheldon, M. Poliakoff, *Science*, 2012, **337**, 695–699.
18. C. Choi, S. Seo, B. Kim, *Sci. Rep.*, 2016, **6**, 1–10.
19. S. Sankar, S. Saravanan, H. Im, *Mater. Lett.*, 2019, **240**, 189–192.
20. C. Peng, X. Yan, J. Lang, *Electrochim. Acta*, 2013, **87**, 401–408.
21. U. Siripatrawan, B. Harte, *Food Hydrocoll.*, 2010, **24**, 770–775.
22. Y. Tan, S. Lim, E. Thian, *Mater. Res. Bull.*, 2015, **69**, 142–146.
23. M. Shah, S. Bosco, S. Mir, *Meat Sci.*, 2014, **98**, 21–33.
24. P. Kanmani, J. Rhim, *Int. J. Biol. Macromol.*, 2014, **68**, 258–266.
25. V. Bifani, C. Ramírez, N. Zaritzky, *LWT-Food Sci. Technol.*, 2007, **40**, 1473–1481.
26. P. Mayachiew, S. Devahastin, *Food Chem.*, 2010, **118**, 594–601.
27. K. Norajit, K. Kim, G. Ryu, *J. Food Eng.*, 2010, **98**, 377–384.

28. S. Min, M. Krochta, in *Improving the safety of fresh fruit and vegetables*, 2005, 454–492.
29. G. Lim, S. Jang, K. Song, *J. Food Eng.*, 2010, **98**, 415–420.
30. C. Zhang, D. Ma, X. Li, *Int. J. food Sci. Technol.*, 2010, **45**, 1801–1806.
31. S. Senanayake, *J. Funct. Foods*, 2013, **5**, 1529–1541.
32. J. Lin, C. Lin, I. Juan, *J. Agric. Food Chem.*, 1998, **46**, 3635–3642.
33. A. Michalak, *Polish J. Environ. Stud.*, 2006, **15**, 4.
34. P. Velayutham, A. Babu, D. Liu, *Curr. Med. Chem.*, 2008, **15**, 1840.
35. Q. Guo, S. Shen, *Biochim. Biophys. Acta-General Subj.*, 1999, **1427**, 13–23.
36. F. najio, T. ishigami, Y. hara, *Biol. Pharm. Bull.*, 1993, **16**, 1156–1159.
37. T. Nakagawa, T. Yokozawa, *Food Chem. Toxicol.*, 2002, **40**, 1745–1750.
38. R. Das, S. Gang, S. Nath, *J Biomater Nanobiotechnol.*, 2011, **2**, 472.
39. M. Nakhjavani, S. Shoja, M. Sarafraz, *Heat Mass Transf.*, 2017, **53**, 3201–3209.
40. H. Chandra, P. Kumari, S. Yadav, *Biocatal. Agric. Biotechnol.*, 2020, **24**, 101518.
41. C. Das, J. Joselin, J. Baalamurugan, *Biocatal. Agric. Biotechnol.*, 2020, **27**, 101593.
42. O. Pryshchepa, P. Pomastowski, B. Buszewski, *Adv. Colloid Interface Sci.*, 2020, 102246.
43. S. Kumar, N. Rajendran, N. Houreld, *Int. J. Biol. Macromol.*, 2018, **115**, 165–175.
44. J. Pulit, M. Zielina, B. Laskowska, *J. Nanomater.*, 2020, **10**, 542.
45. L. Baschir, E, Cosma, I. Creanga, Dig. J. Nanomater. biostructures., 2014, **9**, 847–857.
46. A. Lőrinczi, *Dig. J. Nanomater. biostructures*., 2014, **9**, 847–857.
47. N. Jana, Z. Wang, T. Pal, *Langmuir*, 2000, **16**, 2457–2463.
48. K. Mallick, M. Witcomb, M. Scurrell, *Mater. Chem. Phys.*, 2006, **97**, 283–287.
49. M. Parthibavarman, R. BoopathiRaja, M. Jayashree, *Bionanoscience*, 2019, **9**, 423–432.
50. F. Wang, W. Zhang, *Colloids Surfaces A Physicochem. Eng. Asp.*, 2019, **563**, 31–36.
51. M. Mavaei, Y. Shokoohinia, A. Khoshroo, *Sci. Rep.*, 2020, **10**, 1–12.S.
52. S. Kumar, I. Basumatary, H. Sudhani, *Trends Food Sci. Technol.*, 2021, **112**, 651–666.
53. Q. Wei, T. Becherer, R. Haag, *Angew. Chem. Int. Ed.*, 2014, **53**, 8004–8031.
54. S. Duan, J. Li, T. Hayat, *ACS Sustain. Chem. Eng.*, 2016, **4**, 3368–3378.
55. S. Meyers, M. Grinstaff, *Chem. Rev.*, 2012, **112**, 1615–1632.
56. H. Lee, W. Miller, P. Messersmith, *Science*, 2007, **318**, 426–430.

57. Z. Dong, X. Liu, X. Pei, *J. Mater. Chem. A*, 2014, **2**, 5034–5040.
58. S. Hong, K. Dening, E. Appel, S. Gorb, H. Lee, *Adv. Mater.*, 2014, **26**, 7581–7587.
59. M. Xiao, M. Shawkey, A. Dhinojwala, *ACS Nano*, 2015, **9**, 5454–5460.
60. M. d'Ischia, P. Meredith, T. Sarna, *Angew. Chem. Int. Ed.*, 2009, **48**, 3914–3921.
61. Z. Wang, C. Lau, L. Shao, *ACS Appl. Mater. Interfaces*, 2015, **7**, 9534–9545.
62. Z. Wang, Y. Bai, L. Shao, *J. Mater. Chem. A*, 2015, **3**, 2650–2657.
63. Y. Xu, F. You, H. Sun, *ACS Sustain. Chem. Eng.*, 2017, **5**, 5520–5528.
64. M. Schultz, J. Bendick, E. Holm, *Biofouling*, 2011, **27**, 87–98.
65. M. Callow, J. Callow, *Biologist*, 2002, **49**, 1–5.
66. D. Yebra, S. Kiil, K. Johansen, *Prog. Org. Coatings*, 2004, **50**, 75–104.
67. I. Sawada, Y. Ohmukai, T. Maruyama, *J. Memb. Sci.*, 2012, **387**, 1–6.
68. S. Liu, W. Fan, J. Hedrick, *Adv. Mater.*, 2012, **24**, 6484–6489.
69. C. Weinman, M. Callow, J. Callow, *Langmuir*, 2009, **25**, 12266–12274.
70. M. Lejars, A. Margaillan, C. Bressy, *Chem. Rev.*, 2012, **112**, 4347–4390.
71. W. Cheng, Y. Yang, X. Ding, *Biomacromolecules*, 2015, **16**, 1967–1977.
72. J. Hasan, R. Crawford, E. Ivanova, *Trends Biotechnol.*, 2013, **31**, 295–304.
73. D. Pranantyo, L. Xu, S. Teo, *Biomacromolecules*, 2015, **16**, 723–732.
74. H. Ejima, G. Such, F. Caruso, *Science*, 2013, **341**, 154–157.
75. T. Sileika, P. Messersmith, R. Zhang, *Angew. Chem. Int. Ed.*, 2013, **52**, 10766–10770.
76. S. Chen, Y. Xie, T. Xiao, *Chem. Eng. J.*, 2018, **337**, 122–132.
77. A. Athanassiou, L. Ceseracciu, T. Tran, *Green Chem.*, 2018, **20**, 894–902.
78. B. Duan, H. Gao, M. He, *ACS Appl. Mater. Interfaces*, 2014, **6**, 19933–19942.
79. H. Sai, R. Fu, L. Xing, *ACS Appl. Mater. Interfaces*, 2015, **7**, 7373–7381.
80. L. Zhang, G. Zhou, R. Sun, *Nat. Commun.*, 2021, **12**, 982.
81. X. Tian, T. Verho, R. Ras, *Science*, 2016, **352**, 142–143.
82. Y. Bu, J. Huang, S. Zhang, *Appl. Surf. Sci.*, 2018, **440**, 535–546.
83. Y. Sun, J. Huang, Z. Guo, *Langmuir*, 2020, **36**, 5802–5808.
84. S. Zhao, Y. Liang, Y. Yang, *Nanoscale*, 2021, **13**, 15334.

Chapter 1.

The degradable GTE-PVA biocomposite was developed using green tea extract as antioxidants and pH-indicator

1.1 Introduction

Food packaging is an important part of the food industry. Currently, the majority of food packaging is made from petroleum-based polymers as they are inexpensive and easy to process, and can be produced in large quantities. However, there are serious environmental issues associated with their use, including the depletion of fossil resources and global warming. Therefore, the development of bio-based polymers has recently attracted increasing attention. The biodegradability, non-toxicity, and selective antioxidant properties of composites made from bio-based polymers have been studied for applications in food packaging. Naturally, active films also represent suitable substitutes for use as commercial plastics as they do not cause any inherent food contamination. Moreover, active films, which have biological activities, show good interactions and biocompatibilities with the food, such as increasing the antioxidant activities of certain foods.[1-3] Therefore, active packaging films are being increasingly used to extend the shelf life of food products and monitor food quality.

Phenolic compounds are plant-derived ingredients with a variety of biological activities, particularly antioxidant and pH-sensitive properties. Green tea is rich in gallic acid, catechin, and other phenolic compounds, which result in the excellent antioxidant capacity of a green tea extract (GTE).[4] Siripatrawan et al. reported that chitosan films mixed with GTE showed high levels of free radical scavenging activity.[5] Chitosan is a functional biopolymer with intrinsic antimicrobial and antioxidant properties, which consequently has a high potential for use in biodegradable active packaging. As a source of polyphenols, GTE can be used as an active agent and incorporated into films. Accordingly, this study aimed to develop an eco-friendly active film from chitosan incorporated with an aqueous GTE as a natural antioxidant.

As mentioned above, biodegradable active packaging is the main focus of current food packaging research and development. Recently, poly(vinyl alcohol) (PVA) has been widely

used as a water-soluble film for packaging[6] because of its low cost, good mechanical strength, and biodegradability.[7] This plant extract was incorporated into PVA in order to develop a food packaging film with enhanced strength and antioxidant activity. Owing to the good biological activities of GTE, a combination of GTE and PVA may have a beneficial effect on the biological characteristics of blend films. The use of green tea as a potential natural additive to enhance the antioxidant activity and pH-sensitivity of biocomposite film remains to be studied.

In this study, novel food packaging materials with good mechanical and antioxidant activities were developed. A GTE-PVA biocomposite film was made into a film and characterized. The relationship between the GTE content and the microstructure, physical properties, antioxidant activity, and pH sensitivity of the biocomposite film was investigated. The GTE-PVA biocomposite film was found to be suitable for potential exploitation in the food packaging industry and optimized.

1.2 Experimental Section

1.2.1 Materials

Green tea (500 g) was purchased from Ito En Ltd (Japan). Poly(vinyl alcohol) (PVA) with a molecular weight (Mw) of 14.6 kDa, gallic acid (99%), 2,2-diphenyl-1-picrylhydrazyl (DPPH) reagent, the Folin-Ciocalteu reagent, 2,4,6-Tris(2-pyridyl)-s-triazine (TPTZ), ferric chloride, hydrochloric acid, sodium acetate trihydrate, acetic acid (99%), glycerol, ethanol (99%), sodium carbonate, and potassium persulfate were purchased from Sigma Aldrich (Japan). Deionized water (DI water) and a vent filter for PE Tank (Type 2 Water) were used for solution preparation and dilution. All reagents were of analytical grade and used as received, without further purification.

1.2.2 GTE-PVA composite film preparatio

Green tea leaves (20 g) were immersed in DI water (500 mL) at room temperature for 24 h. The wet green tea leaves were then crushed using a super masscolloider (12 × 100 rpm, 8 times) in water. The resulting dispersion of green tea leaves was freeze-dried for 2 days to obtain the green tea extract (GTE) powder. The total phenol content in GTE was measured using the Folin-Ciocalteu reagent.

PVA powder (4 g) was added to DI water (36 g) and stirred at 90 °C for 12 h to obtain a 10 wt% PVA solution. The PVA solution was mixed with different concentrations (2 wt%, 5 wt%, and 10 wt%) of GTE. Then, 10 wt% of glycerol was added to the GTE-PVA mixture as a plasticizer. The film-forming solutions were poured into Petri dishes, and the GTE-PVA biocomposite films were obtained after oven drying at 50 °C for 2 days.

1.2.3 Characterization.

Fourier transform infrared (FT-IR) measurements of the sample were performed using a Nicolet iS5 spectrometer (Thermo Scientific, MA, USA) equipped with an iD5 ATR attachment. The FT-IR spectra of the GTE-PVA biocomposite films were recorded from 4000 cm^{-1}–400 cm^{-1} at a resolution of 1 cm^{-1} using an FT-IR spectrometer.

Fourier transform infrared (FT-IR) spectra of the TC and TTC fibers were recorded from 4000 to 500 cm^{-1} at a resolution of 1 cm^{-1} using a Nicolet iS5 spectrometer (Thermo Fisher Scientific, MA, USA) fitted with an iD5 attenuated total reflectance attachment. Scanning electron microscopy (SEM) images of the GTE-PVA biocomposite films were captured on a scanning electron microscope (SU3500, Hitachi, Tokyo, Japan) at an accelerating voltage (15 kV). Before analysis, the GTE-PVA biocomposite films were dried, fractured in liquid nitrogen, and coated with a gold layer using an MSP-1S sputter coater (Vacuum Device Inc., Tokyo, Japan). Thermogravimetric analysis (TGA) of the GTE-PVA biocomposite films was performed on a TG/DTA 200 instrument (Exstar, Woodland, CA, USA) by heating from 40 to 640 °C, at a heating rate of 10 °C min^{-1}, under nitrogen atmosphere. The static contact angles of the GTE-PVA biocomposite films were determined using a Drop Master DM300 (Kyowa Interface Science, Saitama, Japan). A digital micrometer (Mitutoyo, Osaka, Japan) with a resolution of 0.001 mm in the range of 0–45 mm was used to measure the thickness of the films. The thickness of each film was measured at 10 random positions, and the average thickness of each film was calculated, as per a previously reported method.[8] A water droplet (1.0 μL) was dropped onto the surface of the GTE-PVA biocomposite films (1 cm × 4 cm), and the contact angle of each film was determined in five different positions at 5 s (scanning time) after the attachment of the droplet in 0 min and after 5 min. The average values have been reported.

The opacity was determined by measuring the absorbance of the GTE-PVA composite film samples (1 cm × 4 cm) at 600 nm with a UV-vis spectrophotometer (U-2810, Hitachi, Tokyo, Japan), according to a previously reported method.[9-11] Eq. (1) was used to estimate the opacity of each film:

$$Opacity = \frac{Abs_{600}}{x} \quad (1)$$

where Abs_{600} is the absorbance of the film samples at 600 nm and x is the film thickness (mm). According to this equation, high opacity values indicate lower transmittance.

Each GTE-PVA biocomposite film was cut into 2 × 2 cm sections and the initial weight was measured. Then, the films were dried at 110 °C for 24 h. The moisture content was

determined by drying the film sample to a constant weight.[12] After obtaining the dry weight, the moisture content (MC) of the film was calculated using Eq. (2):

$$Moisture\ content(\%) = \frac{M_i - M_t}{M_i} \times 100 \quad (2)$$

where M_i *and* M_t are the weights of the film sample before (*i*) and after (*t*) drying.

The GTE-PVA biocomposite films were cut into 2 cm × 2 cm sections and weighed. Then, the film sample was placed in 50 mM sodium phosphate buffer (pH 7) with continuous stirring at room temperature.[13] After 24 h, the undissolved film samples were removed and dried to a constant weight at 110°C. The water solubility (WS) of the film was calculated using Eq. (3):

$$Water\ solubility\ (\%) = \frac{M_d \times (1-\mathrm{MC}) - M_f}{M_d \times (1-\mathrm{MC})} \times 100 \quad (3)$$

where Md and Mf denote the initial and final weights of the film sample, respectively. *MC* denotes the moisture content in the film sample obtained in Eq. (2).

Each GTE-PVA biocomposite film was covered with a test tube (8 cm-depth, 4 cm in diameter), which was then dried in silica gel. The film-covered test tube was weighed and maintained at 20 °C in a desiccator, and the film was weighed every 6 h for 3 consecutive days.[14] The water vapor permeability (WVP) was calculated using Eq. (4):

$$WVP = \frac{\mathrm{W} \times x}{A \times \Delta \mathrm{P} \times \mathrm{t}} \quad (4)$$

where *W* is the weight of the test tube (g), x is the film thickness (m), *t* is the duration (s) of the increased weight of the test tube, *A* is the permeation area of the film sample (m^2), and *ΔP* is the partial vapor pressure at 20 °C (2339 Pa).

The GTE, PVA, and glycerol concentrations were considered as operational variables (denoted as A, B, and C), and the effect on the selected dependent variable, toughness (T), was calculated. The set of experiments followed the Box–Behnken design, a second-order, incomplete, factorial design.[15] The experiment design was statistically analyzed using the Design Expert® 10.0.6 software (Stat-Ease, Inc., Minneapolis, MA, USA). The model was validated through the multifactor analysis of variance (ANOVA). T was calculated as the area under the stress-strain curve per specimen volume, using Eq. (5). The tensile strength (TS) and elongation at break (EAB) of the GTE-PVA composite film were established by tensile testing

of the GTE-PVA composite films performed in a universal testing machine (EZ Graph, Shimadzu, Japan).[16]

$$Toughness = \frac{\text{Energy}}{Volume} \quad (5)$$

$$Tensile\ strength\ (MPa) = \frac{\text{F}}{x \times W} \quad (6)$$

$$Elongation\ at\ break\ (\%) = \frac{\Delta \text{L}}{L_0} \times 100 \quad (7)$$

where F is the stress for film fracture (N), x is the film thickness (mm), W is the film width (mm), and ΔL and L_0 are the elongated and initial lengths (mm) of the film, respectively.

1.2.4 Antioxidant ability of the GTE-PVA composite films

The total phenolic content (TPC) of the GTE-PVA biocomposite films was estimated using the Folin-Ciocalteu reagent reduction associated with a change in color from yellow to blue.[8,17] The GTE-PVA biocomposite films were prepared by soaking in 2.5 mL ethanol and mixed with the Folin-Ciocalteu reagent (0.3 mL, 10% v/v) and 2 mL of 7.5% (w/v) sodium carbonate solution. After 15 min, the absorbance of the mixture was measured using a UV-vis spectrophotometer. Gallic acid (GA) was used as the reference and the standard curve was obtained for 0 ppm-1000 ppm of GA. TPC was calculated as a microgram GA equivalent per unit gram weight of the film.

$FeCl_3$ solution (0.02 M) was mixed with the TPTZ solution (0.04 M, in HCl) and sodium acetate trihydrate solution (pH 3.6) at a 10:1:1 ratio. The FRAP assay solution was incubated at 37°C for 30 min. The prepared ethanol extract of the GTE-PVA biocomposite films (150 µL) was added to the FRAP assay solution (2850 µL). This mixture was incubated for 15 min in the dark. UV–Vis spectrophotometry was performed at 595 nm and the standard curve was obtained using GA as the reference at a concentration of 0 ppm-1000 ppm. The FRAP activity was calculated in terms of a microgram GA equivalent per unit gram weight of the film.

DPPH assay is an easy and rapid method to evaluate the antioxidant content of films.[18] The dose-dependent and time-dependent antioxidant ability of the GTE-PVA biocomposite films was evaluated using the DPPH radical scavenging assay. For dose-dependent antioxidant measurements, different amounts of the GTE-PVA biocomposite films (4 mg, 8 mg, 12 mg, 16

mg, and 20 mg) were added to the DPPH ethanol solution (100 μM, 4 mL). After incubation in the dark for 1.5 h, the absorbance of the reaction solution was measured using an Infinite® 200 (TECAN, Männedorf, Zürich, Switzerland) at 517 nm. For time-dependent antioxidant measurements, the GTE-PVA biocomposite films (20 mg) were added to a DPPH ethanol solution (100 μM, 4 mL). The absorbance of the reaction solution was measured for 10 min, 20 min, 30 min, 40 min, 50 min, and 60 min using an Infinite® 200 (TECAN, Männedorf, Zürich, Switzerland) at 517 nm. The % DPPH radical scavenging activity was calculated using Eq. (8):

$$Scavenging(\%) = \frac{\mathrm{Abs(control)} - \mathrm{Abs(sample)}}{\mathrm{Abs(control)}} \times 100 \quad (8)$$

where Abs (control) and Abs (sample) indicate the absorbance of the blank and the reaction solution, respectively.

1.2.5 pH-sensitivity of the GTE-PVA biocomposite films

To determine the pH response of the GTE-PVA biocomposite film, it was exposed to different buffer solutions (pH 3, 4, 5, 6, 7, 8, 9, 10, 11, and 12) for 30 min. Then, the samples were evaluated using a UV spectrometer (U-2810, Hitachi, Tokyo, Japan) by scanning the sample from 400 nm to 700 nm.

1.3 Results and discussion

1.3.1 FT-IR spectra of the GTE-PVA biocomposite films

The FT-IR spectra of the pure PVA, the GTE, and the GTE-PVA biocomposite films have been shown in **Figure 1-1a**. GTE absorption bands were observed at 1350 cm^{-1}, 1444 cm^{-1}, and 1650 cm^{-1}, in which 1350 cm^{-1} and 1444 cm^{-1} were attributed to a C−H stretching and 1650 cm^{-1} was attributed to a C=C stretching. In contrast, the absorption bands of PVA were observed at 3280 cm^{-1}, 2917 cm^{-1}, 1425 cm^{-1}, 1324 cm^{-1}, and 1081 cm^{-1}.[19] These peaks were attributed to an O−H stretching of the hydroxyl group, CH_2 asymmetric stretching, C=O carbonyl stretching, C−H stretching of CH_2, C−H stretching, C−O stretching of acetyl groups, and C−C stretching. For the GTE-PVA composite film, the hydroxyl stretching region in the range of 3500 cm^{-1}-3000 cm^{-1} and the C−O stretching region in the range of 1300 cm^{-1}-1000 cm^{-1} were relatively sensitive to compositional changes. Notably, some changes occurred in the band position and peak intensity for the GTE-PVA biocomposite films.

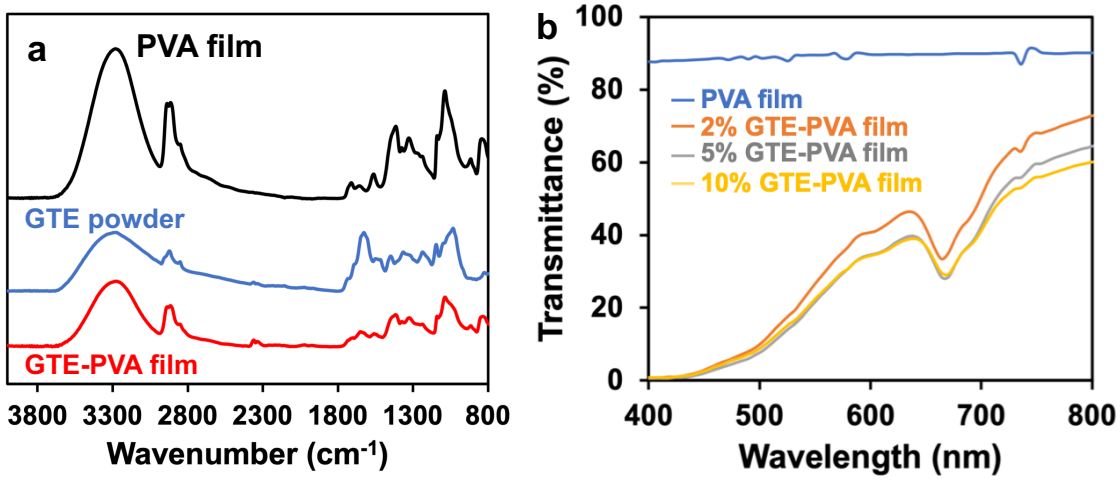

Figure 1-1. (a) FT-IR spectra of pure PVA film, GTE powder and GTE-PVA biocomposite film. (b) UV-vis light transmittance of pure PVA film and GTE-PVA biocomposite films.

1.3.2 Characterization of the GTE-PVA biocomposite films

The UV–vis light barrier property of the film is very important for light-sensitive food packaging. As shown in **Figure 1-1b**, the transmittance around 600 nm was approximately 89.6% for the pure PVA film, 42% for the GTE-PVA composite film containing 2% GTE, 35.4%

for the GTE-PVA composite film containing 5% GTE, and 35% for the GTE-PVA biocomposite film containing 10% GTE. The pure PVA film had almost no barrier to UV light. In contrast, the GTE-PVA biocomposite films showed good barrier properties against UV light because of the UV absorption ability of the phenolic compounds in GTE. Opacity is another index that reflects the transmittance of films. As shown in **Table 1-1**, the opacity of the GTE-PVA biocomposite films was significantly higher than that of the pure PVA film, indicating that the incorporation of GTE decreased the transmittance of the films. This result was following the physical appearance of the films observed in **Figure 1-2**.

Table 1-1 Opacity, Abs_{600}, and thickness of pure PVA and GTE-PVA biocomposite films.

	Abs_{600}	**x (μm)**	**Opacity**
pure PVA	0.04 ± 0.01	72 ± 9	0.6 ± 0.0
2% GTE-PVA	0.13 ± 0.02	76 ± 10	1.8 ± 0.1
5% GTE-PVA	0.23 ± 0.00	84 ± 21	2.8 ± 0.0
10% GTE-PVA	0.29 ± 0.01	85 ± 13	3.4 ± 0.1

Values are given as mean ± standard deviation (SD) (n = 3).

Table 1-2 Thickness, water contact angle (0 min and after 5 min) of GTE-PVA biocomposite films.

Films	**Film Thickness (μm)**	**Contact Angle (deg)**	
pure PVA	72.0 ± 9.0	79.7 ± 2.0	58.2 ± 1.2
2% GTE-PVA	76.0 ± 10.1	87.7 ± 2.1	61.8 ± 1.8
5% GTE-PVA	84.0 ± 21.2	90.8 ± 2.3	75.8 ± 2.0
10% GTE-PVA	85.0 ± 13.1	93.2 ± 1.9	77.0 ± 1.9

Values are given as mean ± standard deviation (SD) (n = 3).

Figure 1-2 shows the surface and cross-sectional microstructure images of the pure PVA film and each GTE-PVA biocomposite film observed by SEM. In general, the surfaces and cross-sections of the films were smooth and uniform, indicating that PVA, GTE, and glycerol were homogeneously mixed.

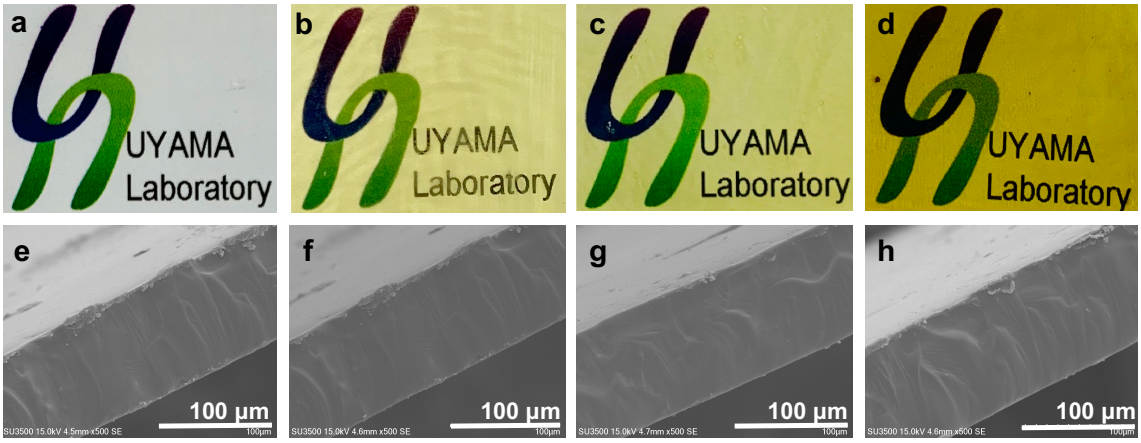

Figure 1-2. Surfaces (a-d) and SEM cross-sections (e-h) of pure PVA film and 2%, 5%, and 10% GTE-PVA biocomposite films.

The thickness of the PVA film and GTE-PVA biocomposite films have been summarized in **Table 1-2**. The thickness of the GTE-PVA biocomposite films significantly increased with an increase in the GTE content. All the GTE-PVA biocomposite films were thicker than the pure PVA control film, and the GTE-PVA biocomposite films containing 10% GTE showed a maximum thickness increment ratio of 15%. The increase in the thickness of the GTE-PVA biocomposite films was caused by the presence of GTE droplets between the PVA polymer chains.

Water contact angle tests were used to determine the hydrophilicity or hydrophobicity of the film surface. The static contact angles of the pure PVA film control film and the GTE-PVA biocomposite films have been summarized in **Table 1-2**. The results indicated that the hydrophobicity of the GTE-PVA biocomposite films increased as the GTE concentration increased. The significant increase in the contact angles of the GTE-PVA biocomposite films was attributed to the inclusion of polyphenolic compounds contained in the GTE, which led to a decrease in the hydrophilicity of the film.

1.3.3 Moisture content, water solubility, and water vapor permeabilit

As shown in **Table 1-3**, compared with the pure PVA film, the biocomposites containing 2%, 5%, and 10% GTE showed a significant reduction in the moisture content. Moreover, the moisture content of the GTE-PVA biocomposite films decreased as the GTE concentration increased. These results indicated that the decrease in moisture content of the GTE-PVA

biocomposite films was due to the inclusion of the hydrophobic components of GTE, which decreased the water absorption capacity of the film.

The water solubility of the pure PVA film and the GTE-PVA biocomposite films has been summarized in **Table 1-3**. It followed the same trend as that observed in the moisture content studies. The GTE-PVA biocomposite films containing 2%, 5%, and 10% GTE showed a substantial decrease in water solubility compared with that exhibited by the pure PVA film. Several studies have reported that strong interactions between phenolic compounds and PVA chains decrease the availability of the hydroxyl groups of the polymer for water interaction.[20,21] Therefore, the decrease in the water solubility of the GTE-PVA biocomposite films indicated a strong cohesion between the GTE and PVA.

Table 1-3 Moisture content, water solubility and water vapor permeability of GTE-PVA biocomposite films.

Films	MC (%)	WS (%)	WVP ($\times 10^{-10} gs^{-1}m^{-1}Pa^{-1}$)
pure PVA	34.1 ± 0.4	32.8 ± 0.8	1.5 ± 0.1
2% GTE-PVA	28.7 ± 0.3	29.1 ± 0.9	1.2 ± 0.2
5% GTE-PVA	25.5 ± 0.3	20.2 ± 0.7	1.0 ± 0.1
10% GTE-PVA	21.7 ± 0.3	13.0 ± 0.8	0.7 ± 0.0

Values are given as mean ± standard deviation (SD) (n = 3).

The WVP value reflects the ability to prevent moisture transfer in films. As shown in **Table 1-3**, the GTE-PVA composite films exhibited lower WVP values than those exhibited by the pure PVA film. Moreover, the WVP value of the GTE-PVA biocomposite films gradually decreased when the GTE content increased from 2 wt% to 10 wt%. The WVP of the active film was also affected by the interaction and uniform distribution of the GTE, temperature, humidity, and plasticizer concentration. In addition, the bulky aromatic in the skeleton of tea polyphenol could obstruct the inner networks of the GTE-PVA biocomposite films and reduce the water vapor affinity of the films. This decrease in WVP values was also reported when chitosan film was incorporated with carvacrol extract and apple polyphenol.[22-24]

1.3.4 Mechanical properties of the GTE-PVA biocomposite films

The response surface describing the effect of the concentration of GTE, PVA, and glycerol on toughness has been shown in **Figure 1-3a**. Increasing the PVA concentration increased the toughness values at lower GTE concentrations, indicating that the functional group of PVA played the role of a plasticizer, that is it enhanced the toughness of the developed GTE-PVA biocomposite films via carboxyl and hydroxyl groups. This behavior demonstrated that the formation between the GTE and PVA chains allowed for the sliding of the polymer chains during the mechanical test, thus improving their ability to absorb energy and plastically deform without fracturing of the GTE-PVA biocomposite films. However, the toughness decreased with an increasing glycerol concentration. A negative effect on the toughness was found for the GTE-PVA biocomposite films when the concentration of glycerol was over 15%, since its interaction with GTE-PVA-glycerol reduced the direct interaction among cellulose chains, reducing the toughness properties.

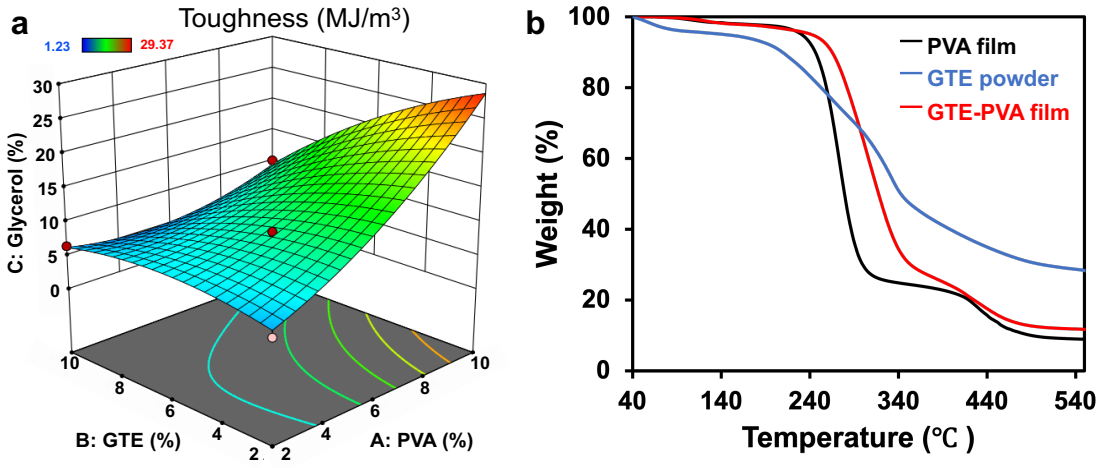

Figure 1-3. (a) Toughness of the GTE-PVA biocomposite films. A: the different contents of PVA (2, 5 and 10%); B: the different contents of GTE (2, 5 and 10%); C: the different contents of glycerol (0, 15 and 30%). The color is the toughness change of the GTE-PVA biocomposite films. (b) TGA curves of the pure PVA film, GTE powder and GTE-PVA biocomposite film.

The tensile strength and elongation at break of the pure PVA control film and the GTE-PVA biocomposite films have been summarized in **Table 1-4**. The GTE-PVA biocomposite films showed higher tensile strength than those exhibited by the pure PVA film. In addition, the tensile strength of the GTE-PVA biocomposite films gradually increased with an increased GTE

content. The increase in the tensile strength of the film containing GTE may be due to the hydrogen bond formed between the hydroxyl groups of the PVA and the polyphenols in the GTE, with similar improvements of the mechanical properties previously observed in the CS-green tea extract films.[5] As shown in **Table 1-4**, the EAB of the GTE-PVA biocomposite film gradually increased with an increased GTE content, indicating that GTE could significantly increase the flexibility of the GTE-PVA composite films.

Table 1-4 Tensile strength and Elongation at break of GTE-PVA biocomposite films.

Films	Tensile strength (MPa)	Elongation at break (%)
pure PVA	24.1 ± 3.1	27.1 ± 3.8
2% GTE-PVA	25.7 ± 3.3	33.3 ± 3.7
5% GTE-PVA	33.7 ± 3.7	40.0 ± 3.2
10% GTE-PVA	40.1 ± 4.0	51.7 ± 3.5

Values are given as mean ± standard deviation (SD) (n = 6).

1.3.5 Thermal properties of the GTE-PVA biocomposite films

Thermal analyses of the GTE-PVA biocomposite films were performed to determine the effect of GTE on the thermal stability and morphology of the polymer. As shown in **Figure 1-3b**, the GTE thermogram showed a broad degradation band that started at 150 °C, with a maximum of approximately 200 °C. Part of the catechin from the GTE was glycosylated, and these sugars were “caramelized” during heating. The partial degradation of the catechins, leading to the formation of gallic acid, and the polymerization of phenols, may also be related to this transition.[25] This degradation was observed over a wide range of temperatures, and the last stage, from 340 °C, was caused by the tea cellulose in GTE. The TGA of the GTE-PVA biocomposite films demonstrated that degradation occurred in three stages. The first stage, within the temperature range of 35 °C–110 °C, corresponded to the dehydration of moisture and physisorbed water molecules on the films. The second stage (110 °C–230 °C) was caused by the tea polyphenols and the main intermolecular hydrogen bonding degradation of PVA. The third stage (230 °C–360 °C) comprised the breakage of tea cellulose and the intramolecular

chain degradation of PVA. The final stage (360 °C–500 °C) comprised the cleavage of the C–C backbone of the PVA polymer and the production of carbon molecules and hydrocarbons. Notably, GTE-PVA film presented relatively lower weight loss than pure PVA film, suggesting the incorporation of GTE could enhance thermal stability.

1.3.6 Antioxidant ability of the GTE-PVA biocomposite films

Tea polyphenols in GTE, such as catechins and gallic acid, show good free radical scavenging activities due to the presence of multiple phenolic hydroxyl groups.[5] Thus, the incorporation of GTE into food packaging films can considerably enhance the antioxidant activity of films to protect food from oxidative damage. Gallic acid, is one of the major phenolic compounds in GTE and can be used as the standard for TPC measurement. As shown in **Figure 1-4a**, TPC has used as a preliminary antioxidant assessment for the pure PVA control film and the GTE-PVA biocomposite films with different levels of GTE content. The result has been attributed to the incorporation of GTE in the film.

The FRAP assay is used to determine the antioxidant activity of films based on their ability to reduce ferric (III) iron into ferrous (II) iron. The GTE-PVA biocomposite films showed a substantial improvement in terms of their iron reduction capacity, with the level of FRAP activity increasing with the increasing GTE levels (**Figure 1-4b**).

The dose-dependent and time-dependent antioxidant abilities of the films have been shown in **Figures 1-4c and 4d**. When the GTE content was increased from 2 wt% to 10 wt% on a PVA basis, the DPPH radical scavenging activity of the GTE-PVA biocomposite film was found to increase gradually. When the film equivalent reached 5 mg mL^{-1}, the DPPH radical scavenging activities of the GTE-PVA biocomposite films containing 2% 5%, and 10% GTE were 32.2%, 39.7%, and 52.9%, respectively. As presented in **Figure 1-4d**, all the films showed time-dependent DPPH radical scavenging activities. The results showed that the GTE-PVA biocomposite films were comprised as follows: 10% GTE > 5 GTE-PVA biocomposite film containing 5% GTE > GTE-PVA composite film containing 2% GTE > pure PVA film.

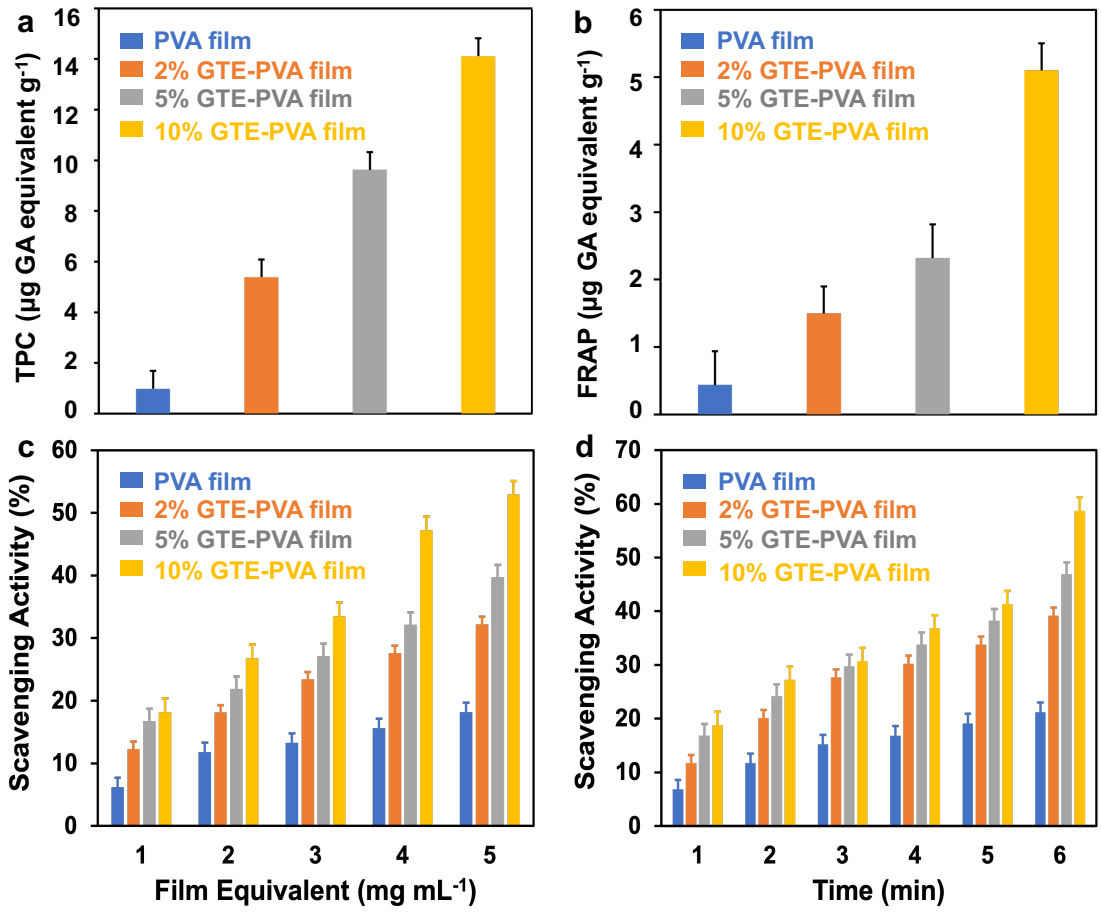

Figure 1-4. Antioxidant assessment of pure PVA film and GTE-PVA biocomposite films: (a) total phenolic content (TPC) (b) ferric reducing antioxidant power (FRAP) activity (c) dose-dependent scavenging activities; (d) time-dependent scavenging activities. Each value represents the mean ± standard deviation (SD) (n = 3).

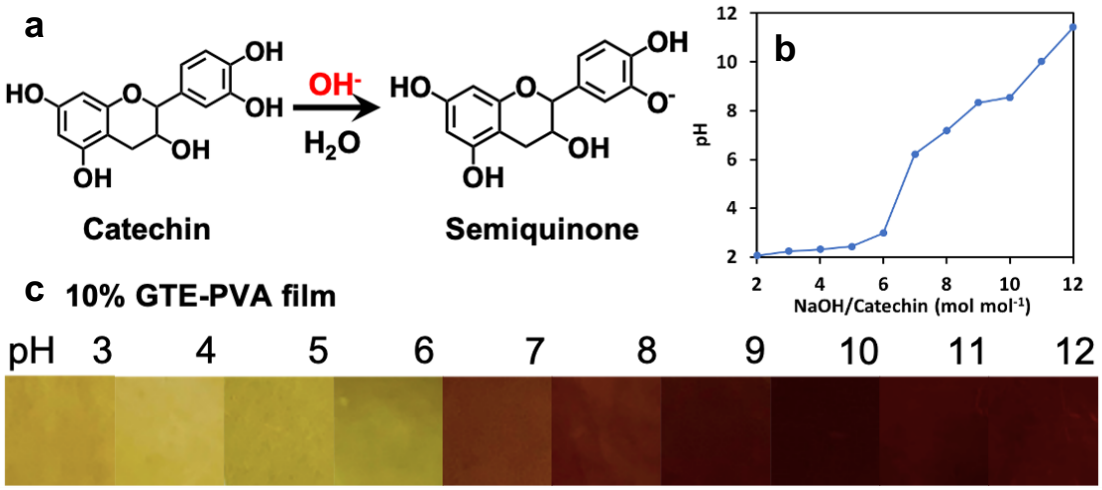

Figure 1-5. (a) Color variations of the irreversible process. (b) NaOH equivalent for different pH values of catechin. (c) Changes in the colors of the 10% GTE-PVA biocomposite film after immersion in different pH solutions.

1.3.7 pH sensitivity of the GTE-PVA biocomposite films

The color was used as an indication of the sensitivity of the GTE-PVA biocomposite films to changes in the pH, due to the structural transformations of tea polyphenols, in which catechin plays an important role. Catechin was converted into semiquinone after immersion in a buffer (pH > 7) (**Figure 1-5a**). At the same time, the color of the GTE-PVA biocomposite films changed to reddish-brown. When the pH of the solution was under 7, the film color (yellowish-green) was almost negligible; however, with an increase in the pH value, the film color became reddish-brown. The pH of the aqueous catechin was acidic and contained many hydroxyl groups, more than that in the GTE. The hydrogen atom of the hydroxyl group was found to have a different dissociation when found at different positions. Therefore, when the pH of the solution was 7, the required NaOH equivalent was greater than 7, such that the color of the GTE-PVA composite films was different from that at pH 7 (**Figure 1-5b**). As shown in **Figure 1-5c,** the pH-sensitive GTE-PVA biocomposite films could be used as pH indicators to monitor the freshness of food products, based on changes in the color of the films.

1.4 Conclusions

In this study, the author developed an active food packaging film using GTE biomass compounded with PVA. The SEM images obtained indicated that PVA, GTE, and glycerol were homogeneously mixed in the GTE-PVA biocomposite films established in this study. The tensile strength and surface hydrophobicity of the biocomposite films was found to increase with an increasing concentration of GTE. The increased concentration of GTE caused a significant reduction in the water solubility, water vapor permeability, and elongation at the break of the established films. The GTE-PVA biocomposite films showed superior UV–vis light barrier properties compared to those exhibited by pure PVA control films. This characteristic may be attributed to the UV absorption ability of the phenolic compounds in GTE, a property that can be used to protect food from UV light.

Owing to the abundant phenolics found in GTE, the GTE-PVA biocomposite films showed high levels of antioxidant activity and pH-sensitive abilities. The antioxidant assessment of the GTE films also confirmed an observable increase in their antioxidant activity compared to those observed in pure PVA films. Considering all the physical and functional properties, the GTE-PVA biocomposite films may be used in the future as a degradable and antibacterial active packaging material in the food industry and beyond.

1.5 References

1. S. Hosseini, M. Rezaei, M. Farahmandghavi, *Food Chem.*, 2016, **194**, 1266–1274.
2. R. Babu, K. O'Connor, R. Seeram, *Prog. Biomater.*, 2013, **2**, 8.
3. J. Barreto, M. Trevisan, W. Hull, *J. Agric. Food Chem.*, 2008, **56**, 5599–5610.
4. U. Siripatrawan, B. Harte, *Food Hydrocoll.*, 2010, **24**, 770–775.
5. S. Tripathi, G. Mehrotra, P. Dutta, *Int. J. Biol. Macromol.*, 2009, **45**, 372–376.
6. G. Perotto, L. Ceseracciu, R. Simonutti, *Green Chem.*, 2018, **20**, 894–902.
7. Z. Adilah, B. Jamilah, Z. Hanani, *Food Hydrocoll.*, 2018, **74**, 207–218.
8. K. Halász, L. Csóka, *Food Packag. Shelf Life*, 2018, **16**, 185–193.
9. P. Park, J. Je, S. Kim, *Carbohydr. Polym.*, 2004, **55**, 17–22.
10. M. Kurek, I. Garofulić, M. Uzelac, *Food Hydrocoll.*, 2018, **84**, 238–246.
11. S. Rivero, M. García, A. Pinotti, *Carbohydr. Polym.*, 2010, **82**, 270–276.
12. V. Rubentheren, T. Ward, C. Chee, *Cellulose*, 2015, **22**, 2529–2541.
13. J. Liu, S. Liu, Q. Wu, *Food Hydrocoll.*, 2017, **73**, 90–100.
14. G. Box, D. Behnken, *Technometrics*, 1960, **2**, 455–475.
15. E. Talón, K. Trifkovic, V. Nedovic, *Carbohydr. Polym.*, 2017, **157**, 1153–1161.
16. A. Adilah, B. Jamilah, M. Noranizan, *Food Packag. Shelf Life*, 2018, **16**, 1–7.
17. J. Liu, C. Meng, C. Jin, *Food Hydrocoll.*, 2017, **63**, 457–466.
18. A. Kharazmi, N. Faraji, R. Hussin, *Nanotechnol.*, 2015, **6**, 529–536.
19. X. Zhang, Y. Shen, W. Prinyawiwatkul, *Food Chem.*, 2013, **141**, 111–116.
20. S. Jang, Z. Xu, Agric. *Food Chem.*, 2009, **57**, 858–862.
21. R. Nazurah, C. Peng, Z. Hanani, *Carbohydr. Polym.*, 2017, **157**, 1479–1487.
22. J. Rubilar, R. Cruz, H. Silva, *Food Eng.*, 2013, **115**, 466–474.
23. L. Sun, L. Chen, Y. Guo, *Carbohydr. Polym.*, 2017, **163**, 81–91.
24. C. Dicastillo, C. Nerín, P. Alfaro, *Food Chem.*, 2011, **59**, 7832–7840.

Chapter 2.

Poly(vinyl alcohol)-based composite film with Ag immobilized TEMPO-oxidized nano-tea cellulose for improving photocatalytic performance

2.1 Introduction

Bio-based packaging has received significant attention owing to its environment friendliness, biodegradability, and green material constituents, which are derived from plants (a renewable resource) or animal feedstocks.[1-5] Particularly, "Tea residue", which is generated from the production of green tea in beverage factories, can be considered as an inexpensive source of biomass, owing to its constituents, such as cellulose and polyphenols.[6] Cellulose-based materials are widely used because of their numerous merits including edibility, biocompatibility, attractive appearance, non-toxicity, non-polluting, and low cost.[7] In recent years, plant extracts have gained considerable attention in the synthesis and capping of metallic nanoparticles (MNPs). These plant extract-based MNPs have been widely used in the biological, environmental, electrochemical, and catalytic fields.

MNPs have received much research attention because of their potential applications in catalytic, biomedical, and bacterial materials owing to their size-dependent optical and chemical properties. For instance, silver nanoparticles (AgNPs) display stronger antibacterial activities than free Ag ions.[8] AgNPs have been reported as a good alternative to develop as an antibacterial agent against multidrug-resistant strains of bacteria.[9] Traditional methods employed for the synthesis of nanoparticles include laser ablation and radiofrequency plasma method.[10-12] Alternatively, plant extract-mediated synthesis of AgNPs can be advantageous when compared with other biological processes as the preservation of cell cultures and aseptic environments is not required.[13] Green tea is a rich source of polyphenolic compounds, and it has been exploited as a natural source for the synthesis of nanoparticles.[14] The water-soluble phytochemicals in green tea are mainly catechins. Therefore, green tea extract (GTE), as a strong antioxidant, can act as a reducing agent for metal ions, leading to the formation and

capping of AgNPs. AgNPs are suggested to play a vital role in exhibiting antibacterial activity. Besides their antibacterial efficacy, AgNPs also show catalytic properties in the field of dye detoxification and its removal. In a study, Kumar et al showed catalytic degradation of a rhodamine dye in the presence of silver and silver chloride nanoparticles biosynthesized using Solidagaltissimoma.[15] AgNPs also have been applied in the catalytic degradation of methylene blue and eosin Y.[16] Due to the high surface area of silver nanoparticles, they exhibit a strong degrading activity on dyes.[17] However, the potential release of AgNPs from composite can limiting their application in food preservation and the recovery efficiency in photocatalyst degradation test. An effective approach to control their release is via the immobilization of MNPs. Specifically, through a 2,2,6,6-tetramethylpiperidine-1-oxyl (TEMPO; T) oxidation process, tea cellulose (TC), extracted from tea residue, can be converted into TTC, which can subsequently be used as a template/immobilization substrate to synthesize and immobilize AgNPs. During this oxidation process, the cellulose fibrils are separated into individual fibrils with minimal aggregation. Such modifications weaken the adhesion between the cellulose fibrils by preventing the formation of strong interfibrillar hydrogen bonds.[18] TEMPO-mediated oxidation is an established pretreatment method for the modification of cellulose, which introduces carboxyl groups into the cellulosic backbone through oxidized primary hydroxyl groups on the cellulose chain. TTC has carboxylic groups, which can chelate metal ions to the cellulose backbone. Therefore, this method can also endow the immobilized AgNPs with functional properties such as antibacterial activity and photocatalyst degradation property.

In this study, a simple, one-step green approach was developed for the synthesis and immobilization of AgNPs using GTE, which acted as the reducing agent. TC, which was obtained from tea residue, was converted into TTC via TEMPO-mediated oxidation that was subsequently employed as a substrate and a stabilizer to immobilize AgNPs onto transparent, flexible composite films. The morphology, physicochemical and mechanical properties, optical transmittance, the cumulative rate of release of Ag from the films, and the antioxidant activity were investigated. Finally, the photocatalytic degradation of methyl orange (MO) was investigated in the presence of the Ag-TTC-PVA composite film.

2.2 Experimental Section

2.2.1 Materials

Green tea was purchased from Ito En Ltd. (Tokyo, Japan). Poly(vinyl alcohol) (PVA, Mw = 14,700 g mol^{-1}), DPPH reagent, NaOH, TEMPO, NaBr, NaClO (500g, Mw: 74.44 g mol^{-1}), and Na_2CO_3 were purchased from Sigma-Aldrich (Tokyo, Japan). Methyl orange (MO) was purchased from Fujifilm Wako Pure Chemical Corporation (Tokyo, Japan). Deionized water (DI water) was used for solution preparation and dilution. All reagents were of analytical grade and used as received without further purification.

2.2.2 Preparation of TC fibers

To extract TC, 20 g green tea was treated with 400 mL DI water at 90 °C for 2 h. The insoluble residue was first subjected to a degreasing treatment using petroleum ether at a ratio of 1:10 (g mL^{-1}) for 2 h, followed by a depigmentation process with acetone at a ratio of 1:10 (g mL^{-1}) for 2 h under magnetic stirring. The residue was then delignified with $NaClO_2$ solution (pH 4.0) at a ratio of 1:20 (g mL^{-1}) at 75 °C for 2 h. After filtration and washing with distilled water, the residue was mixed with NaOH solution (10%, w/v) at a ratio of 1:20 (g mL^{-1}) for 10 h at room temperature to remove hemicellulose.[19] Christopher L. et al. report that hemicellulose and cellulose decompose over different temperature ranges; generally, hemicellulose decomposes at a lower temperature range (220–315 °C) than cellulose (300–400 °C).[20] The residue was then washed with distilled water and ethanol (95%, v/v) until the filtrate turned neutral. TC fibers were obtained after drying at 60 °C for 24 h. Tea residues are rich in cellulose, hemicellulose, lignin, theanine, tea protein, tea polyphenols, tea polysaccharides, caffeine, tea pigments, tea saponins, vitamins. Among them, cellulose contained 13%-19% cellulose of its dry weight.[21,22] In this research, the mass percentage of TC extracted from tea residues using the above process was about 18.5%.

2.2.3 Preparation of TTC nanofibers

The TTC nanofibers were prepared as follows: 4 g TC fibers were suspended in 400 mL

DI water containing 0.075 g TEMPO and 0.75 g NaBr. Next, the total volume (20 mL, 0.14 mol L^{-1}) of NaClO was directly added to the mixture under continuous stirring. The pH of the reaction mixture was maintained at 10.5. The color of the mixture changed to pale yellow and finally to white after the reaction was complete. The obtained suspension was treated by centrifugation at 4,000× g several times. After a thorough wash with DI water, until the pH reached 7, the TC fibers were mechanically treated for 30 min using a blender to disperse the cellulose into individual nanofibers (TTC) and then concentrated under a vacuum to obtain a concentrated TTC suspension, which was stored at 4 °C until further use.

2.2.4 Preparation of AgNPs using GTE

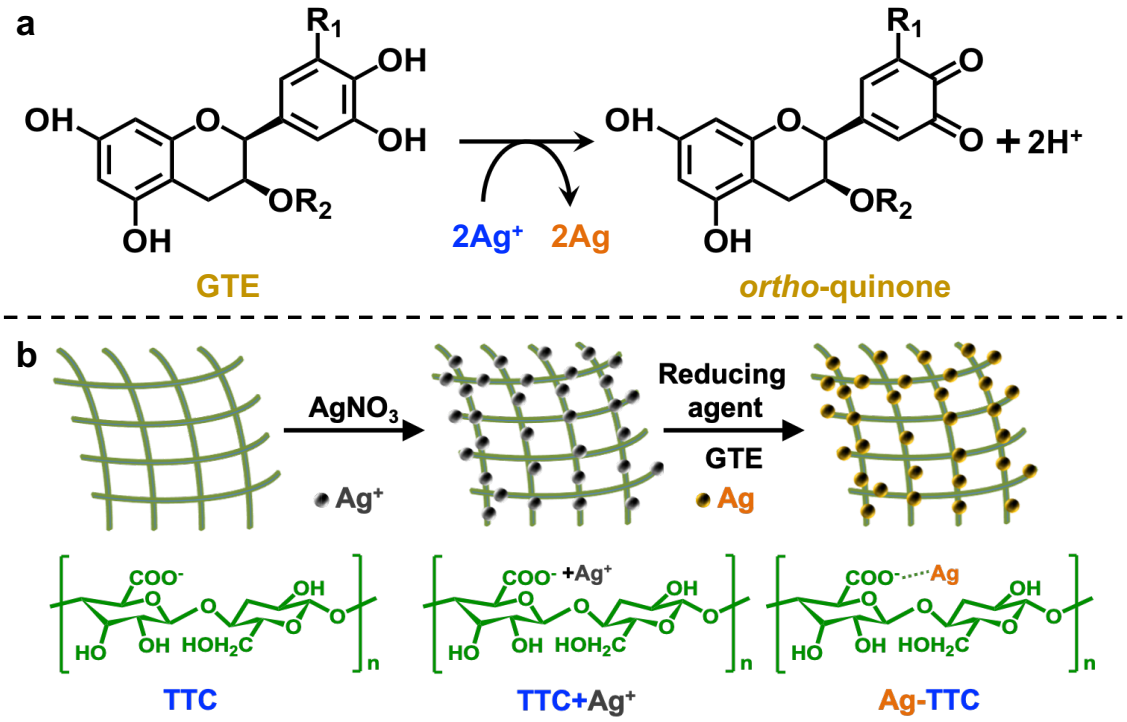

Scheme 2-1. (a) Synthesis of AgNPs using the aqueous extract of green tea (GTE). (b) Preparation of TTC-mediated immobilized AgNPs.

For the synthesis of AgNPs using GTE as a reductant, $AgNO_3$ in DI water was used as the source of Ag^+, and a typical reaction mixture consisted of 10 mL GTE (1 mg mL^{-1}) in 90 mL $AgNO_3$ solution (10 mM). The suspension was stirred for 15 min at room temperature for the reduction of Ag^+ to Ag until the color of the mixture became reddish-brown, indicating the

formation of AgNPs. The suspension was centrifuged at 90,000× g for 30 min, and the precipitated AgNPs were washed and freeze-dried.

2.2.5 Preparation of immobilized AgNPs

AgNPs were obtained as Rolim WR, et. al. reported [23] (**Scheme 2-1a**, introduced in the SI in detail). The immobilization of AgNPs on TTC (Ag-TTC), which was used as the template substrate, was performed as follows. TTC nanofibers (0.1 g) were dispersed in 40 mL DI water under stirring for 10 min after which 5 mL $AgNO_3$ solution (10 mM) was added under continuous stirring for another 10 min. Subsequently, 3 mL GTE (1 mg L^{-1}) was added dropwise, and the mixture was allowed to react at room temperature for 1 h to obtain Ag-TTC dispersion (**Scheme 2-1b**). Free (i.e., non-immobilized) AgNPs were also prepared using GTE but in the absence of TTC.

2.2.6 Preparation of TTC-PVA and Ag-TTC-PVA composite films

Ag-TTC-PVA composite film was prepared via a casting solvent evaporation technique. TTC nanofibers were dispersed in ultrapure water to prepare a 1% (w/v) TTC dispersion. The TTC dispersion was then mixed with Ag-TTC (2.0% w/$w_{\mathbf{TTC}}$), 10% (w/w) PVA, and 10% (w/w) glycerol and stirred for 2 h. Under 45 °C, the above solution was poured into Petri dishes and subsequently allowed to dry for 24 h. TTC-PVA film was also prepared similarly, however, in the absence of Ag-TTC. In addition, TTC with no immobilized AgNPs was prepared by solution casting of TTC with no immobilized AgNPs.

2.2.7 Characterization

The crystallinity of the prepared samples was determined by X-ray diffraction (XRD) on a D500 diffractometer (SmartLab, Rigaku, Tokyo, Japan) with Cu Kα radiation. Diffraction peaks were measured from 5 to 90° at a rate of 5° min^{-1}. The grain size and distribution of AgNPs in TTC were investigated by transmission electron microscopy (TEM; JEOL JEM-2010, Tokyo, Japan) at an accelerating voltage of 100 kV. Fourier transform infrared (FT-IR) spectra of the TC and TTC fibers were recorded from 4000 to 500 cm^{-1} at a resolution of 1 cm^{-1} using a Nicolet iS5 spectrometer (Thermo Fisher Scientific, MA, USA) fitted with an iD5 attenuated

total reflectance attachment. Scanning electron microscopy (SEM) images of the TTC-PVA and Ag-TTC-PVA composite films were captured on a scanning electron microscope (SU3500, Hitachi, Tokyo, Japan) at an accelerating voltage (15 kV).[24] Before analysis, the TTC-PVA, and Ag-TTC-PVA composite films were dried, fractured in liquid nitrogen, and coated with a gold layer using an MSP-1S sputter coater (Vacuum Device Inc., Tokyo, Japan). The chemical surface composition of the TTC-PVA and Ag-TTC-PVA composite films was determined by X-ray photoelectron spectroscopy (XPS; JEOL JPS-9010MC, Tokyo, Japan).[25] Survey (75 W) and narrow (150 W) XPS patterns were recorded using a monochromatic Al Kα X-ray source and at fixed analyzer pass energies of 160 and 10 eV, respectively. CasaXPS Version 2.3.15 software was used for peak differentiation and fitting analysis of the C 1s narrow XPS spectra. Thermogravimetric analysis (TGA) of the TTC-PVA and Ag-TTC-PVA composite films was performed on a TG/DTA 200 instrument (Exstar, Woodland, CA, USA) by heating from 40 to 640 °C, at a heating rate of 10 °C min^{-1}, under nitrogen atmosphere.

The degree of oxidation (DO) was expressed as the ratio between the amount of oxidized hydroxymethyl groups and total hydroxymethyl groups, which was determined by conductimetric titration. A 50 mg cellulose sample was suspended/dissolved into 15 mL of 0.01 mol L^{-1} hydrochloric acid solutions. After 10 min of stirring, the suspension was titrated with 0.05 mol L^{-1} NaOH solution under stirring. The conductivity was monitored using a conductivity meter throughout the titration process. The titration was terminated when the pH reached 10.5. DO was calculated by the following equation [26,27]:

$$DO = \frac{162\times \mathrm{C}\times(V_2-V_1)}{\mathrm{m}-36\times \mathrm{C}\times(V_2-V_1)} \times 100\% \quad (1)$$

where C is the NaOH concentration (mol L^{-1}), V_1 and V_2 are the volume of NaOH (L), and m is the weight of the dried sample (g).

The water solubility (WS) of the TTC-PVA and Ag-TTC-PVA composite films was assessed as follows.[28] The films were cut into 2 cm × 2 cm sections and weighed. They were then placed in 50 mL DI water under continuous stirring at room temperature. After 24 h, the residual films (undissolved films) were retrieved and dried to a constant weight at 110 °C. The WS of the film was calculated using Eq. (2):

$$\text{Water solubility (\%)} = \frac{M_i \times (1-\text{MC}) - M_f}{M_i \times (1-\text{MC})} \times 100 \quad (2)$$

where M_i and Mf denote the initial and final weights of the film sample, respectively, and MC is the moisture content of the films.

The light transmittance of the films was assessed on a UV–vis spectrophotometer (U-2810, Hitachi, Tokyo, Japan) according to a previously reported method.[29] The film samples were scanned in the range of 200–800 nm.[30,31] The total color difference (ΔE) and whiteness index (WI) were calculated using Eqs. (3) and (4), respectively:

$$\Delta\text{E} = \sqrt{(L^* + L)^2 + (a^* - a)^2 + (b^* - b)^2} \quad (3)$$

$$\text{WI} = 100 - \sqrt{(100 - L)^2 + a^2 + b^2} \quad (4)$$

where L, a, and b represent the color values of the film samples determined from a CR-10PLUS colorimeter (Satoshoji Corporation, Osaka, Japan). L^* refers to the lightness, a^* is the red/green coordinate, and b^* is the yellow/blue coordinate; specifically, L^* (94.3), a^* (−0.3), and b^* (−0.6) are the color values of a standard white plate.

The tensile strength (TS) and elongation at break (EAB) of the films were determined as follows. The dry films were cut into specimens of size 20 mm × 5 mm and immersed in water for 2 h. The tensile test of the films was performed on an EZ Graph universal testing machine (Shimadzu Corporation, Kyoto, Japan) using a 10 N load cell for the wet films or a 100 N load cell for the dry films and a strain rate of 10 mm/min. Measurements were taken at five different positions on each film and the average value was calculated. The TS and EAB were calculated using Eqs. (5) and (6), respectively, as follows:

$$\text{TS (MPa)} = \frac{F}{xW} \quad (5)$$

$$\text{EAB (\%)} = \frac{\Delta L}{L_0} \times 100 \quad (6)$$

where F is the stress for film fracture (N), x is the film thickness (mm), W is the film width (mm), and ΔL and L0 are the elongated and initial lengths (mm) of the film, respectively.

The dose-dependent and time-dependent antioxidant activities of the TTC-PVA and Ag-TTC-PVA composite films were evaluated using the DPPH radical scavenging assay. For the

dose-dependent antioxidant measurements, different amounts of the TTC-PVA or Ag-TTC-PVA film (2.5, 5, 7.5, 10, 12.5, and 15 mg) were added to DPPH ethanolic solution (100 μM, 4 mL). After incubation in the dark for 1.5 h, the absorbance of the reaction solution at 517 nm was measured on an Infinite 200 plate reader (TECAN, Männedorf, Zürich, Switzerland). For the time-dependent antioxidant measurements, the TTC-PVA or Ag-TTC-PVA composite film (15 mg) was added to the DPPH ethanolic solution (100 μM, 4 mL). The absorbance of the reaction solution at 517 nm was measured for 10, 20, 30, 40, 50, and 60 min on an Infinite 200 plate reader. The percentage DPPH radical scavenging activity was calculated using Eq. (7):

$$\text{Scavenging (\%)} = \frac{\text{Abs(control)} - \text{Abs(sample)}}{\text{Abs(control)}} \times 100 \quad (7)$$

where Abs(control) and Abs(sample) indicate the absorbance of the blank and the reaction solution, respectively.

2.2.8 Cumulative release studies of AgNPs

To examine the stability and release behavior of AgNPs from the Ag-TTC-PVA composite film, non-immobilized AgNPs and immobilized AgNPs film was immersed in a 5 mL buffer solution at pH 7 at 25 °C.[32] After 24 h, 0.5 mL media was withdrawn, and fresh media was added to maintain the initial conditions. The samples were then added to 4.5 mL H_2SO_4 (0.5 mol L^{-1}), and the volume after dilution was 5 mL. The Ag content was determined by inductively coupled plasma optical emission spectroscopy (LTQ Orbitrap XL, Thermo Fisher Scientific, MA, USA).

2.2.9 Photocatalytic activity

The photocatalytic activities of composite films were assessed by degrading an MO solution under the UV LED lamp (λ = 365 nm, 100 mW cm^{-2}, PiPhotonics, Inc. HLKK60). In this experiment, 100 mg of a composite film was added to a beaker containing 50 mL of MO solution (10 mg L^{-1}). Before turning on the light, the mixture was stirred in the dark for 30 min to establish adsorption-desorption equilibrium between MO and the composite films. During UV irradiation, the residual concentration of MO at its maximum absorption wavelength (465 nm) was determined by UV–vis spectroscopy for every 10 minutes. The MO solutions with

immersing TTC-PVA and Ag-TTC-PVA composite films were analyzed under the same conditions. A blank degradation test without photocatalyst was also analyzed to explore the self-degradation of MO.

$$\text{Degradation efficiency } (\%) = \frac{C_0 - C_t}{C_0} \times 100 \quad (6)$$

where C_0 and C_t represented the concentration of dyes before and after degradation, respectively.

2.3 Results and discussion

2.3.1 FT-IR and Microstructure of TC/TTC powder

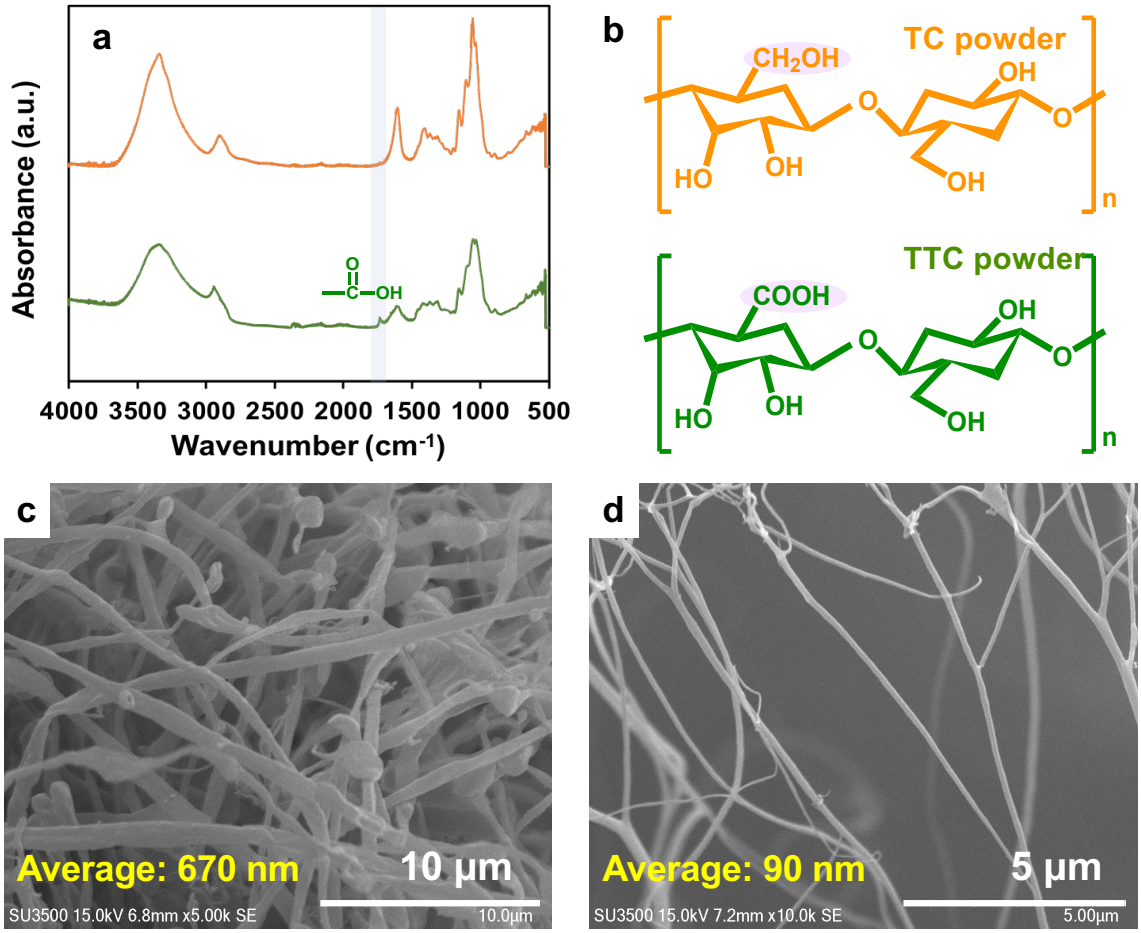

Figure 2-1. (a) FT-IR spectra and structures of TC and TTC fibers. A magnified view of the spectrum in the range of 2000–1200 cm^{-1} is shown. SEM images of (b) TC fibers and (c) TTC nanofibers.

The difference in the functionality of the TC fibers before and after TEMPO-mediated oxidation was assessed by FT-IR spectroscopy. As shown in **Figure 2-1a**, before oxidation, the FT-IR spectrum of the TC fibers featured typical characteristics of natural cellulose, confirming the absence of carboxylate groups. The peaks at 3300 cm and 1056 cm^{-1} were attributed to the O–H stretching vibration and the C–O bond of cellulose, respectively, and the peaks at 2917 and 1395 cm^{-1} were attributed to C–H stretching and bending of $–CH_2$ groups, respectively. The peak at 1600 cm^{-1} was attributed to H–O–H stretching vibration of absorbed water in the carbohydrate. After acidification of the oxidized TC, the stretching mode of the C=O functional

group appeared at 1700 cm^{-1} (carboxylic acid groups). The presence of this new peak in TTC indicates the successful oxidation of the TC fibers via the TEMPO process. The Degree of oxidation (DO) of the obtained TTC was 5.18 %. **Figures 2-1c** and **2-1d** respectively show SEM images of the TC and TTC fibers. The average size of the TC fibers (670 nm) reduced to ~90 nm after the TEMPO-mediated oxidation process, confirming the successful formation of TTC nanofibers.

2.3.2 Characterization of TTC@AgNPs

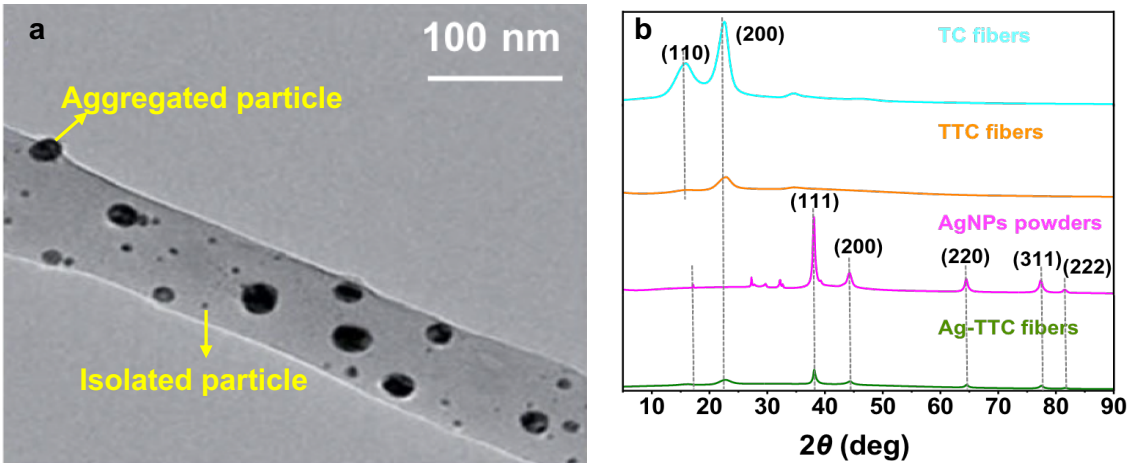

Figure 2-2. (a) TEM image of an Ag-TTC nanofiber. (The yellow arrows indicate the presence of aggregated particle and isolated particle). (b) XRD patterns of TC fibers, TTC nanofibers, AgNPs, and Ag-TTC nanofibers.

Ag-TTC was synthesized by using GTE as a green reductant and TTC as a stabilizer at room temperature. As observed from the TEM image in **Figure 2-2a**, AgNPs (black features) grew on the surface of the TTC (gray) nanofiber. The size of homogeneously dispersed AgNPs was 10–20 nm. AgNPs were partially aggregated (bigger ones) and isolated particles (smaller ones) were also detected in some regions. Both of them are indicated by yellow arrows. The crystalline structures of TC, TTC, AgNPs, and Ag-TTC were analyzed by XRD (**Figure 2-2b**). From the XRD analysis, TC had a typical semi-crystalline cellulose structure, as indicated from the characteristic diffraction peaks observed at 2θ =16.21° and 22.76°, which correspond to the (110) and (200) planes, respectively. The XRD pattern of TTC featured similar peaks at similar positions. However, compared with TC, TTC had a lower degree of crystallinity because of the

complete separation of the crystalline cellulose microfibrils into individual nanofibers. The XRD pattern of AgNPs featured characteristic peaks at 2θ of 38.08, 44.36, 64.51, 77.41, and 81.65°, which correspond to Ag (AgNPs) face-centered cubic planes (111), (200), (220), (311), and (222), respectively (JCPDS File No. 89-3722). Ag-TTC featured characteristic peaks of both TTC and AgNPs, indicating the coating of AgNPs on the surface of the TTC nanofibers.

2.3.3 Water solubility and XPS spectra of TTC and TTC@AgNPs composite films

Table 2-1. Water solubility and changes in the shape of the TTC and Ag-TTC-PVA films

Samples[a]	Water Solubility[b] (%)	Shape
TTC	35.9 ± 1.1	change
Ag-TTC-0.5-0.5	30.7 ± 0.9	change
Ag-TTC-0.5-2	28.1 ± 0.5	change
Ag-TTC-0.5-5	24.5 ± 1.2	change
Ag-TTC-1-0.5	20.5 ± 0.8	change
Ag-TTC-1-2	18.1 ± 0.5	no change
Ag-TTC-1-5	17.9 ± 0.2	change
Ag-TTC-2-0.5	20.1 ± 1.7	change
Ag-TTC-2-2	17.7 ± 0.9	change
Ag-TTC-2-5	16.5 ± 0.6	change

[a]Films are denoted as follows: Ag-TTC-*x*-*y*, where *x* refers to the concentration of TTC and *y* refers to the concentration of immobilized AgNPs.

[b]Data are shown as the mean ± standard deviation (SD) (n = 3).

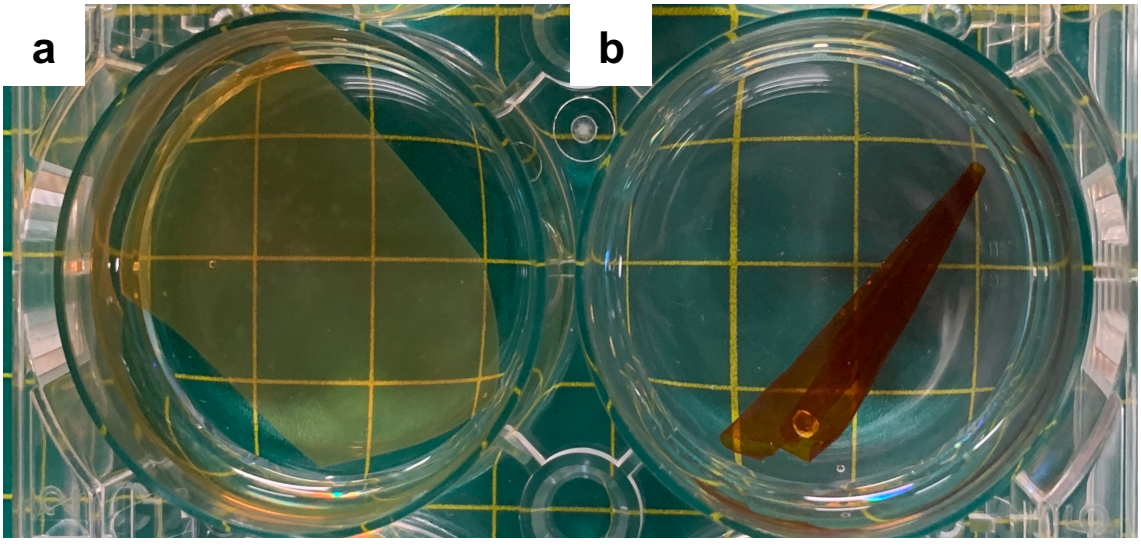

Figure 2-3. Shape a) no change and b) change of the Ag-TTC-PVA films immersed in water.

The water solubility of the TTC-PVA and Ag-TTC-PVA films is summarized in **Table 2-1**. When immersed in the TTC-PVA film in the water for several hours, it will have higher water solubility and the shape of the film is easily change following immersion. The Ag-TTC-PVA film containing 0.5, 2, and 5% (w/w_{TTC}) Ag-TTC displayed a substantially reduced water solubility capability when compared with the TTC film. As reported, cellulose has a high amount of hydroxyl groups as well as substantial intra- and intermolecular hydrogen bonding interactions.[33] These chemical groups are likely involved in the stabilization of the AgNPs by anchoring silver to the cellulose fibers and through interactions between the AgNPs and cellulose hydrogen bonds. Therefore, the decrease in the water solubility of the Ag-TTC-PVA composite films indicates a strong interaction between the TTC nanofibers and AgNPs. The Ag-TTC composite film prepared with the weight ratio of TTC: Ag-TTC: PVA as 1 wt.%: 2% (w/w_{TTC}): 10 wt.% were considered as an optimal film because of the low water solubility and negligible changes in film shape following immersion of the film in water for several hours (**Figure 2-3**).

The chemical surface composition of the films was probed by XPS. Comparison of the XPS survey spectra of the TTC-PVA and Ag-TTC-PVA composite films (**Figure 2-4a**) revealed the presence of high contents of C and O in the Ag-TTC-PVA film owing to the immobilization of AgNPs on the surface of TTC-PVA. The strong metallic Ag 3d signal peaks at binding energies of 367.8 eV (Ag $3d_{5/2}$) and 373.8 eV (Ag $3d_{3/2}$), shown in **Figure 2-4b**, further support the successful generation of AgNPs on the Ag-TTC-PVA film. The functional groups in TTC are likely involved in the stabilization of the AgNPs through interactions between TTC and the AgNPs. Comparison of the C 1s XPS spectra in **Figures 2-4c** and **2-4d** revealed the presence of more carboxylate groups on the Ag-TTC-PVA composite film than on the TTC-PVA film. These groups serve as effective host functional groups to guest metallic ions through strong ionic interactions. The AgNPs subsequently aggregate for immobilization onto TTC.

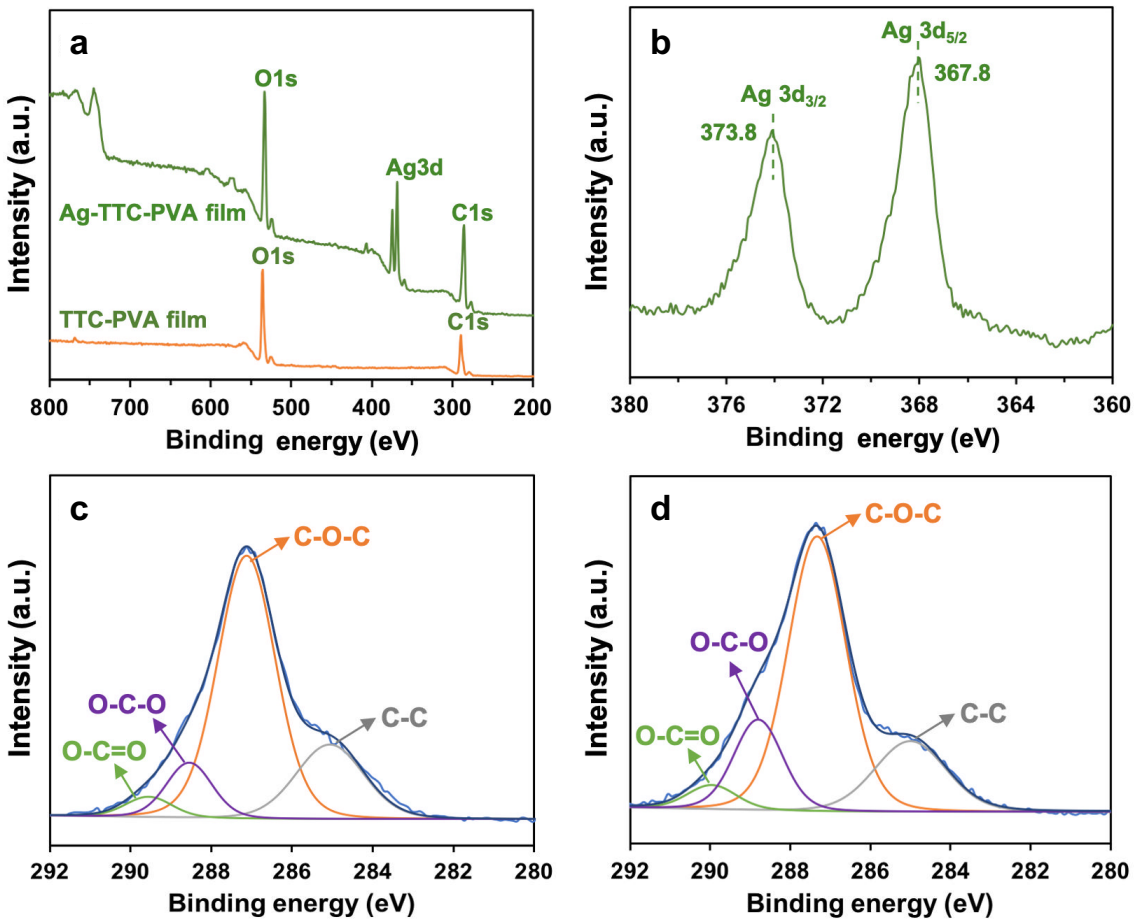

Figure 2-4. (a) XPS survey spectra of the TTC-PVA and Ag-TTC-PVA films. (b) High-resolution Ag XPS spectrum (380–360 eV) of the Ag-TTC-PVA film. High-resolution C 1s XPS deconvolution spectra of the (c) TTC-PVA and (d) Ag-TTC-PVA films.

2.3.4 Physical appearance, and color of TTC and TTC@AgNPs composite films

As presented in **Figure 2-5**, the TTC-PVA film was transparent and colorless, whereas the Ag-TTC-PVA composite film was red-brown with the addition of AgNPs. The physical appearance of the films was further characterized by their color parameters (**Table 2-2**). The incorporation of AgNPs led to a smaller L value, indicating that the Ag-TTC-PVA composite film was darker than the TTC-PVA film given that $L = 0$ is black and $L = 100$ is white. The values of a and b were significantly larger for the Ag-TTC-PVA composite film than for the TTC-PVA film, which indicates more intense hues of red and yellow in the Ag-TTC-PVA composite film. Moreover, the Ag-TTC-PVA composite film displayed a higher ΔE value than the TTC-PVA film, further confirming the coloration of the Ag-TTC-PVA composite film. In

summary, the color parameters in **Table 2-2** indicate that the Ag-TTC-PVA composite film was darker and more red and yellow than the TTC-PVA film.

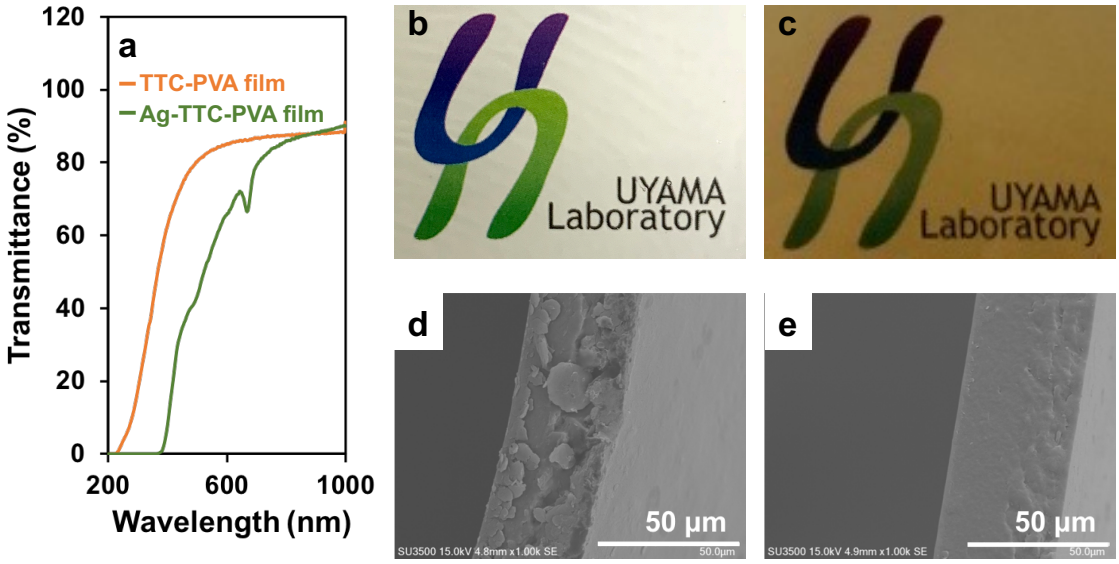

Figure 2-5. (a) The transmittance of the TTC-PVA and Ag-TTC-PVA composite films. Photographs of the (b) TTC-PVA and (c) Ag-TTC-PVA composite films. SEM images of cross-sections of the (d) TTC-PVA and (e) Ag-TTC-PVA composite films.

The UV–vis light barrier property of a film is an important parameter to examine for application in light-sensitive food packaging. **Figure 2-5a** shows the UV–vis transmittance of the TTC-PVA and Ag-TTC-PVA composite films. The results show that the TTC-PVA film featured a lower UV–vis light barrier than the Ag-TTC-PVA composite film in the range of 400–200 nm, owing to the absence of UV–vis absorption groups in the TTC structure. In addition, the shielding effect of AgNPs against UV–vis light contributed to the higher UV–vis light barrier of the Ag-TTC-PVA composite film when compared with that of the TTC-PVA film. The transmittance at 600 nm was approximately 85% for the TTC-PVA film and 68% for the Ag-TTC-PVA composite film. The reduced optical transmittance of the Ag-TTC-PVA composite film was attributed to the stabilizing effect of the AgNPs through interactions between cellulose hydrogen bonds and the AgNPs, which hindered light transmission across the film. **Figures 2-5b** and **2-5c** respectively show photographs of the surface of the TTC-PVA and Ag-TTC-PVA composite films. In general, the films were smooth and uniform, indicating that TTC and Ag-TTC were homogenously mixed with PVA. GTE (2% w/w_{TTC}), TTC (1 wt.%),

and PVA (10 wt.%) were also mixed to prepare the GTE-TTC-PVA composite film,. Further analysis showed that the Ag-TTC-PVA composite film was smoother and more homogenous than the TTC-PVA film (**Figure 2-5d and 2-5e**). This observation indicates the uniform dispersion of the immobilized AgNPs within the TTC matrix of the composite films, resulting in a smooth film surface.

Table 2-2. Color parameters of the TTC-PVA and Ag-TTC-PVA composite films[a]

Samples	L	a	b	ΔE	WI
TTC-PVA	85.9 ± 1.1	-2.1 ± 0.5	0.5 ± 0.3	8.7 ± 0.9	85.7 ± 0.3
Ag-TTC-PVA	37.7 ± 0.9	24.5 ± 0.2	36.9 ± 0.6	72.3 ± 0.4	23.6 ± 0.7

[a]Data are shown as the mean ± standard deviation (n = 3).

2.3.5 Mechanical properties of the dry/wet TTC-PVA and Ag-TTC-PVA films.

The feasible usage of films in food packaging is typically determined by their mechanical property such as TS and EAB. **Figure 2-6** shows the strain–stress curves of dry/wet TTC-PVA and Ag-TTC-PVA composite films. As observed, the addition of Ag-TTC significantly improved the mechanical property of the resulting film. As summarized in **Table 2-3**, the dry Ag-TTC-PVA composite film displayed both high strength and toughness, which were superior to the mechanical properties displayed by the other films examined. The maximum failure strength of the dry Ag-TTC-PVA composite film (∼75 MPa) was ~1.1-fold higher than that of the dry TTC-PVA film. The EAB of the dry Ag-TTC-PVA composite film was higher than that of the dry TTC-PVA film, indicating the increased flexibility of the Ag-TTC-PVA composite film. These results indicate that the addition of Ag-TTC can improve the mechanical properties of the Ag-TTC-PVA composite film. The improvement in the mechanical property is attributed to the stronger cross-linking effect of the TTC-PVA chains upon the introduction of Ag-TTC, which can fill the interspace of the TTC-PVA films, thereby making the inner structure of the film more compact and subsequently increasing its mechanical properties, as consistent with the SEM results (**Figure 2-5d and 2-5e**). As the hydroxyl groups in TTC can easily form hydrogen bonds with water molecules in a humid environment, the TS of the wet films was also assessed. The maximum failure strength of the wet Ag-TTC-PVA composite film (∼55 MPa) was also ~1.1-fold higher than that of the wet TTC-PVA film (**Table 2-3**). Likewise, the EAB of the wet Ag-TTC-PVA composite film was higher

than that of the wet TTC-PVA film, indicating that the Ag-TTC-PVA composite film was more flexible than the TTC-PVA film. The TS of both the TTC-PVA and Ag-TTC-PVA wet composite films remained high values, which is indicative of interactions between cellulose hydrogen bonds and the AgNPs under the wet conditions, and these function as plasticizers within the framework. Poly(ethylene terephthalate) (PET) [34] and polypropylene (PP) [35] as packaging materials with the tensile strength of ~50 MPa and ~80 MPa, respectively. Zhang, et al. prepared the CS-TiO_2-BPPE composite as food packaging with the tensile strength of ~23.9 MPa.[36] Hesham, et al. use organoclay with poly(butylene adipate-*co*-terephthalate) (PBAT) to prepare the composite films with the tensile strength of ~17.6 MPa and 18.2 MPa.[37] In our research, the tensile strength of both dry/wet Ag-TTC-PVA films is more than 50 MPa (**Table 2-3**). Thus, Ag-TTC-PVA wet composite films have sufficient strengths for food packages.

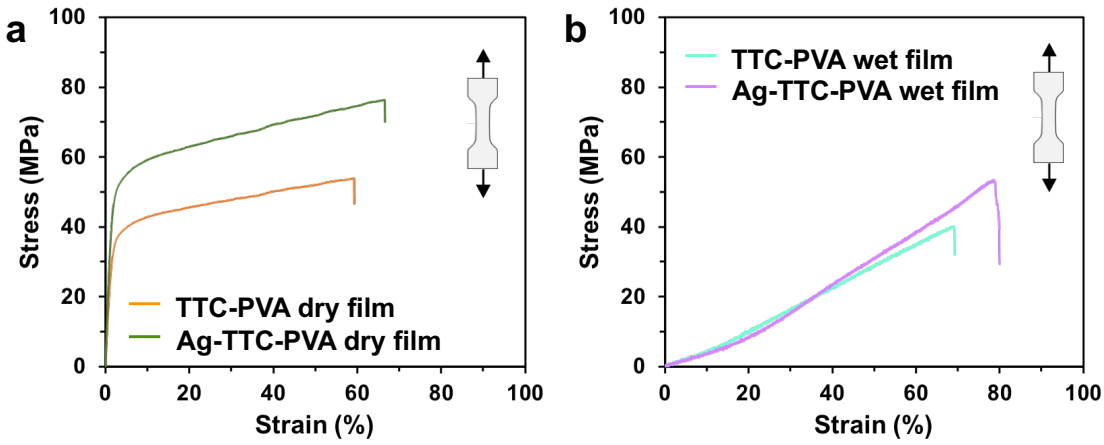

Figure 2-6. Tensile stress-strain curves of dry/wet TTC-PVA and Ag-TTC-PVA films.

Table 2-3. Tensile strength and elongation at break of dry and wet TTC-PVA and Ag-TTC-PVA composite films[a]

Samples	Tensile Strength (MPa)	Elongation at Break (%)
Dry TTC-PVA	66.2 ± 1.2	68.2 ± 2.5
Dry Ag-TTC-PVA	75.2 ± 1.1	78.9 ± 2.2
Wet TTC-PVA	48.6 ± 1.4	59.2 ± 1.9
Wet Ag-TTC-PVA	55.6 ± 0.9	69.2 ± 2.7

[a]Data are shown as the mean ± standard deviation (n = 3).

Figure 2-7 shows SEM images of the cross-section images of the TTC-PVA and Ag-TTC-PVA dry and wet composite films after the tensile test. The properties of a material are closely related to the dispersion of the filler in the composite: as the filler dispersion becomes more homogeneous, the

material properties improve. As observed from the SEM images, the dispersion of the TTC-based filler was largely homogeneous. The dimples observed on the fractured surface correspond to the extent of plastic deformation that the wet Ag-TTC-PVA composite film underwent before fracture. The small number of large-sized and deep dimples observed shows that this fracture mode is a ductile fracture and indicates that the wet Ag-TTC-PVA composite film displays higher toughness than the wet TTC-PVA film.

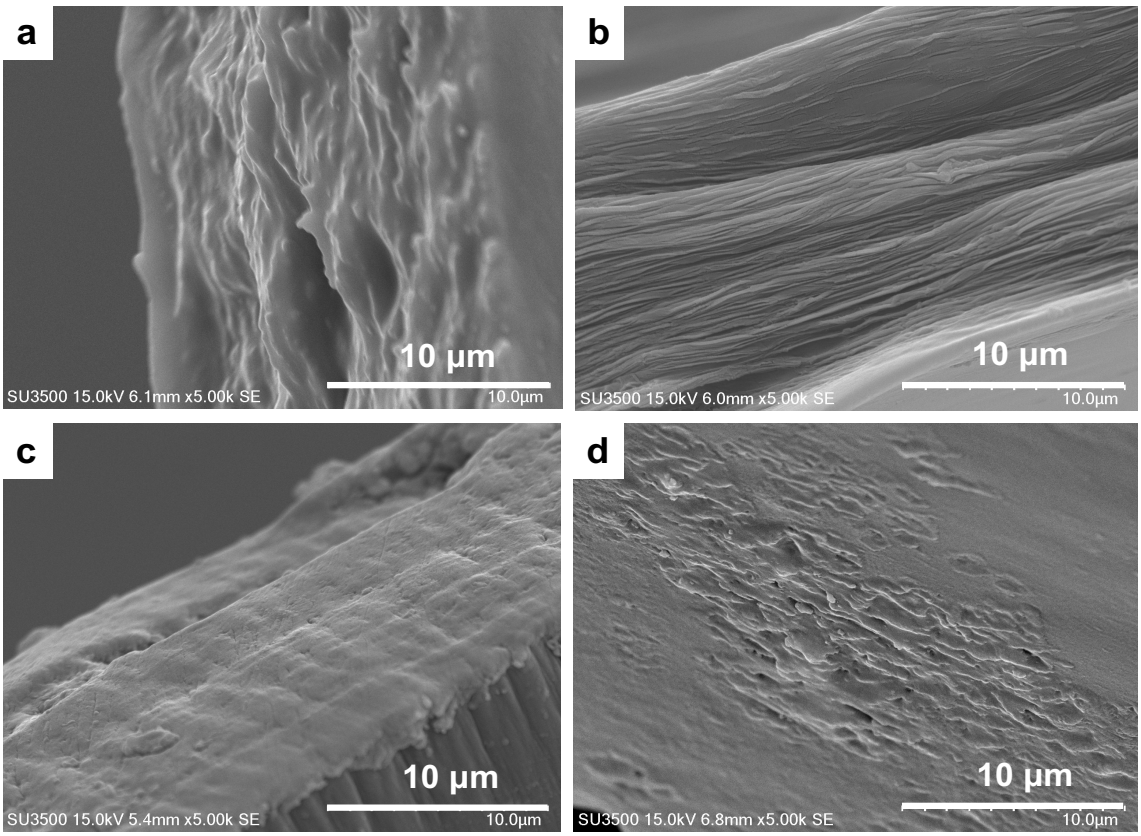

Figure 2-7. SEM images of cross-sections of (a) dry and (b) wet TTC-PVA films, and (c) dry and (d) wet Ag-TTC-PVA composite films after tensile test.

2.3.6 Thermal properties of TTC-PVA and Ag-TTC-PVA films

As shown in **Figure 2-8a**, the PVA film displayed two stages of decomposition.[38-40] The decompositions at ~200–360 °C and 360–500 °C were attributed to the decomposition of the side hydroxyl group and the main chain of PVA, respectively. The degradation of the TTC nanofibers shifted to a lower temperature of 230 °C relative to that of the TC fibers that occurred at 360 °C. This shift is attributed to the surface modification of TC upon oxidation, which occurs at the C6–OH to form sodium carboxylate groups (–COO–Na^+) on the surface of the TC fibers.

Compared with the thermal stabilities of the PVA film and the TC and TTC fibers, the thermal stabilities of the TTC-PVA and Ag-TTC-PVA composite films improved through hydrogen bonds between the matrices and fillers. As observed in **Figure 2-8b**, the derivative TGA (DTG) curve of the TTC-PVA and Ag-TTC-PVA composite films featured two peaks at ~290 °C and ~360 °C, which coincide with the peaks observed in the PVA film and TC fibers, respectively. These findings confirm the presence of strong interfacial interactions between PVA and TTC in the TTC-PVA and Ag-TTC-PVA composite films. During film synthesis, the TC microfibrils exhibit high hydroxyl group packing density, which is maintained upon rapid temperature changes. It will form fiber–fiber and fiber-matrix hydrogen bonding interactions.[41]

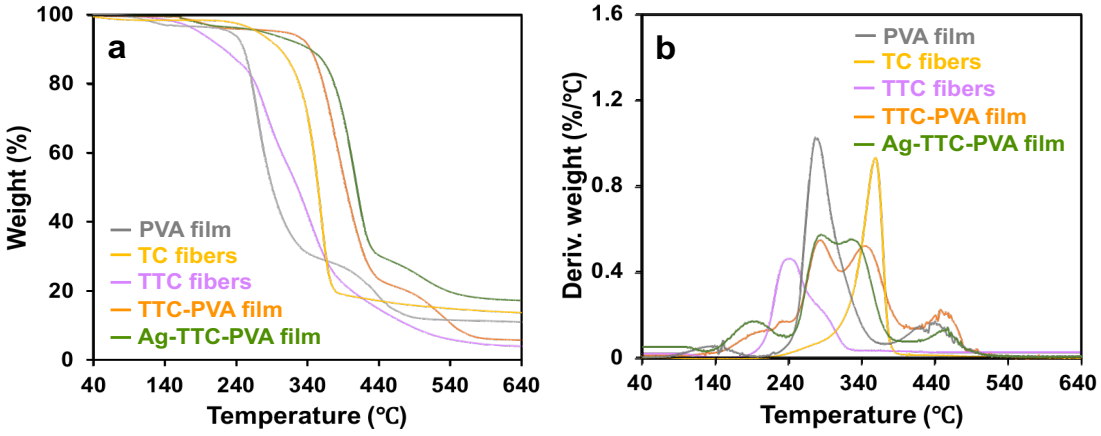

Figure 2-8. (a) TGA and (b) DTG curves of the TC fibers, TTC nanofibers, PVA film, TTC-PVA film, and Ag-TTC-PVA composite film.

TGA curves of the TTC-PVA and Ag-TTC-PVA composite films displayed three degradation steps. The first step (170–260 °C) was attributed to the decomposition of the tea polyphenols and the main intermolecular hydrogen bonds of PVA in both the TTC-PVA and Ag-TTC-PVA composite films. The second step was observed at 260–420 °C, with a maximum at approximately 360 °C, for the TTC-PVA film, whereas for Ag-TTC-PVA composite film, the second step occurred at 260–440 °C, with a maximum at approximately 420 °C. For both films, the decomposition was attributed to the rupture of the TC microfibrils and the intramolecular chain degradation of PVA. The final decomposition step occurred at 420–560 °C for the TTC-PVA film and 440–560 °C for the Ag-TTC-PVA composite film. This decomposition step was attributed to the cleavage of the C–C backbone of PVA and the production of carbon molecules

and hydrocarbons. Notably, the Ag-TTC-PVA composite film displayed a lower weight loss than the TTC-PVA film, suggesting increased thermal stability upon the incorporation of the AgNPs. The thermal stability of the TTC-PVA and Ag-TTC-PVA composite films is also related to the dispersion homogeneity of TTC in the composite.

2.3.7 AgNPs release and antioxidant properties of TTC-PVA and Ag-TTC-PVA films

Although AgNPs display good antimicrobial activity, their potential release can be toxic and present health concerns. The Ag-TTC-PVA composite film was fully soluble in H_2SO_4 (0.5 mol L^{-1}) and then test the total amount of AgNPs, which is 34 ppm. **Figure 2-9a** shows the cumulative release rates of AgNPs from the immobilized film as well as in free (non-immobilized) form in phosphate buffer (pH 7). The results show that the release rates of AgNPs from the immobilized AgNPs composite film were considerably and sustainably (up to 120 h examined) slower than those of the non-immobilized AgNPs. The findings indicate that TTC-PVA exerts an effective immobilizing effect on AgNPs, resulting in reduced AgNPs leakage.

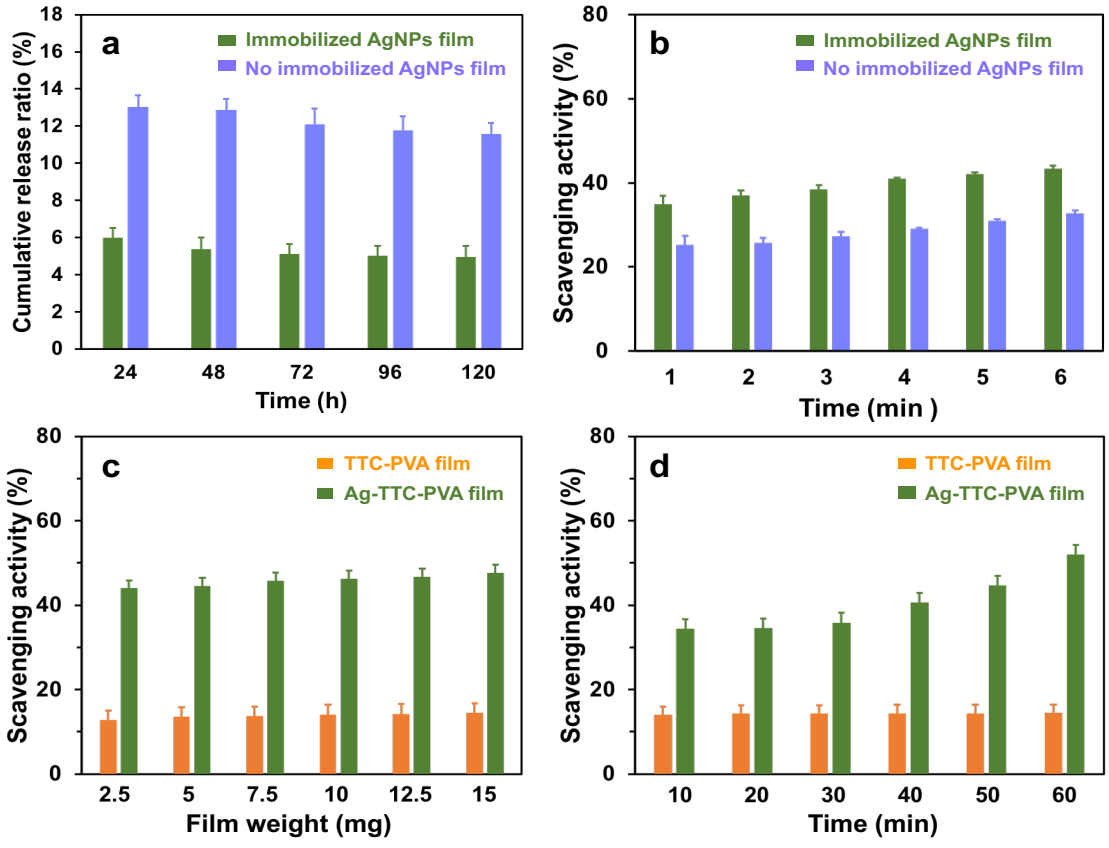

Figure 2-9. (a) Cumulative release rates of AgNPs in phosphate buffer (pH 7) and (b) antioxidant

performance of non-immobilized AgNPs and immobilized AgNPs film. (c) Dose-dependent and (d) time-dependent scavenging activities of the TTC-PVA and Ag-TTC-PVA composite films. Data are shown as the mean ± standard deviation (n = 3).

As shown in **Figure 2-9b**, the non-immobilized AgNPs film displayed a lower scavenging activity than the immobilized AgNPs film because AgNPs were readily released from non-immobilized AgNPs film, thus displaying reduced antioxidant property. The dose-dependent and time-dependent antioxidant properties of the TTC-PVA and Ag-TTC-PVA composite films were also studied, and the results are shown in **Figures 2-9c and 9d**. The DPPH radical scavenging activity of the Ag-TTC-PVA composite film was consistently higher than that of the TTC-PVA film irrespective of the dose or reaction time examined. For instance, at a film weight of 15 mg mL^{-1}, the DPPH radical scavenging activity of the Ag-TTC-PVA composite film was 48%, whereas that of the TTC-PVA film was 15%. These results demonstrate that the Ag-TTC-PVA composite film has a strong antioxidant activity and can prevent oxidative rancidity in food.

2.3.8 Photocatalytic activities of TTC-PVA and Ag-TTC-PVA films

The photocatalytic activities of composite films are assessed by the degradation of MO under UV irradiation. **Figure 2-10a** shows the color differences between the MO solutions with and without immersing the TTC-PVA or Ag-TTC-PVA composite films. TTC-PVA film without AgNPs has a non-specific adhesion process during the 30 min in dark. The color of MO with immersing TTC-PVA film has a little lighter than MO solution, which because the MO was partially absorbed by TTC-PVA film after 30 min in dark. The color of MO solution with immersing Ag-TTC-PVA composite film was lighter than that with immersing TTC-PVA film. As shown in **Figure 2-10b**, no significant degradation of MO is observed without films, indicating that the self-degradation of MO could be neglected under UV irradiation. It is obvious that the concentration of MO of TTC-PVA film immersed MO solution slightly decreased 7% and reached adsorption-desorption equilibrium after 30min in dark; however, the concentration of MO did not change after irradiated by UV for 60 min. When the Ag-TTC-PVA composite film was immersed in the MO solution in dark for 30 min, approximately 11% of

MO was adsorbed by the Ag-TTC-PVA composite film. 56% of MO was photodegraded after the subsequent 60 min immersion under UV irradiation, which implies the good photocatalytic activity of the Ag-TTC-PVA composite film. This is because the UV irradiation struck the valence electrons of Ag in Ag-TTC-PVA composite film, which gained energy and was emitted from the valence shell. After emission, these highly energetic electrons were used in the generation of hydroxyl radicals which were responsible for the degradation of dyes.[42-45] These results demonstrate that MO can be degraded by the Ag-TTC-PVA composite film.

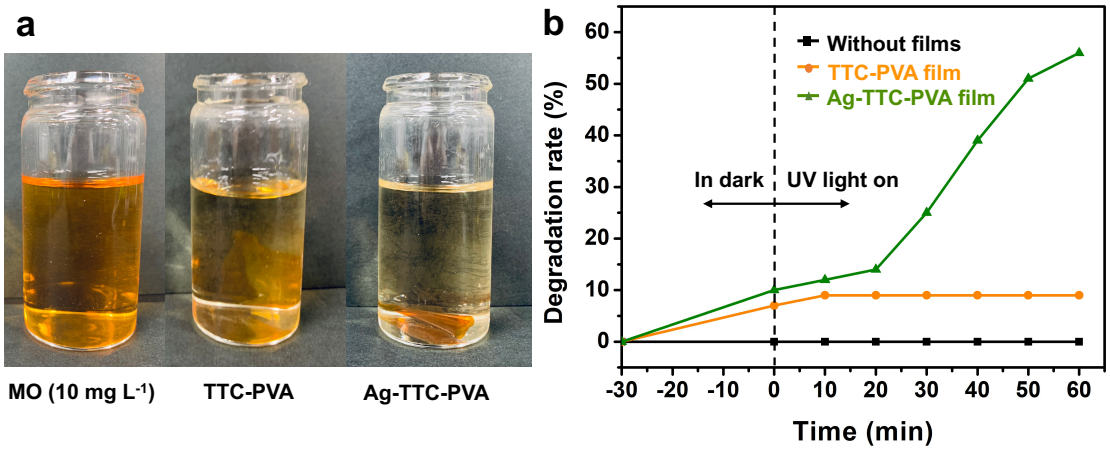

Figure 2-10. (a) Images of the MO solution with or without immersing TTC-PVA or Ag-TTC-PVA composite films under UV irradiation. (b) Degradation rates of MO in the solution in dark/under UV irradiation with or without immersing TTC-PVA or Ag-TTC-PVA composite film.

2.4 Conclusions

In summary, flexible and transparent Ag-TTC-PVA composite film with multifunctional performance is successfully prepared by the chemical immobilization of pre-prepared AgNPs. TTC was successfully applied as a template to synthesize and immobilize AgNPs owing to the presence of carboxylic groups that immobilized metal ions on the cellulose backbone, which contributes to separating and recovering catalysts from the reaction system without centrifugation and filtration. The Ag-TTC-PVA composite film featured improved mechanical and thermal properties when compared with the TTC-PVA films. In addition, the presence of TTC inhibited the fast release of AgNPs from the TTC-derived films, thereby reducing the cytotoxic effects of the AgNPs. Particularly, the Ag-TTC-PVA composite film possessed high antioxidant activity and photocatalytic performance, which is beneficial for decreasing the agglomeration of nanoparticles and simultaneously improving the photocatalytic efficiency. Most importantly, TTC and PVA, the main raw materials of the prepared films, all possess superior biodegradability and biocompatibility, which contributes to broadening their application fields and simultaneously decreasing the secondary contamination caused by the used composite films. We believe that the obtained composite films may have great potential application value in different fields, including photocatalysis and medicine.

2.5 References

1. D. Dehna, Z. Djomeh, H. Mirzaei, *Carbohydr Polym.*, 2014, **105**, 222–228.
2. M. Makaremi, G. Cavallaro, S. Lee, *ACS Appl Mater Interfaces.*, 2017, **9**, 17476–17488.
3. K. Goh, J. Heising, Y. Yuan, *ACS Appl Mater Interfaces.*, 2016, **8**, 9994–10004.
4. M. Felix, V. Puyana, A. Romero, J Polym Environ., 2017, **25**, 91–100.
5. F. Hemmati, S. Jafari, M. Motlagh, *Int J Biol Macromol.*, 2018, **120**, 1216–1224.
6. C. Solak, A. Kaleli, O. Baytut, *Turkish J Fish Aquat Sci.*, 2016, **16**, 953–959.
7. M. Imran, S. Fahmy, S. Desobry, *Carbohydr Polym.*, 2010, **81**, 219–225.
8. O. Choi, K. Deng, N. Kim, *Water Res.*, 2008, **42**, 3066–3074.
9. Y. Loo, Y. Rukayadi, M. Khaizura, *Front Microbiol.*, 2018, **9**, 1–7.
10. M. Benelmekki, J. Vernieres, J. Kim, *Mater Chem Phys.*, 2015, **151**, 275–281.
11. F. Mafuné, J. Kohno, Y. Takeda, *J Phys Chem B.*, 2001, **105**, 5114–5120.
12. Y. Hiragino, T. Tanaka, H. Takeuchi, *Solid State Electron.*, 2016, **118**, 41–45.
13. S. Pirtarighat, M. Ghannadnia, S. Baghshahi, *J Nanostructure Chem.*, 2019, **9**, 1–9.
14. Z. Xiong, Y. Zhu, F. Chen, *Chem. Eur. J.*, 2016, **22**, 11224–11231.
15. V. Kumar, T. Uchida, T. Mizuki, *Adv Nat Sci Nanosci Nanotechnol.*, 2016, **7**, 66–78.
16. V. Vidhu, D. Philip, *Micron.*, 2014, **56**, 54–62.
17. S. Kang, C. Liao, S. Po, *Chemosphere*, 2000, **41**, 1287–1294.
18. T. Saito, S. Kimura, Y. Nishiyama, *Biomacromolecules*, 2007, **8**, 2485–2491.
19. X. Hu, K. Hu, L. Zeng, *Carbohydr Polym.*, 2010, **82**, 62–68.
20. C. Waters, R. Mallinson, L. Lobban, *J Anal Appl Pyrolysis.*, 2017, **126**, 380–389.
21. N. Rahman, B. Chieng, N. Ibrahim, *Polymers*, 2017, **9**, 1–11.
22. T. Zhao, Z. Chen, X. Lin, *Carbohydr Polym.*, 2018, **184**, 164–170.
23. W. Rolim, M. Pelegrino, B. Lima, *Appl Surf Sci.*, 2019, **463**, 66–74.
24. C. Jiao, Z. Zhang, J. Tao, *RSC Adv.*, 2017, **7**, 27787–27795.
25. L. Dai, Z. Long, Y. Zhao, *Cellulose*, 2016, **23**, 2989–2999.
26. Y. Habibi, H. Chanzy, M. Vignon, *Cellulose*, 2006, **13**, 679–687.

27. D. Perez, S. Montanari, M. Vignon, *Biomacromolecules*, 2003, **4**, 1417–1425.
28. H. Wen, Y. Hsu, T. Asoh, *Polym. Degrad. Stab.*, 2020, **178**, 109215.
29. Z. Adilah, B. Jamilah, Z. Hanani, *Food Hydrocoll.*, 2018, **74**, 207–218.
30. M. Kurek, I. Garofulić, M. Bakić, *Food Hydrocoll.*, 2018, **84**, 238–246.
31. K. Halász, L. Csóka, *Food Packag Shelf Life*, 2018, **16**, 185–193.
32. C. Wu, S. Fuh, S. Lin, *Biomacromolecules*, 2018, **19**, 544–554.
33. L. Valle, A. Díaz, J. Puiggalí, *Gels*, 2017, **3**, 27.
34. N. Dardmeh, A. Khosrowshahi, H. Almasi, *J Food Process Eng.*, 2017, **40**, e12324.
35. M. Lauer, R. Smith, *Compr Rev Food Sci Food Saf.*, 2020, **19**, 3031–3083.
36. X. Zhang, Y. Liu, H. Yong, *Food Hydrocoll.*, 2019, **94**, 80–92.
37. H. Moustafa, A. Youssef, N. Darwish, *Compos Part B Eng.*, 2019, **172**, 16–25.
38. J. Chen, D. Wei, W. Gong, *ACS Appl Mater Interfaces*., 2018, **10**, 37535–37543.
39. T. Kuo, C. Jhang, C. Lin, *Open Phys.*, 2017, **15**, 1004–1014.
40. J. Gilman, D. VanderHart, T. Kashiwagi, *ACS Symp Ser.*, 1995, **75**, 161–185.
41. B. Poyraz, A. Tozluoğlu, Z. Candan, *Fibers Polym.*, 2018, **19**, 195–204.
42. E. Elemike, D. Onwudiwe, A. Ekennia, *Mater Sci Eng C.*, 2017, **75**, 980–989.
43. V. Saraswathi, D. Saravanan, *J Photochem Photobiol B Biol.*, 2017, **171**, 20–26.
44. V. Saraswathi, J. Tatsugi, P. Shin, *J Photochem Photobiol B Biol.*, 2016, **167**, 89–98.
45. K. Tahir, S. Nazir, B. Li, *Sep Purif Technol.*, 2015, **150**, 316–324.

Chapter 3.

Antifouling multifunctional material was developed by using gallic acid-terminated poly(2-ethyl-2-oxazoline) as the sustainable scaffold graft on the poly(methyl methacrylate) surface

3.1 Introduction

At present, renewable and biodegradable biocomposite materials have been attracting much attention as promising green materials in different domains of application such as biomedical, [1] and bio-membranes. [2] The raw material from plants offers another common source to produce multifunctional bio-based materials. [3,4] Plant-derived materials constitute the bulk of the green linker molecules, which are the class of crosslinker, are biocompatible, and do not possess any environmental hazards. Bio-based linker molecules provide a greener and environmentally sustainable alternatives for producing suitable multifunctional bio-composites. Xu et al. are developing novel materials to reduce the biofouling of surfaces, with an emphasis on the design of protein-resistant coatings. [5-7] A common theme is the use of mussel-inspired strategies for linking antifouling polymers onto surfaces. These coatings can be made by adsorbing catechol modified polymers onto a surface, or by adsorbing an initiator and growing bound polymer by surface-initiated polymerization. Further, these natural moieties overcome issues of the biocompatibility and toxicity of synthetic linker molecules. Bio-based linker molecules possess inherent medicinal properties and thereby furnish an additional benefit over synthetic crosslinkers. [8-10]

Surface biofouling, which is defined as the undesired adhesion and accumulation of biomolecules and organisms with sizes ranging from nanometer to centimeters, has been a persistent problem for centuries. [11] Poly(methyl methacrylate) (PMMA) is a non-toxic polymer as it possesses a very good toxicological safety record in biomedical applications. [12,13] However, PMMA has a strong tendency to induce protein adsorption on its surface owing to its poor antifouling properties. [14-16] With the development of medical composite materials, higher

requirements have been proposed for long-term use and for reducing protein adsorption and local inflammation. [17-19] Therefore, the design of antifouling PMMA surfaces is imperative. [20,21]

Poly(2-ethyl-2-oxazoline) (PEtOx) and its derivatives have attracted wide attention because of their excellent antifouling capacities. [22-25] The amide groups of the PEtOx and its derivatives can form hydrogen bonds with water, generating a physical barrier to hinder the fouling process. Tannic acid (TA), a natural-occurring polyphenol extracted from green tea, has been investigated as an ideal and sustainable linker molecule for fabricating multifunctional coatings on substrate surfaces. [26-28] Sundaramurthy et al. [29] reported a universal approach was performed to construct anti-fouling materials surface inspired from tannic acid and Poly(2-oxazoline)s. For coating applications, it is necessary to immobilize PEtOx on the surface. However, weak binding onto a surface would reduce the long-term stability of the coating. The chemical long-term stability of antifouling coatings is mandatory and can be greatly improved by terminating end groups on surface-coated polymers with functional group-terminated polymers. [30]

Gallic acid (GA), which is a subset of polyphenols, are colorless naturally occurring crystalline compounds found in all plants. GA has also proven to be an effective anti-inflammatory agent and may reduce the symptoms of arthritis, lupus, and other inflammatory conditions such as allergies. [31] Because of its molecular structure, anti-inflammatory property, and low cost, GA attracted our interest as a linker molecule to obtain multifunctional coatings between PEtOx and PMMA substrate. Firstly, GA can functionalize PEtOx by terminating the end groups via an esterification method using ytterbium trifluoromethanesulfonate ($Yb(OTf)_3$) as the catalyst, resulting in strong binding to the surface of the biomaterial. Secondly, PEtOx-GA was reacted poly(ethyleneimine)-modified PMMA substrate (PEI-S) to form the functional film (PEtOx-GA-PEI-S) via Schiff-base and Michael addition reactions. Among them, PEI-S was obtained by adding the amino groups from PEI, onto the surface of PMMA through a nucleophilic addition-elimination reaction. [32-35]

In this study, a PEtOx-GA-PEI-S functional film with good protein adsorption prevention properties was developed and the functional film was formed by using GA as an ideal and

sustainable linker molecule for fabricating multifunctional coatings onto the surface. A new bio-based polymer (PEtOx-GA) with good antifouling and anti-inflammatory properties was first synthesized via a simple and convenient method. The morphology, surface chemical structure, and composition of the PMMA substrate, PEI-S, and PEtOx-GA-PEI-S functional films were characterized by scanning electron microscopy (SEM), atomic force microscopy (AFM), Fourier transform infrared spectroscopy (FTIR), and X-ray photoelectron spectroscopy (XPS), respectively. The effects of the PMMA substrate, PEI-S, and PEtOx-GA-PEI-S functional films on the adsorption of proteins were also investigated. Therefore, this galloyl group terminated polymer plays a fresh and universal route to construct antifouling surface applying for multifunctional composite materials.

3.2 Experimental Section

3.2.1 Materials

$Yb(OTf)_3$, PEtOx (M_w = 5,000 g mol^{-1}), PMMA (M_w = 120,000 g mol^{-1}), nitromethane (CH_3NO_2), GA, bovine serum albumin (BSA, 66.5 kDa), lysozyme (recombinant, expressed in rice, 16.5 kDa), myoglobin (from equine skeletal muscle, 17 kDa), and plasma (from bovine, 10 mL) were purchased from Sigma-Aldrich (Tokyo, Japan). Plasma was diluted with phosphate buffer (pH 7.4) for experiments. PEI (M_w = 1,800 g mol^{-1}) and $MgSO_4$ were purchased from Fujifilm Wako Pure Chemical Corporation (Tokyo, Japan). 4-Acetoxybenzoic acid was purchased from Tokyo Chemical Industry Co., Ltd. (Tokyo, Japan). Phosphate buffer (0.1 mol L^{-1}, pH 7.4) was purchased from Nacalai Tesque, Inc. (Kyoto, Japan). Deionized water (DI water) was used for solution preparation and dilution. All reagents were of analytical grade and used as received without further purification.

3.2.2 Synthesis of PEtOx-GA powder

GA (0.4 mmol) and PEtOx (0.4 mmol) were mixed in a solvent (CH_3NO_2, 10 mL) and the Lewis catalyst $Yb(OTf)_3$, 1 mol%, was added. After 5 min in an ultrasonic bath, the mixture was stirred in an oil bath at 120 °C under a nitrogen atmosphere for 35 min. After cooling, the mixture was washed three times with water and sodium bicarbonate ($NaHCO_3$) (30 mL) and dried over $MgSO_4$. The mixture was then dialyzed for 5 days, and a freeze drier was used to obtain PEtOx-GA powder. The yield of PEtOx-GA in the reaction was determined using a 1220 Infinity LC system (reversed-phase column C18), 65% MeOH in H_2O for 20 min at 1.0 mL min^{-1} and UV detection at 210 nm, TOSOH, Tokyo, Japan) with 4-Acetoxybenzoic acid as the internal standard substance, which was added to the reaction mixture in an amount equivalent to the gallic acid. The aqueous layer was concentrated in vacuo to give a crystalline residue, which was finally heated at 180 °C for 48 h in vacuo to afford recovered $Yb(OTf)_3$. The structure of PEtOx-GA was confirmed by ^1H NMR spectroscopy. Yield=1.47 g, 74%; Mn = 5,168 g/mol. ^1H NMR (400 Hz, CD_3OD, ppm) δ: 6.98 (s, 2H, **proton from galloyl group**), 3.63–3.31 (m, 4H, −NCO**CH_2CH_2**−), 3.03–2.96 (m, 3H, **CH_3**–N−), 2.45–2.19 (m, 2H, −**CH_2**–

CH_3), 1.16–0.97 (m, 3H, $-CH_2-\mathbf{CH_3}$).

3.2.3 Preparation of PMMA substrate

A solution casting method was used to prepare the PMMA substrate. First, 2 g of PMMA were added to chloroform (40 mL) and stirred for 1 h at room temperature. The solution was then poured into a petri dish and left overnight at 40 °C in an oven to evaporate the chloroform. The sample was denoted as a PMMA substrate.

3.2.4 Preparation of PEI-S and PEtOx-GA-PEI-S

The method for modifying the surface of the PMMA substrate is based on the procedure presented by Bai et al,[36] but some changes were introduced. First, the PMMA substrate was treated in NaOH solution (1 mol L^{-1}) at 60 °C for 30 min to hydrolyze the ester groups on the surface. The next step consisted of washing with distilled water for 5 min and drying the substrate in an oven. The substrate was then immersed in 1.0% PEI solution (wt%) in borate buffer (0.1 mol L^{-1}, pH 11.5) at room temperature for 1 h, and then washed again. After drying, the PEI-S was ready for use. The Bai procedure is described basically in one-step modification, in which free amino groups of PEI react with ester groups of the PMMA surface, resulting in amide groups that anchor PEI on the polymer surface. However, in this procedure, an improved result compared to the Bai procedure is attributed to two effects: surface cleaning and improvement of the electrostatic adhesion of PEI. The hot base promotes the hydrolysis of methyl ester groups on the PMMA surface. This results in surface hydration and consequent solubilization of the polymeric chain, which had a remarkable improvement on the PEI immobilization. The second effect is related to the augmentation of anionic carboxylate groups on the surface, which initially promotes the electrostatic retention of PEI through the residual amino groups. The final immobilization of PEI is achieved by the formation of amide groups involving the PMMA chains as well as by cross-linking. The PEI-S films were immersed in different concentrations of PEtOx-GA (0.5, 1.0, 1.5, 2.0, 2.5, and 3.0 mg mL^{-1}) to functionalize PEtOx-GA-PEI-S films (**Scheme 3-1**), in which PEtOx-GA was dissolved in phosphate buffer solution (pH 7.4).

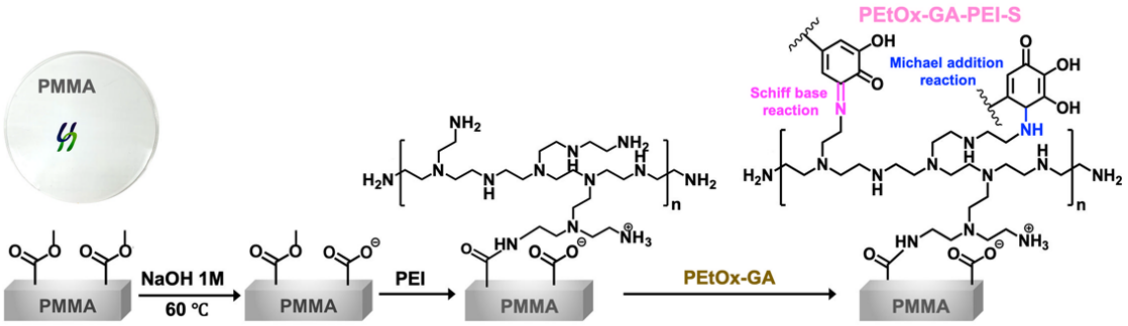

Scheme 3-1. Schematic representation of PEtOx-GA-PEI-S formation.

3.2.5 Characterization

FTIR measurements of the PEtOx and PEtOx-GA powders were recorded in the range 4000–500 cm^{-1} at a resolution of 1 cm^{-1} using a Nicolet iS5 spectrometer (Thermo Scientific, MA, USA) equipped with an iD5 ATR attachment. PEtOx and PEtOx-GA powders were analyzed by proton nuclear magnetic resonance (^{1}H NMR) spectroscopy using a JNM-ECS400 instrument (400 MHz, JEOL Ltd., Tokyo, Japan) and CD_3OD as the solvent. The surface morphology of the substrate, PEI-S, and PEtOx-GA-PEI-S films was observed by SEM (SU3500; Hitachi, Tokyo, Japan) at an accelerating voltage of 15 kV. Before analysis, the substrate, PEI-S, and PEtOx-GA-PEI-S films were dried and coated with a gold layer using an MSP-1S (Vacuum Device Inc., Tokyo, Japan). AFM measurement (SPI3800N/SPA-400, Seiko Instruments Inc., Tokyo, Japan) was to analyze the morphology of the PMMA substrate, PEI-S, and PEtOx-GA-PEI-S film. The water contact angles of the PMMA substrate, PEI-S, and PEtOx-GA-PEI-S film were determined using a Drop Master DM300 (Kyowa Interface Science, Saitama, Japan). A water droplet (1.0 mL) was dropped onto the surface of the films (1 cm × 4 cm), and the contact angle of each film was determined in five different positions. The average values have been reported. The surface chemical compositions of the PEtOx-GA powder, PMMA substrate, and PEtOx-GA-PEI-S film were determined using XPS (JEOL JPS-9010MC, Tokyo, Japan). The XPS inert parameters included the power of analysis (wide: 75 W, narrow: 150 W) and monochromatic Al Kα.[37] The survey and high-resolution XPS spectra were obtained at fixed analyzer pass energies of 160 eV and 10 eV, respectively. Peak-differentiation-imitating analysis was performed by the CasaXPS Version 2.3.15 computer program.

3.2.6 Protein adsorption properties

BSA (isoelectric point (pI)=4.7, 0.5 mg mL^{-1}) was used to conduct protein adsorption on the substrate, PEI-S, and PEtOx-GA-PEI-S surfaces. The films with the area of 1 × 2 cm^2 for each were washed by phosphate buffer at 37 °C for 1 h and then immersed in the protein solutions at 37 °C for different times (0-24 h, and 144 h). Different concentrations (0.25, 0.5, 1.0, 2.0, 4.0, and 8.0 mg mL^{-1}) of BSA were also discussed. At the same time, the protein adsorption effect of PEtOx-GA concentrations (0.5, 1.0, 1.5, 2.0, 2.5, and 3.0 mg mL^{-1}) was also investigated. The amounts of proteins adsorbed on the substrate, PEI-S, and PEtOx-GA-PEI-S films were determined by the modified dye-interaction method.[38] When CBBG binds with proteins, the reddish-violet color of CBBG changes to blue. For the preparation of the dye solution, CBBG (25 mg) was dissolved in 12.5 ml of ethanol (95%). Phosphoric acid (25 ml, 85% w/v) was added to the dye solution and diluted with distilled water (250 ml). Protein solutions (100 μL) of known concentration were added to the dye solution. The protein-dye solutions were kept for 10 min and centrifuged at 15,000× rpm for 20 min. In this process, protein-CBBG complexes were precipitated and free CBBG remained in the upper layer. The absorbance of supernatants at 465 nm was used for the standard calibration, The dye solution (3 ml) was added to a test tube and protein-absorbed films were immersed in the dye solution, after 3 h reaction, films were removed and the absorbance was measured at 595 nm using microplate reader (SH-9000Lab, Yamato Scientific co., ltd., Tokyo, Japan). The amounts of proteins adsorbed on the films were calculated based on the standard calibration. Lysozyme (pI=10.5, 0.5 mg mL^{-1}), myoglobin (pI=7.0, 0.5 mg mL^{-1}) and bovine plasma were also used to investigate the protein adsorption properties of the substrate, PEI-S, and PEtOx-GA-PEI-S films.

3.3 Results and discussion

3.3.1 Preparation of PEtOx-GA powder

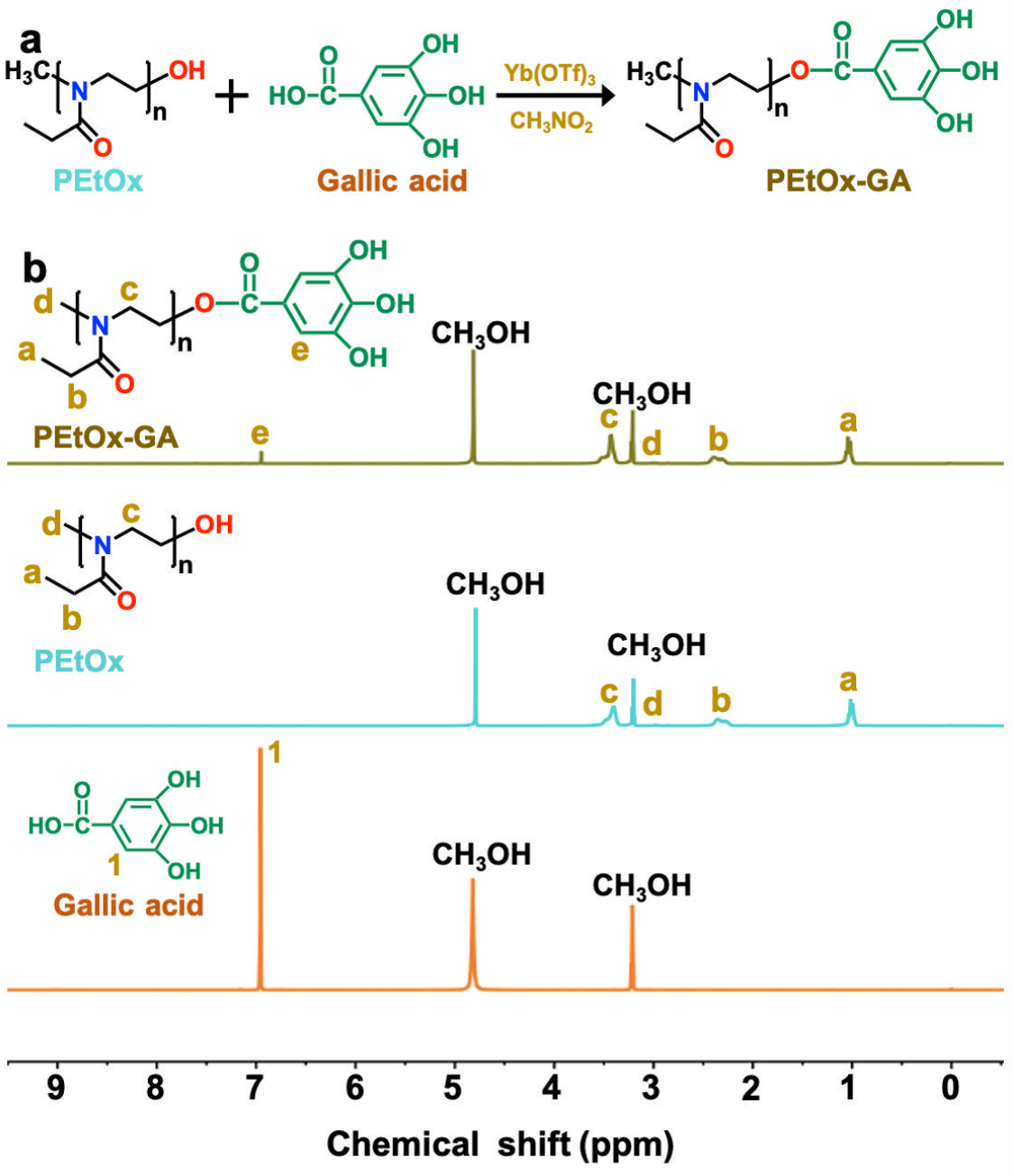

Figure 3-1. (a) The synthesis process of PEtOx-GA. (b) ^{1}H NMR spectra (400 Hz, solvent: CD_3OD) of Gallic acid, PEtOx, and PEtOx-GA powders.

PEtOx-GA was prepared by rapid and practical catalytic esterification by modification of PEtOx with GA. This synthesis process used a solvent (CH_3NO_2) and a Lewis catalyst

($Yb(OTf)_3$). As shown in **Table 3-1**, the recovery of $Yb(OTf)_3$ was 70%. In **Figure 3-1b**, the characteristic peaks of GA can be observed in the ^{1}H-NMR spectrum. The characteristic peaks of the galloyl groups appear at 6.98 ppm. The degree of substitution (DS) was calculated by comparing the integrated area of the aromatic C−H peaks in the galloyl groups with the area of the proton peak assigned to methylene in the PEtOx at approximately 2.45–2.19 ppm. The DS of PEtOx-GA was found to be 85%. The ^{1}H-NMR spectra indicate the successful grafting of galloyl groups onto the PEtOx backbone.

Table. 3-1. Reuse of $Yb(OTf)_3$ in Etherification in PEtOx-GA.

No. of times	Yield/%[a]	Recovery of $Yb(OTf)_3$/%
1	74	72
2	72	70
3	68	70

[a]Yields were determined by HPLC using the internal standard method.

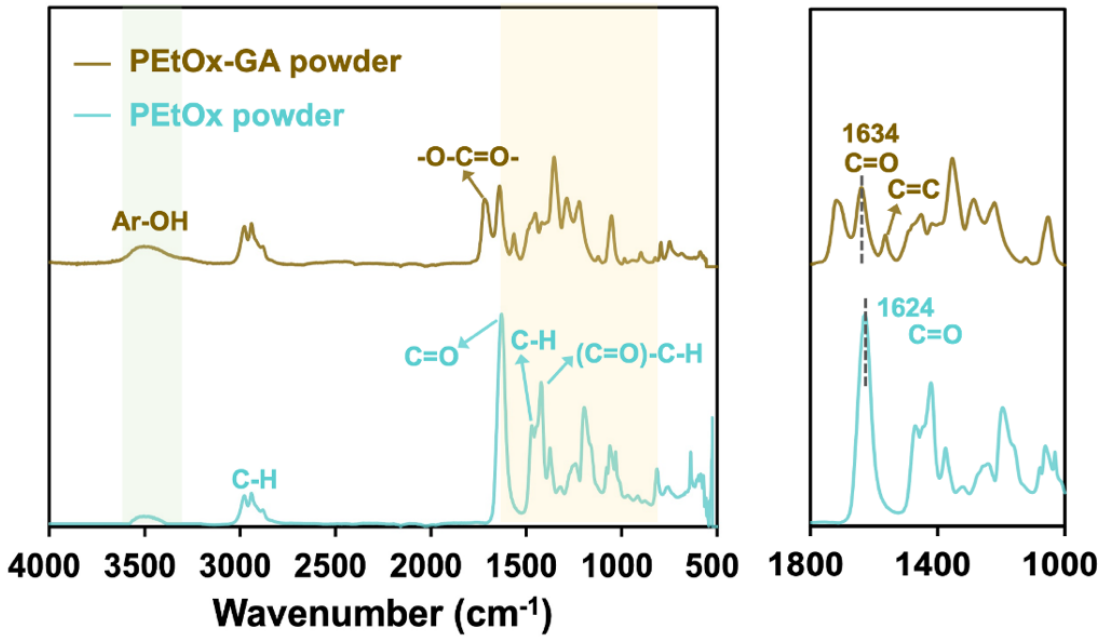

Figure 3-2. FTIR spectra of PEtOx and PEtOx-GA powders. A magnified view of the spectrum in the range of 1800–1000 cm^{-1} is shown on the right.

Figure 3-2 shows the FTIR spectra of PEtOx and PEtOx-GA, where the peak at 1624 cm^{-1} assigned to the carbonyl stretching is typical for PEtOx. After the formation of PEtOx-GA, this

peak shifts to a higher wavenumber at 1634 cm^{-1} due to the presence of hydrogen bonding between the −C=O of PEtOx and the -OH groups of GA. After the synthesis of PEtOx-GA, stretching of the C=O functional group appears at 1718 cm^{-1} (ester carbonyl groups). The presence of this new peak in the PEtOx-GA powder confirms the rapid and catalytic esterification to produce galloyl groups.

3.3.2 Preparation of PEtOx-GA-PEI-S film

The autoxidation reaction of the three phenolic hydroxyl groups in PEtOx-GA is shown in **Scheme 3-2**. The phenolic hydroxyl groups of PEtOx-GA make it susceptible to degradation via autoxidation. Under normal physiological conditions (pH 7.4, 37 °C), the phenolic hydroxyl groups are autoxidized and converted to an *o*-quinone. The amino groups in PEI-S then react with the C=O or C=C−C=O structures in the *o*-quinone through Michael addition and Schiff-base reactions (**Scheme 3-1**).[39,40] This is confirmed by the FTIR and XPS results of the PEtOx-GA-PEI-S film. In the FTIR spectrum of the PEtOx-GA-PEI-S film (**Figure 3-3a**), the peak at 3496 cm^{-1} corresponds to the stretching peak of phenolic hydroxyl. The new peaks at 1650 and 1634 cm^{-1} belong to C=N and C=O in the C=O−NH group. The C=O peak in the ester carbonyl groups appears at 1718 cm^{-1}. The peak at 1510 cm^{-1} is attributed to the vibration of C=C in the benzene ring skeleton.

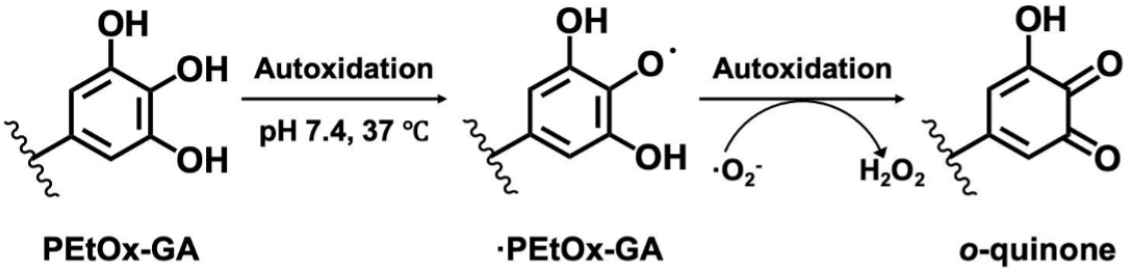

Scheme 3-2. Schematic representation of the autoxidation of phenolic hydroxyl groups (PEtOx-GA): formation of o-quinone.

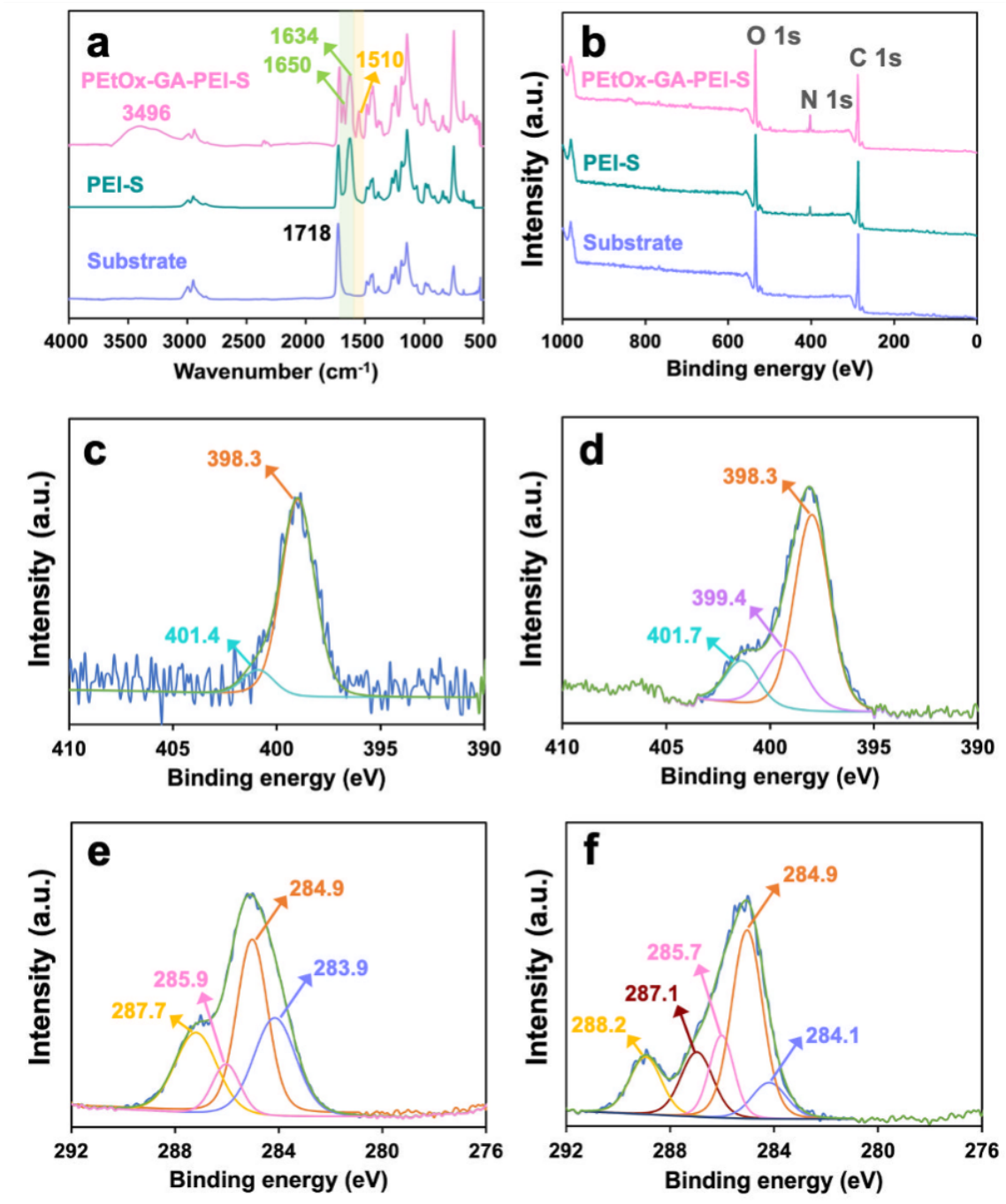

Figure 3-3. (a) FTIR spectra of PEtOx-GA-PEI-S, PEI-S, and substrate films. XPS spectra of PEtOx-GA-PEI-S, PEI-S, and substrate films: (b) wide-spectra; N 1s spectra of (c) PEI-S film and (d) PEtOx-GA-PEI-S film; C 1s spectra of (e) PEtOx-GA powder and (f) PEtOx-GA-PEI-S film.

The atomic chemical bonding states of the substrate, PEI-S, and PEtOx-GA-PEI-S films were characterized by XPS. The wide XPS spectra confirm that a reaction takes place between PEtOx-GA and PEI-S because the occurrence of the N 1s peak is observed in the spectrum of the PEtOx-GA-PEI-S film (**Figure 3-3b**). The atomic composition of the substrate, PEI-S, and

PEtOx-GA-PEI-S films is summarized in **Table 3-2**. The total nitrogen compositions of the PEI-S and PEtOx-GA-PEI-S film surfaces are 2.23 % and 4.57 %, respectively. From the high-resolution XPS of N 1s of the PEI-S and PEtOx-GA-PEI-S films (**Figure 3-3c and 3-3d**), the peak at 398.3 eV belongs to the C−N bond created by Michael addition and the intrinsic C−N bond from PEtOx-GA and PEI-S. The wide peak in the PEtOx-GA-PEI-S film at 399.4 eV is assigned to C=N, which is attributed to the Schiff-base reaction between PEtOx-GA and PEI-S. The peaks at 401.4 and 401.7 eV are attributed to $-NH_3^+$, one from the intrinsic group in PEI-S and the other one from the reaction between galloyl groups in PEtOx-GA and $-NH_2$ in PEI-S.

Table 3-2. Atomic compositions of the substrate, PEI-S, and PEtOx-GA-PEI-S films.

Species		Substrate mass conc. (%)	PEI-S mass conc. (%)	PEtOx-GA-PEI-S mass conc. (%)
C 1s	C	41.58	42.64	40.17
	C−O	17.02	16.45	16.98
	O−C=O	13.41	11.03	13.24
	total C 1s	72.11	70.12	70.39
O 1s	O	16.41	14.54	13.26
	O=C	11.58	12.12	11.78
	total O 1s	27.89	26.66	25.04
N 1s	C−N	-	1.87	2.74
	NH_3^+	-	0.36	0.97
	C=N	-	-	0.86
	total N 1s	-	2.23	4.57

The high-resolution C 1s spectra of the PEtOx-GA powder and PEtOx-GA-PEI-S film also confirm the reactions (**Figure 3-3e and 3-3f**). For the C 1s spectra of PEtOx-GA, the peaks at 284.9, 283.9 eV, and 285.9 are assigned to C−C, C=C, and aromatic C−OH bonds, respectively. The peak at 287.7 eV is attributed to the C=O in the galloyl groups. In the C 1s spectrum of the PEtOx-GA-PEI-S film, the C=C bond shifts to 284.1 eV due to the Schiff-base reaction and Michael addition, rearranging the conjunction of the C=C bonds of the benzene ring. The peak at 285.7 eV is assigned to C−OH and C−N, which are created by rearrangement of the benzene

ring and by Michael addition, respectively.[41] The new peak at 287.1 eV is assigned to the C=N bond, which contributes to the Schiff-base reaction. The results of FTIR and XPS confirm that the Michael addition and Schiff-base reaction occurred during the formation of the PEtOx-GA-PEI-S film.

The morphologies of the substrate, PEI-S, and PEtOx-GA-PEI-S films characterized by SEM and AFM are shown in **Figures 3-4**. The surface morphology of the PEtOx-GA-PEI-S film was smoother than that of the substrate. The root means square (RMS) roughness of the substrate, PEI-S, and PEtOx-GA-PEI-S films were 83.95, 66.17, and 27.26 nm, respectively. This is the result of PEI-S reacting with galloyl groups from PEtOx-GA to form a dense layer on the surface of the PEtOx-GA-PEI-S film.

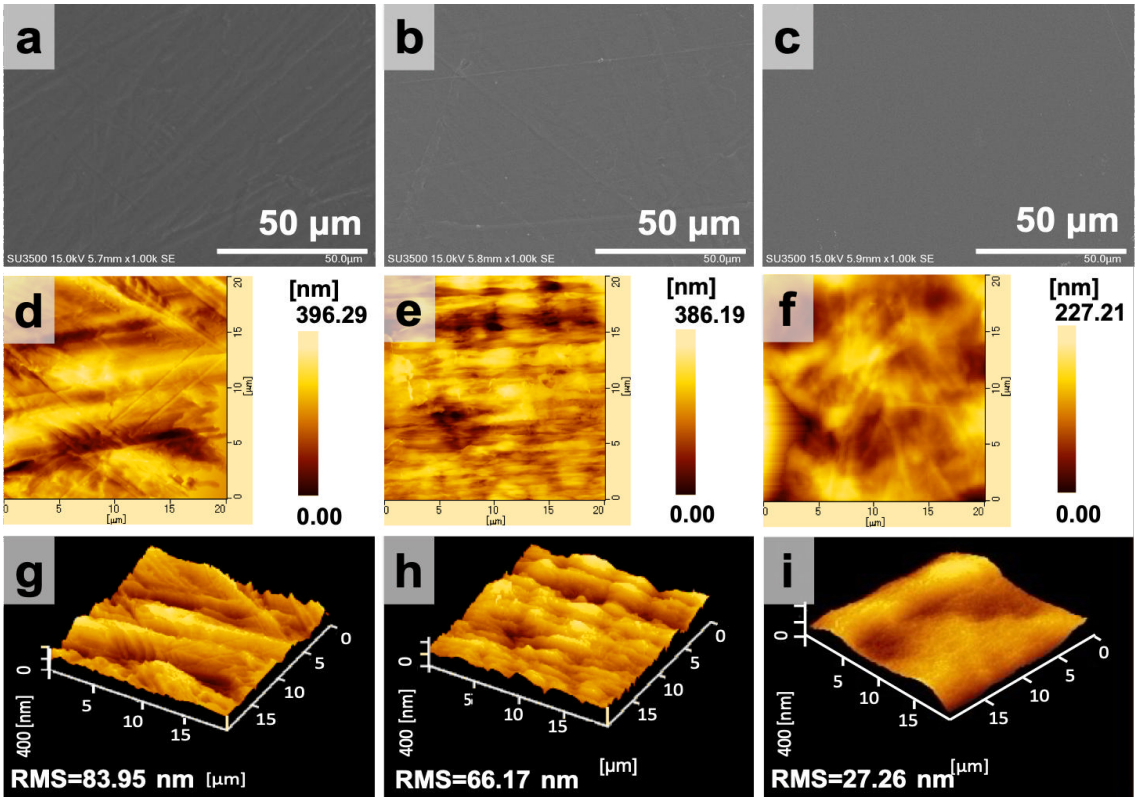

Figure 3-4. SEM images (a–c), AFM height image 2D (d–f) and 3D (g–i) of the substrate (a, d, and g), PEI-S (b, e, and h), and PEtOx-GA-PEI-S films (c, f, and i).

The transmittance is also an important parameter to examine for application in biomedical materials.[42] In the case of optical transmittance, the wavelength from 400 to 800 nm was the

visible range, and the air was regarded as a reference. The optical transmittance was measured using the light source with 600 nm wavelength, which is the central wavelength of the visible range. The UV-vis transmittance values at ~600 nm of the substrate, PEI-S, and PEtOx-GA-PEI-S films were 91 %, 82 %, and 71 %, respectively (**Figure 3-5a**). The transmittance of the PEtOx-GA-PEI-S film was lower than that of the substrate because of the grafted PEtOx-GA. Hydrophilicity/hydrophobicity is the primary factor that affects protein adsorption. [43] Bi, et al.[44] reported that PMMA/PEG copolymers minimize nonspecific adsorption. In this study, we use PEtOx-GA grafted on the surface of PEI-S to increase hydrophilicity. As shown in **Figure 3-5b**, the surface of the PEtOx-GA-PEI-S film is hydrophilic, with a water contact angle ranging from 40° to 45°, which is much lower than that of the substrate (98° to 96°) and PEI-S (72° to 76°) films. A smaller contact angle is commonly regarded as indicating a greater tendency for water to wet the membrane, as well as higher hydrophilicity. The chemical composition may account for the hydrophilic surface of the PEtOx-GA-PEI-S film. As shown in **Figure 3-3a**, amino, carboxyl, and hydroxyl groups are detected on the PEtOx-GA-PEI-S film, which results in a highly hydrophilic surface of the film. The introduction of zwitterionic groups effectively enhances the hydrophilicity and improves the antifouling properties of the PEtOx-GA-PEI-S film.

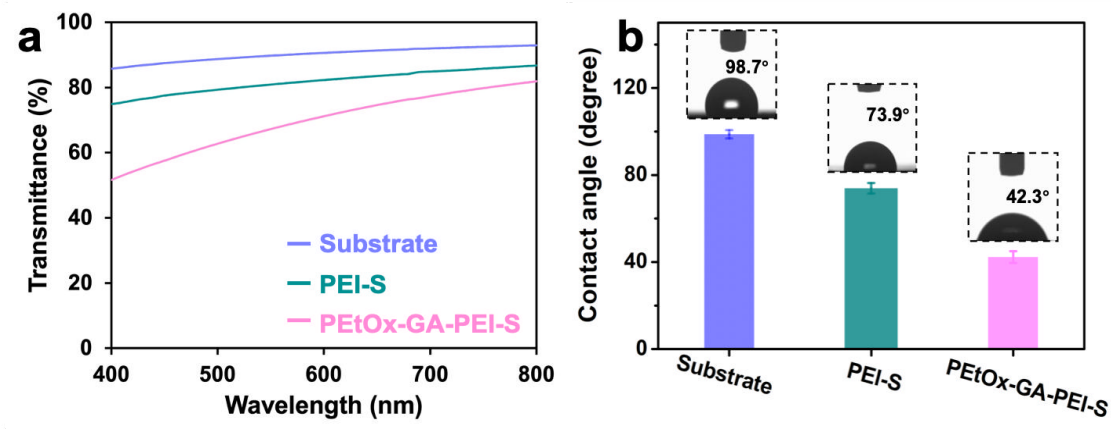

Figure 3-5. Transmittance (a) and water contact angles (b) of the substrate, PEI-S, and PEtOx-GA-PEI-S films. Data are shown as the mean ± standard deviation (n = 3).

3.3.3 Protein adsorption properties

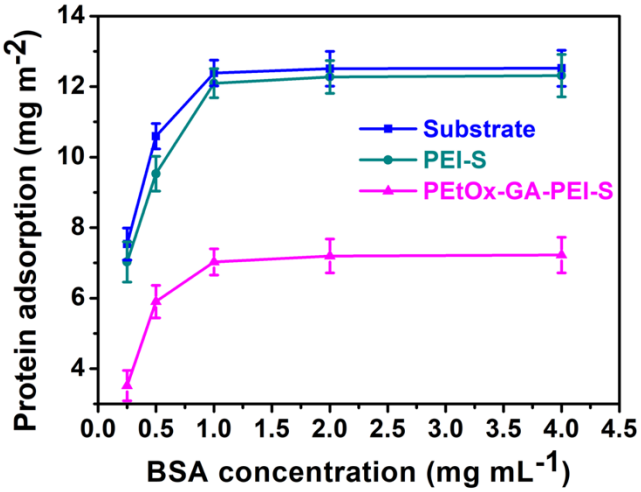

Figure 3-6. Effect of various initial BSA concentration on adsorption performance. Data are shown as the mean ± standard deviation (n = 3).

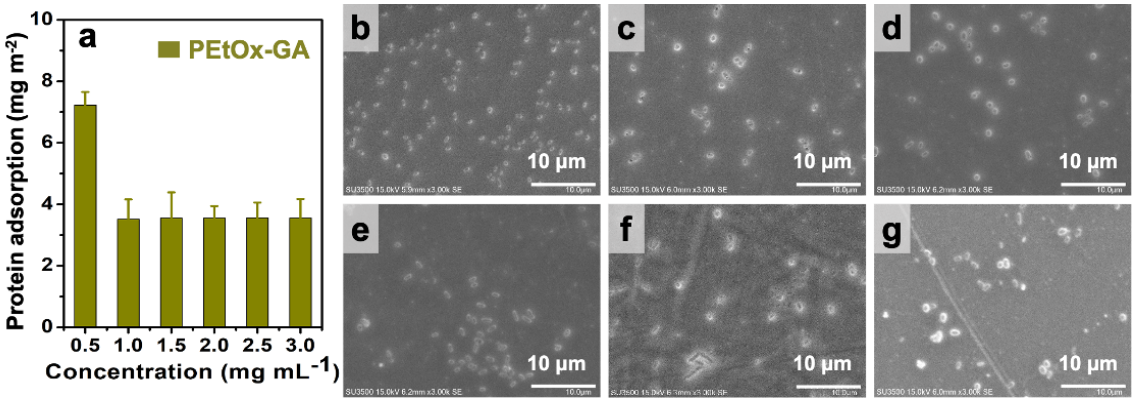

Figure 3-7. The adsorption capacity of PEtOx-GA-PEI-S films immersed in BSA solution (6 h) with various PEtOx-GA concentrations. SEM images of different concentrations: 0.5 (b), 1.0 (c), 1.5 (d), 2.0 (e), 2.5 (f), and 3.0 mg mL^{-1} (g) of PEtOx-GA-PEI-S films immersed in BSA solution. Data are shown as the mean ± standard deviation (n = 3).

BSA was used as the model protein to investigate static protein adsorption on the surface of the substrate, PEI-S, and PEtOx-GA-PEI-S films. BSA was also chosen to investigate the adsorption isotherms. It is observed from **Figure 3-6** that on different films (substrate, PEI-S, and PEtOx-GA-PEI-S), the adsorption amount of BSA was significantly increased when the BSA concentration was lower than 1 mg mL^{-1}, and the adsorption amount was then turned to a plateau in the BSA concentration range of 1-4 mg mL^{-1}. Equilibrium BSA adsorption capacity of 12.59 mg m^{-2}, 12.33 mg m^{-2}, 7.21 mg m^{-2} were obtained on the substrate, PEI-S, and PEtOx-GA-PEI-S films, respectively. Thus, we choose the protein concentration of 0.5 mg mL^{-1} for

the protein adsorption studies. In order to discuss the effect of adding different concentrations of PEtOx-GA on the protein adsorption properties of PEtOx-GA-PEI-S films, different concentrations of PEtOx-GA (0.5, 1.0, 1.5, 2.0, 2.5, and 3.0 mg mL^{-1}) were prepared. As shown in **Figure 3-7a**, concentrations above 1.0 mg mL^{-1} have better protein antifouling properties (BSA adsorption was 3.48 mg m^{-2}, BSA solution: pH 7.4, 0.5 mg mL^{-1}; immersion time: 6 h) because lower concentrations of PEtOx-GA could not provide enough functional groups for grafting on the PEI-S surface. Meanwhile, for concentrations of PEtOx-GA from 1.5 to 3.0 mg mL^{-1}, the results show no significant difference after the BSA antifouling test (the BSA adsorption capacity was ~3.55 mg m^{-2}), because the functional groups reach saturation on the PEtOx-GA-PEI-S and they do not impact the hydrophilicity and protein antifouling properties. SEM images from **Figure 3-7b-7g** were also proved that the concentration of PEtOx-GA was 0.5 mg mL^{-1} was covered a larger amount of protein clustered globules than other concentrations.

When the substrate, PEI-S, and PEtOx-GA-PEI-S (PEtOx-GA: 1.0 mg mL^{-1}) films were immersed in BSA solution (pH 7.4, 0.5 mg mL^{-1}) for different times (4, 8, 24, and 144 h), the PEtOx-GA-PEI-S film showed the best antifouling properties. As shown in **Figure 3-8**, the surface of the substrate was covered by a large number of protein clustered globules, indicating that proteins were easily adsorbed on hydrophobic surfaces. There is a high-density layer of water molecules around the protein molecules, and the protein will fold or remodel on a hydrophobic surface, so it is easily loaded onto a hydrophobic surface. Meanwhile, the PEI-S film has fewer protein antifouling properties than the substrate because of the amino groups on the surface. The surface of the PEtOx-GA-PEI-S film is covered by the smallest area of proteins compared to the substrate and PEI-S films because the protein is not easily fixed and adsorbed on hydrophilic surfaces. The repulsive force of the water molecule layer is not conducive to adsorption on a hydrophilic surface.

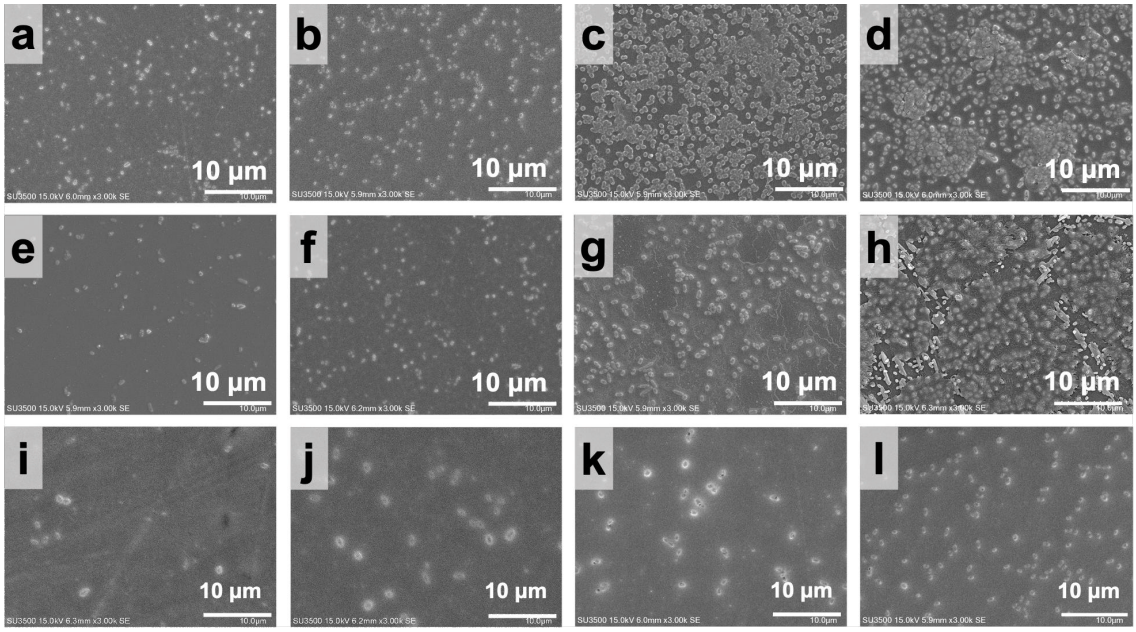

Figure 3-8. SEM images of the substrate (a–d), PEI-S (e–h), and PEtOx-GA-PEI-S (i–l) immersed in BSA solution for different times: 4 (a, e, and i), 8 (b, f, and j), 24 (c, g, and k), and 144 h (d, h, and l).

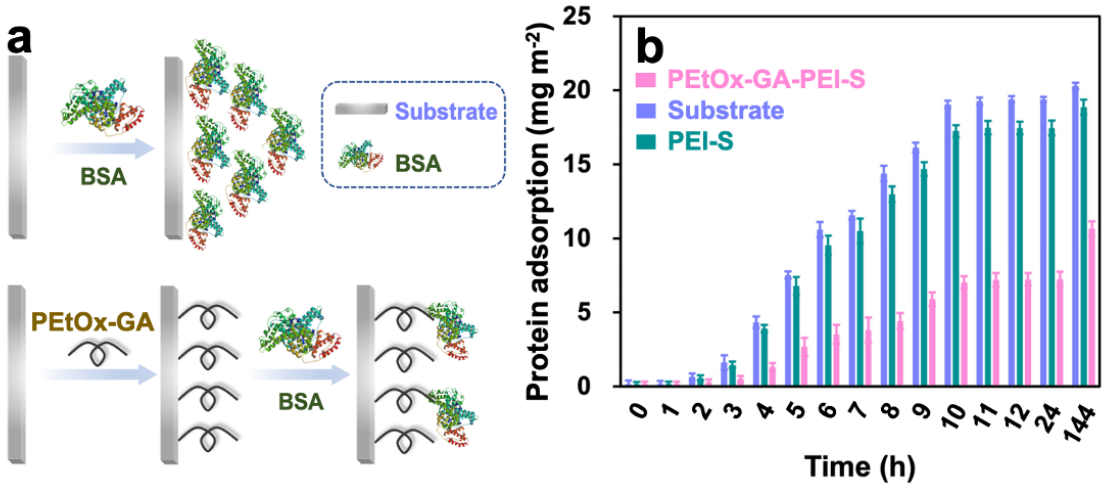

Figure 3-9. (a) Scheme of the BSA adsorption process for the substrate and PEtOx-GA-PEI-S films. (b) The adsorption capacity of the substrate, PEI-S, and PEtOx-GA-PEI-S films with BSA at various times. Data are shown as the mean ± standard deviation (n = 3).

Figure 3-9 shows the correlation between the substrate, PEI-S, and PEtOx-GA-PEI-S films with protein adsorption of BSA. Reduced absorption is shown after PEtOx-GA functionalization when compared to that of the substrate film. After 4 h, the amount of BSA increases on the surface of the substrate and PEI-S film compared to the PEtOx-GA-PEI-S film, as also shown in **Figure 3-8a, 8e,** and **8i**. From 10 to 24 h, BSA on the surface of all three films

reaches adsorption saturation, and the adsorption capacity does not significantly increase. However, after 144 h, the amount of BSA on all the films increases because of protein deposition over a long time. The PEtOx-GA-PEI-S film exhibits the best antifouling property. In relative terms, ~10% less BSA is adsorbed onto the PEI-S film and ~70% less on the PEtOx-GA-PEI-S film. For comparison with BSA (pI=4.7), proteins with different pI values, such as lysozyme (0.5 mg mL^{-1}, pI=10.5) and myoglobin (0.5 mg mL^{-1}, pI=7.0) were also tested for protein adsorption on PEtOx-GA-PEI-S films. As shown in **Figure 3-10**, these two proteins also have antifouling properties after 24 h, showing ~65% less absorption of lysozyme, and ~30% less absorption of myoglobin on the PEtOx-GA-PEI-S film. Many of the polymers used in medical applications or as drug delivery systems come into close contact with plasma.[45] Therefore, the influence of plasma adsorption on the films was investigated. As shown in **Figure 3-10a**, the plasma adsorption amount on the functional film was reduced to 23.12 mg m^{-2}, indicating the adsorption of plasma on the functional film could be prevented. SEM images of **Figure 3-10b, 10e,** and **10h** for lysozyme and **Figure 3-10c, 10f,** and **10i** for myoglobin were also proved substrate and PEI-S films were easy covered a larger amount of protein clustered globules than functional films. The interaction mechanism of the three proteins is different [46] (mixed mode for myoglobin and lysozyme, hydrophilic for BSA). Surface hydrophilicity plays an important role in BSA adsorption and resistance to elution by ionic strength changes regardless of the surface charge. As for myoglobin and lysozyme, the effect of surface charge in the adsorbed protein plays an important role in hydrophilic property. Thus, the protein adsorption effect of the hydrophilic functional film surfaces shows that BSA has less adsorption than myoglobin and lysozyme. These results indicate that the adsorption of all three proteins is reduced on the PEtOx-GA-PEI-S films when the proteins have different isoelectric points. Overall, the specific conjugation of galloyl-terminated polymers functionalizes the surfaces by a grafting strategy to significantly reduce surface-protein adsorption.

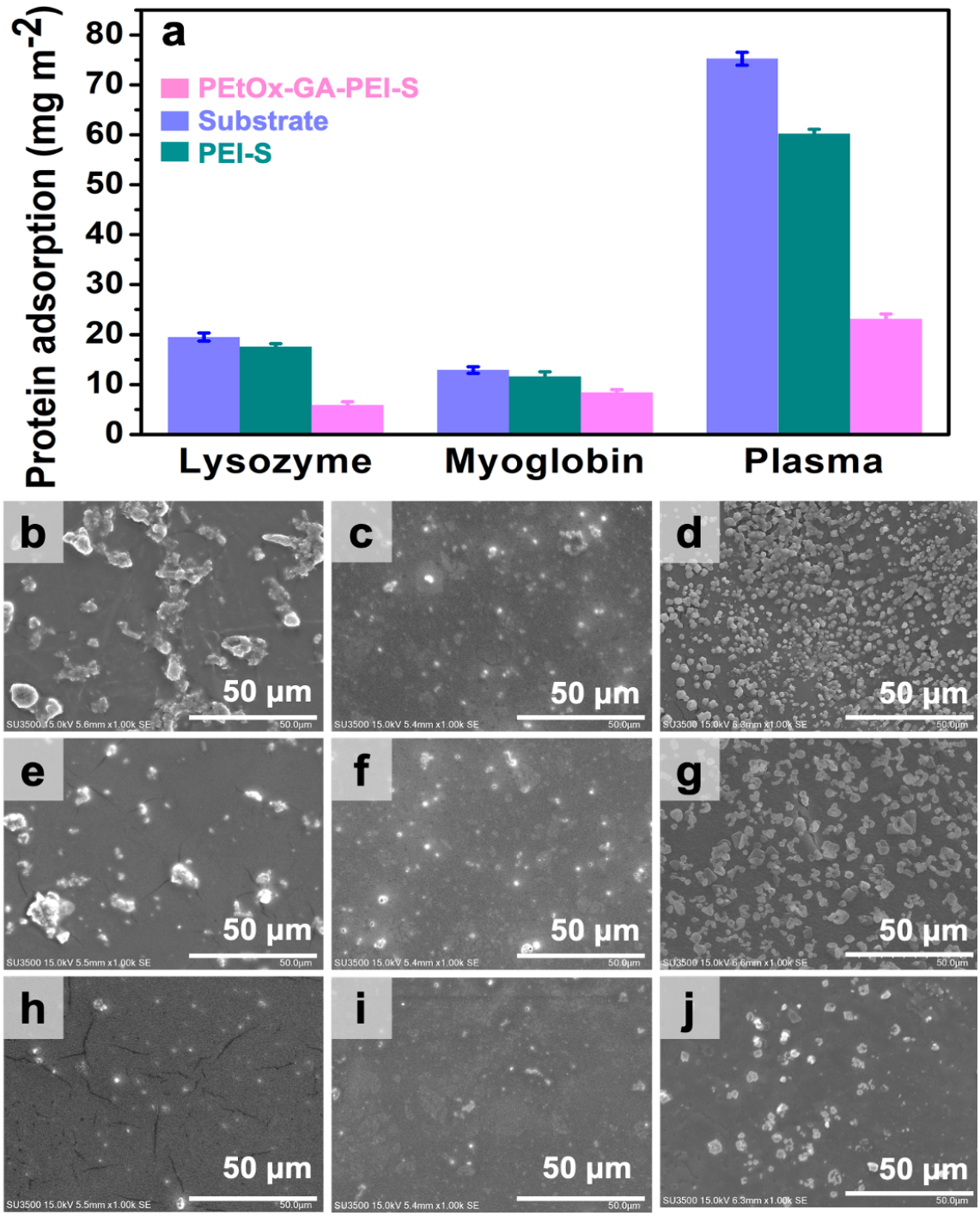

Figure 3-10. (a) Adsorption capacity of substrate, PEI-S, and PEtOx-GA-PEI-S films immersed in lysozyme, myoglobin, and plasma for 24 h, respectively. SEM images of Substrate (b–d), PEI-S (e-g), and PEtOx-GA-PEI-S (h-j) immersed in lysozyme (b, e, and h), myoglobin solution (c, e, and g), and plasma (d, g, and j) for 24 h, respectively. Data are shown as the mean ± standard deviation (n = 3).

3.4 Conclusions

In conclusion, bio-based materials increasing in biomedical applications because of their sustainable and renewable alternative to their chemical counterparts. The PEtOx-GA-PEI-S functional film with good prevention of protein absorption was successfully developed using a PEtOx-GA graft on PEI-modified PMMA substrate via Michael addition and Schiff-base reaction. During the formation of the PEtOx-GA-PEI-S functional film, bio-based material (PEtOx-GA) was synthesized using a rapid and practical esterification method. As compared the protein antifouling properties with other similar polymers (e.g., Xu et al. [47] reported PFMA-*b*-PEG brusher could decrease BSA adsorption on the film by 45%), the new synthesized PEtOx-GA has less protein adsorption. This polymer reduced BSA, lysozyme, and myoglobin adsorption by ~70%, ~65%, and ~30% on PEtOx-GA-PEI-S functional films, respectively. PEtOx-GA also shows significantly better antifouling character when challenged against plasma. This study provides a new design for functional antifouling films that employ PEtOx-GA as an antifouling component to achieve reliable antifouling films, which would help to better understand antifouling behavior and design more effective antifouling materials and surfaces. Thus, bio-based polymer, which has good water solubility and observed low fouling nature can offer an effective approach for a hydrophilic surface design to reduce biofouling, which would facilitate the widespread applications of the PMMA film in complex biological analysis.

3.5 References

1. K. Rahmani, A. Fathi, M. Rabiee, *Int. J. Adv. Manuf.*, 2016, **84**, 2649–2657.
2. S. Krishnan, J. Weinman, K. Ober, *J. Mater. Chem.*, 2008, **18**, 3405–3413.
3. W. Chen, V. Lee, C. Juan, *Carbohydr. Polym.*, 2016, **151**, 1210–1219.
4. G. Pahla, A. Mamvura, F. Ntuli, *south african J. Chem. Eng.*, 2017, **24**, 168–175.
5. Q. Wei, T. Becherer, S. Uberti, *Angew. Chem. Int. Ed.*, 2014, **53**, 8004–8031.
6. R. Qu, W. Zhang, N. Liu, *ACS Sustain. Chem. Eng.*, 2018, **6**, 8019–8028.
7. R. Meyers, W. Grinstaff, *Chem. Rev*., 2012, **112**, 1615–1632.
8. J. Hasan, R. Crawford, E. Ivanova, *Trends Biotechnol.*, 2013, **31**, 295–304.
9. D. Pranantyo, Q. Xu, G. Neoh, *Biomacromolecules*, 2015, **16**, 723–732.
10. H. Ejima, J. Richardson, K. Liang, Science, 2013, **341**, 154–157.
11. P. Schultz, A. Bendick, R. Holm, Biofouling, 2011, **27**, 87–98.
12. A. Bettencour, J. Almeida, *J. Microencapsul.*, 2012, **29**, 353–367.
13. K. Landfester, V. Mailänder, *Expert. Opin. Drug. Deliv.*, 2013, **10**, 593–609.
14. C. McGlothin, C. Rosu, L. Jiang, *Surfaces and Interfaces*, 2019, **17**, 100370.
15. C. Gillain, G. Rouxhet, *Nano. Lett.*, 2001, **1**, 245–251.
16. J. Liu, T. Pan, T. Woolley, *Anal. Chem.*, 2004, **76**, 6948–6955.
17. L. Prime L, M. Whitesides M, *Science*, 1991, **252**, 1164–1167.
18. S. Krishnan, J. Weinman, K. Ober, *J. Mater. Chem.*, 2008, **18**, 3405–3413.
19. D. Falconnet, G. Csucs, M. Grandin, *Biomaterials*, 2008, **27**, 3044–3063.
20. B. Damodaran, S. Murthy, *Biomater. Res.*, 2016, **20**, 1–11.
21. I. Banerjee, C. Pangule, S. Kane, *Adv. Mater.*, 2011, **23**, 690–718.
22. N. Zhang, T. Pompe, I. Amin, *Macromol. Biosci.*, 2012, **12**, 926–936.
23. L. Tauhardt, K. Kempe, M. Gottschaldt, *Chem. Soc. Rev.*, 2013, **42**, 7998–8011.
24. K. Kempe, L. Ng, T. Gunawan, *Adv. Funct. Mater.*, 2014, **24**, 6187–6194.
25. L. Tauhardt, M. Frant, D. Pretze, *J. Mater. Chem. B*., 2014, **2**, 4883–4893
26. D. Pranantyo, Q. Xu, G. Neoh, *Biomacromolecules*, 2015, **16**, 723–732.

27. H. Ejima, J. Richardson, K. Liang, *Science*, 2013, **341**, 154–157.
28. S. Sileika, G. Barrett, R. Zhang, *Angew. Chem. Int. Ed.*, 2013, **52**, 10766–10770.
29. A. Sundaramurthy, M. Vergaelen, S. Maji, *Adv. Healthc. Mater.*, 2014, **3**, 2040–2047.
30. C. Maan, H. Hofman, M. Vos, *Adv. Funct. Mater.*, 2020, **30**, 2000936.
31. H. Yoon, J. Chung, W. Lee, *Joint Bone Spine*, 2013, **80**, 274–279.
32. F. Kitagawa, K. Kubota, K. Sueyoshi, *Sci. Technol. Adv. Mater.*, 2006, **7**, 558–565.
33. J. Ouyang, K. Zhu, Z. Liu, Oxid. Med. Cell. Longev., 2020, **2020**.
34. H. Wen, Y. Hsu, T. Asoh, *Polym. Degrad. Stab.*, 2020, **178**, 109215.
35. S. Shishido, R. Miyano, T. Nakashima, *Sci. Rep*., 2018, **8**, 1–11.
36. Y. Bai, W. Huang, S. Yang, *Biotechnol. Bioeng*., 2007, **98**, 328–339.
37. C. Jiao, Z. Zhang, J. Tao, *RSC Adv.*, 2017, **7**, 27787–27795.
38. M. Redinbaugh, W. Campbell, *Anal. Biochem.*, 1985, **147**, 144–147.
39. H. Lee, M. Dellatore, M. Miller, *Science*, 2007, **318**, 426–430.
40. S. Hong, F. Schaber, K. Dening, *Adv. Mater.*, 2014, **26**, 7581–7587.
41. Q. Cheng, X. Wang, J. Guo, *ACS Sustain. Chem. Eng.*, 2018, **6**, 1881–1890.
42. S. Min, J. Cho, *Int. J. Mol. Sci.*, 2021, **22**, 773.
43. Y. Liu, H. Huang, P. Huo, *Carbohydr. Polym.*, 2017, **165**, 266–275.
44. H. Bi, S. Meng, Y. Li, *Lab. Chip.*, 2006, **6**, 769–775.
45. Q. Wei, T. Becherer, S. Uberti, *Angew. Chemie. Int. Ed.*, 2014, **53**, 8004–8031.
46. P. Satzer, F. Svec, G. Sekot, *Eng. Life. Sci.*, 2016, **16**, 238–246.
47. C. Maan, H. Hofman, M. Vos, *Adv. Funct. Mater.*, 2020, **30**, 2000936.

Chapter 4.

Superhydrophobic PDMS-pCA@CNWF composite with UV-resistant and self-cleaning properties for oil/water separation

4.1 Introduction

With the development of industrialization, the problem of water pollution has become a major challenge. As one of the three major types of industrial wastewater, oily wastewater is viewed as a serious environmental issue, threatening human life and the global ecosystem.[1-5] Oil/water separation is a green technology that separates oil/water mixtures to achieve waste oil recycling and sewage purification. It is widely used in wastewater treatment, domestic sewage treatment, the petrochemical industry, and other fields.[6-9] In most oil/water separation processes, the treatment of oily wastewater is inefficient and costly, and various oil/water separation materials are not able to separate every type of oily sewage simultaneously. In recent years, some research progress has been made in oil/water separation through chemical, physical, and biological treatment methods.[10-13] Although a combination of these methods can meet most of the relevant requirements for the separation of oil/water mixtures, there are also some disadvantages, such as large floor space requirement, long treatment cycles, high cost, and the possibility of secondary pollution.[14,15]

Superhydrophobic surfaces (water contact angles higher than 150°) have been rapidly developed in the past few decades to selectively filter or absorb oil from water.[16,17] Based on this principle, Boinovich et al. [18] prepared a superhydrophobic surface on an aluminum alloy surface by laser treatment and low-surface-energy molecular modification. However, problems can be experienced with commonly used organic ultrafiltration membranes and mesh materials, such as swelling and breakage, which limit their application. A superhydrophilic/underwater superoleophobic PVDF membrane prepared by Nayak et al. [19] has been successfully used to separate oil/water emulsions. However, the repeated use of this type of membrane is limited by

the problem of oil contamination, in which pore blockage is restricted after separation. Meanwhile, high energy consumption, long processing times, low separation efficiency, and the requirement for chemical additives have imposed restrictions on their practical applications.[20]

With continuously improving public awareness of environmental protection, economy, and reuse, there is an increasing demand for adsorption materials that can effectively separate oil-water mixtures. As an agricultural waste, cellulose from plants has the advantages of low price, biodegradability, high fiber strength, and porosity, and has been explored as a new type of adsorption material.[21,22] Wang et al. [23] used cotton fiber as a raw material to prepare Janus cotton cloth, which has a good separation effect on oil slicks and emulsified oil. Pi et al. [24] dipped a cotton fabric in a cross-linkable fluorine-containing copolymer material to prepare a superhydrophobic/superlipophilic cotton fabric. However, owing to the complex preparation process of fluorine-containing chemicals, the resulting fabrics have poor environmental stability, and their applications have been limited. Superhydrophobic cellulose-based materials have many disadvantages. For example, when cotton is subjected to superhydrophobic modification, it is usually susceptible to environmental influences, such as acid and alkali, high temperature, and ultraviolet light, which cause the structure of the product to be unstable and affect its long-term use. Non-woven fabrics are usually obtained from polymer slices, short or filamentary fibers, woven together into net-like structures through an air-laid process, followed by water thorn, acupuncture, or hot rolling reinforcement to finish the fabrication. Owing to the high flexibility, low density, high porosity, and low cost, non-woven fabrics are expected to be a promising high-efficiency material.[25-28]

In this study, cellulose non-woven fabric (CNWF), which has high porosity and low cost, has been used as the base material. In order to make the material unaffected by ultraviolet light, the surface of the CNWF was modified with poly(catechin) (pCA). Because pCA has strong antioxidant and antibacterial properties [29] and can be synthesized through a simple method (laccase-catalyzed polymerization). Subsequently, the superhydrophobic material PDMS-pCA@CNWF was obtained by the condensation reaction between modified CNWF

(pCA@CNWF) and hydrolysis PDMS. The morphology, surface chemical structure, and composition of CNWF, pCA@CNWF, and PDMS-pCA@CNWF were characterized by scanning electron microscopy (SEM), Fourier-transform infrared spectroscopy (FTIR), and X-ray photoelectron spectroscopy (XPS). The separation efficiency and mechanical durability of the PDMS-pCA@CNWF composite were also investigated. This superhydrophobic material could play an important role in oil/water separation in the future.

4.2 Experimental Section

4.2.1 Materials

Cellulose non-woven fabrics (CNWF) were purchased from Futamura Chemical Co., Ltd. (Aichi, Japan). Catechin, 2,2-diphenyl-1-picrylhydrazyl (DPPH) reagent, dimethylformamide (DMF), and polydimethylsiloxane PDMS were purchased from Sigma-Aldrich (Tokyo, Japan). Laccase derived from Myceliophthora was kindly donated by Novozymes Japan Ltd. Chloroform, tetrahydrofuran (THF), hydrochloric acid (HCl), sodium hydroxide (NaOH), and Oil Red O were purchased from Fujifilm Wako Pure Chemical Corporation (Tokyo, Japan). Dimethylformamide (DMF) was purchased from Nacalai Tesque Inc. (Kyoto, Japan). Methylene blue was purchased from Tokyo Chemical Industry Co., Ltd. (Tokyo, Japan). Deionized water (DI water) was used for solution preparation and dilution. All reagents were of analytical grade and used as received without further purification.

4.2.2 Enzymatic Polymerization of Catechin

Catechin (0.15 g) and laccase solution (1000 units· mL^{-1}) were added in a mixture of acetone and 0.1 M acetate buffer (pH 5) (total 30 mL), and then placed in a 50 mL flask under air. The mixture was then stirred at 25 °C.[30] After 24 h, polymer precipitates were collected by centrifugation. The product was washed twice with a mixture of water and methanol (95:5 v:v) and dried at a vacuum oven to obtain the poly(catechin) (pCA).

4.2.3 Antioxidant activity of pCA

The DPPH assay is an easy and rapid method for evaluating the antioxidant content of samples. DPPH solution (0.1 mM in ethanol, 2mL) was mixed with 2 mL of catechin/pCA in ethanol at different concentrations (2, 4, 8, 12,16, and 20 μg mL^{-1}) and incubated in the dark for 30 min. The absorbance was measured at 517 nm by using an Infinite 200 plate reader (TECAN, Männedorf, Zürich, Switzerland).[31] For time-dependent antioxidant measurements, catechin/pCA (20 μg mL^{-1}) was added to the DPPH ethanolic solution for different times (2, 4, 6, 8, 10, and 12 h) to measure the absorbance. The % DPPH radical scavenging activity was

calculated using Eq. (1):

$$\boldsymbol{Scavenging}\ (\%) = \frac{\mathbf{Abs(control) - Abs(sample)}}{\mathbf{Abs(control)}} \times \mathbf{100}\ \mathbf{(1)}$$

where Abs(control) and Abs(sample) indicate the absorbance of the blank and the reaction solution, respectively.

4.2.4 pCA-modified CNWF

CNWF samples (6 cm × 6 cm) were cleaned three times with DI water and ethanol to remove impurities and oil from the surface. After drying at 40 °C for 5 h, the cleaned CNWF samples were soaked in pCA solution (2 mg L^{-1}, pH 7.0) under stirring at room temperature for 24 h to form a pCA layer on the CNWF surface. The samples were then washed with DI water three times. The pCA-modified CNWF (pCA@CNWF) was obtained after drying at 40 °C for 6 h.

4.2.5 Preparation of superhydrophobic PDMS-pCA@CNWF

The targeted superhydrophobic PDMS-pCA@CNWF was prepared using a simple dip-coating method. First, PDMS was mixed with THF (10:1, v:v) and stirred at room temperature to form a homogeneous PDMS solution. Subsequently, the pCA@CNWF was immersed in the PDMS solution for 30 min and cured at 70 °C for 12 h in an oven to complete the PDMS curing. The resultant composite was named PDMS-pCA@CNWF for subsequent experiments.

4.2.6 Oil adsorption capacity and oil/water separation property of PDMS-pCA@CNWF

To determine the oil adsorption capacity of the PDMS-pCA@CNWF, 10 g solvents (THF, DMF, Chloroform, and Hexane) and 150 mL water were added to a 200 mL beaker, and then 0.05 g of the PDMS-pCA@CNWF was placed in the mixture. After 5 min, the film was taken out.[32] The droplets suspended outside the adsorbent were air-dried. The adsorption capacity was calculated using Eq. (2):

$$\boldsymbol{q} = \frac{\boldsymbol{m_1 - m_0}}{\boldsymbol{m_0}}\ (2)$$

where q (g g^{-1}) is the adsorption capability of the film, m_0 (g) and m_1 (g) are the weights of the samples before and after adsorption, respectively.

The oil/water separation property of the superhydrophobic PDMS-pCA@CNWF was evaluated using a series of 100 mL 1:1 (v:v) oil/water mixtures. For better observation, the water and oil phases were colored with methylene blue (MB) and Oil Red O, respectively. Four different organic solvents: hexane, DMF, THF, and chloroform, were selected for the oil phase. The separated liquids were collected to determine the separation efficiency. Each measurement was performed three times and an average was calculated.[33] The separation efficiency (E) of the PDMS-pCA@CNWF for various mixtures was calculated using Eq. (3):

$$\boldsymbol{E = \frac{m_1}{m_0} \times 100\% \ (3)}$$

where m_0 and m_1 represent the weight of the oil before and after separation, respectively.

4.2.7 Mechanical durability and chemical stability of PDMS-pCA@CNWF

Mechanical durability of the superhydrophobic PDMS-pCA@CNWF was investigated using a sandpaper abrasion test. PDMS-pCA@CNWF was dragged in one direction on sandpaper (20 cm length, 5 cm s^{-1}) under a 200 g weight. The water contact angle (WCA) of the samples was measured five times and an average was calculated. WCA of the samples was determined every 10 min.

PDMS-pCA@CNWF samples were immersed in various organic solvents (DMF, THF, hexane, and chloroform) and aqueous solutions with different pH values (pH 1, 5, 7, 9, and 13) for 24 h. After that, the treated PDMS-pCA@CNWF was washed with DI water and then dried in an oven at 80 °C. Subsequently, the chemical stability of each sample was determined by WCAs and SEM images.

4.2.8 Characterization

The pCA powder was analyzed using a Tosoh GPC-8020 apparatus with DMF containing 0.10 M LiCl as the solvent, and the flow rate was 1.0 mL min^{-1} at 40 °C. Calibration curves were obtained using poly(ethylene oxide) as the standard. UV spectra of catechin and pCA were recorded on a UV-vis spectrophotometer (U-2810, Hitachi, Tokyo, Japan). FTIR measurements of the samples were recorded in the range of 4000–500 cm^{-1} at a resolution of 1 cm^{-1} using a Nicolet iS5 spectrometer (Thermo Scientific, MA, USA) equipped with an iD5 ATR attachment.

The surface morphology of the CNWF, pCA@CNWF, and PDMS-pCA@CNWF was observed by SEM (SU3500; Hitachi, Tokyo, Japan) at an accelerating voltage of 15 kV. Before analysis, the CNWF, pCA@CNWF, and PDMS-pCA@CNWF were dried and coated with a gold layer using an MSP-1S (Vacuum Device Inc., Tokyo, Japan). The WCAs of the different PDMS-pCA@CNWF samples were determined using a Drop Master DM300 (Kyowa Interface Science, Saitama, Japan). A water droplet (1.0 mL) was dropped onto the surface of the samples (1 cm × 4 cm), and the contact angle of each film was determined at five different positions. The average values are reported. The surface chemical compositions of CNWF and PDMS-pCA@CNWF were determined using XPS (JEOL JPS-9010MC, Tokyo, Japan). The XPS inert parameters included the power of analysis (wide: 75 W, narrow: 150 W) and monochromatic Al Kα radiation.[34] The survey and high-resolution XPS spectra were obtained at fixed analyzer pass energies of 160 eV and 10 eV, respectively. Peak-differentiation analysis was performed using the CasaXPS Version 2.3.15 computer software.

4.3 Results and discussion

4.3.1 Enzymatic Polymerization of Catechin

pCA was synthesized through a simple laccase-catalytic method by polymerization of catechin (**Scheme 4-1**), which is because laccase is highly active for the oxidative polymerization of phenolic compounds.[35] The molecular weight of the pCA was estimated by size exclusion chromatography (SEC) with DMF containing 0.10 M LiCl as the eluent. The number-average molecular weight (Mn) and polymer dispersity index (PDI) was 3,419 and 2.0, respectively.

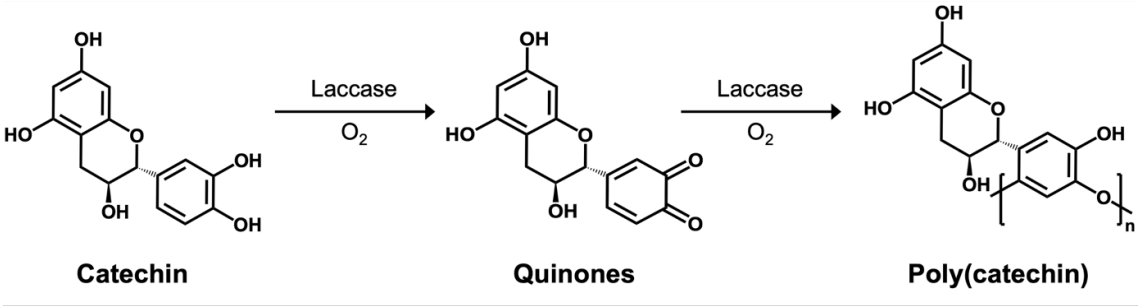

Scheme 4-1. Schematic representation of the polymerization of catechin.

Figure 4-1a shows the FT-IR spectra of catechin and pCA. The peak pattern of pCA is similar to that of catechin, although all the peaks became broader. In the pCA spectrum, the peak at 3300 cm^{-1} is attributed to the vibration of the O–H linkage of phenolic and hydroxyl groups. The peak at 1570 cm^{-1}, distributed to the C=C vibration of the aromatic group, is also observed. According to the literature,[36,37] peaks at 3390, 1602, and 1065 cm^{-1} are attributed to the characteristic functional groups of polyflavonoids. The peak at the range of 1310–1390 cm^{-1} distributed to phenol group (–C–OH) deformation vibrations.

The UV-vis spectra of catechin and pCA are shown in **Figure 4-1b**. Peaks at 280 nm in both catechin and pCA were due to the π–π* transitions of the aromatic fragment appearing. A new large broad peak was appearing in the spectrum of pCA at 370 nm, which indicated the occurrence of catechin polymerization in the enzyme environment.[38] Along with an increase in the basic nature of the reaction environment, the speed and intensity of the appearance of the

polymerization product increased.

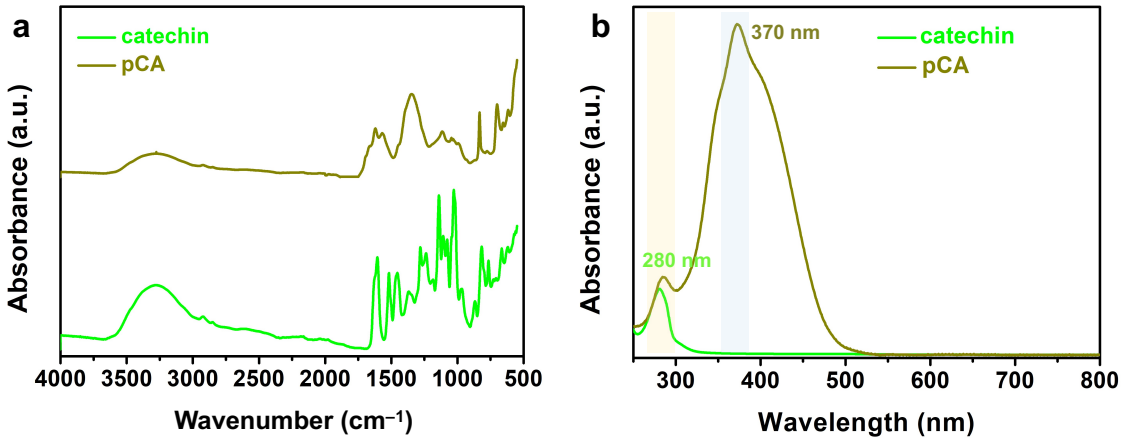

Figure 4-1. (a) FTIR spectra of catechin and pCA powders. (b) UV-vis spectra of catechin and pCA in methanol.

The antioxidant activity of pCA was evaluated using the DPPH method, which is based on the quenching of synthetic-free radicals. In this method, the purple active radical is reduced by antioxidants present in the test sample to a yellow product. As shown in **Figure 4-2a**, at a powder weight of 20 μg mL^{-1}, the DPPH radical scavenging activity of the pCA was 95%, whereas that of the catechin was 90%. Meanwhile, the DPPH radical scavenging activity of the pCA was consistently higher than that of the catechin, irrespective of the reaction time (**Figure 4-2b**). These results suggest that pCA possesses more potent radical scavenging activity than catechin.

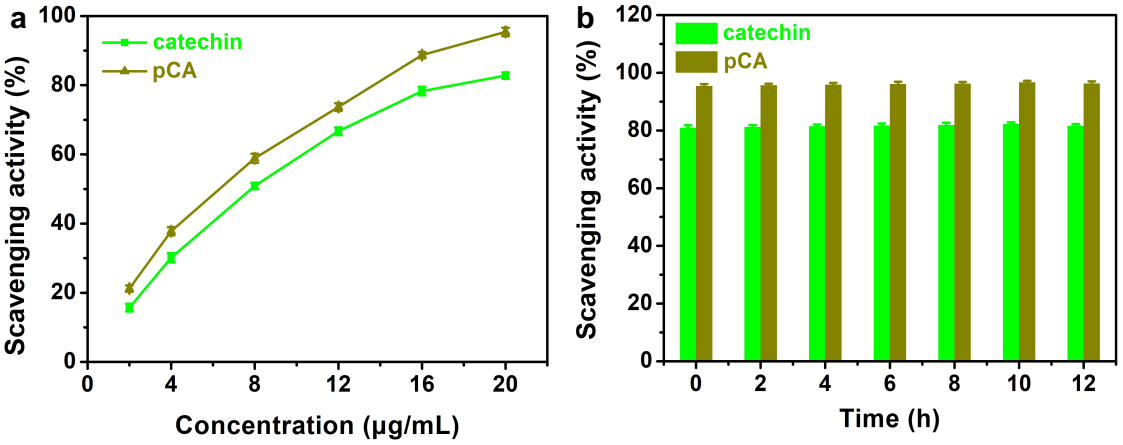

Figure 4-2. Antioxidant assessment of the catechin and pCA depending on the (a) concentration and (b) time. Each value represents the mean ± standard deviation (SD) (n = 3).

4.3.2 Preparation of superhydrophobic PDMS-pCA@CNWF

After the successful preparation of pCA, a modified CNWF (pCA@CNWF) with high antioxidant and antibacterial activity was obtained. Then, the targeted superhydrophobic CNWF (PDMS-pCA@CNWF) for oil/water separation was prepared. Subsequently, the silanol groups from hydrolysis PDMS was reacted with the hydroxyl groups from pCA@CNWF to form a covalently bonded and robust hydrophobic layer through condensation (**Figure 4-3a and 4-3b**).

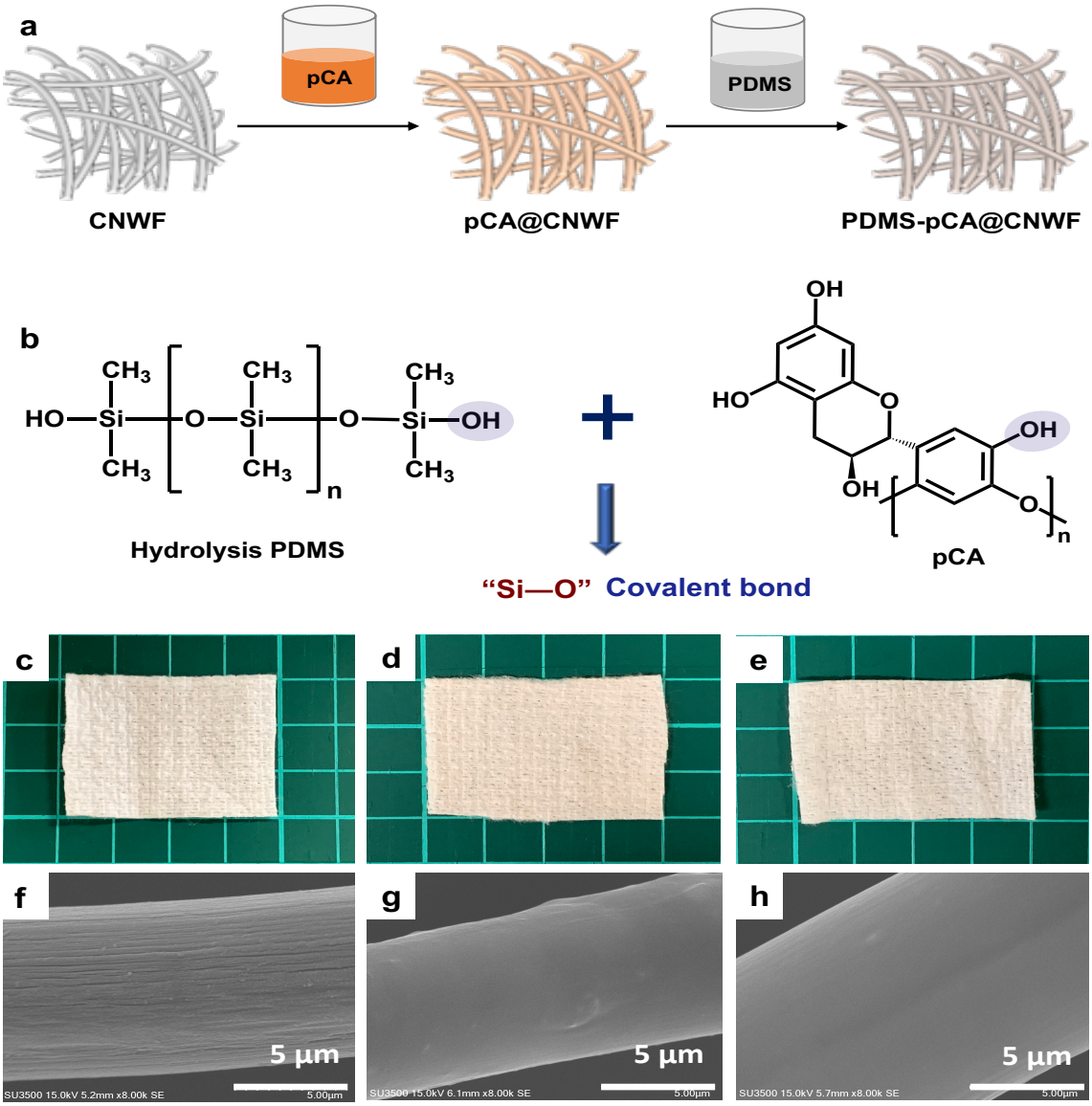

Figure 4-3. (a) Fabrication process of PDMS-pCA@CNWF. (b) Mechanism of the reaction between PDMS and pCA@CNWF surface functional groups. Photographs and SEM images of CNWF (c, f), pCA@CNWF (d, g), and PDMS-pCA@CNWF (e, h).

The successfully obtained superhydrophobic PDMS-pCA@CNWF was confirmed by SEM, FTIR, XPS, and WCA measurements. First, SEM measurements were attituded to characterize the morphological structure of the samples. **Figure 4-3c-3h** shows the surface morphology of the samples. **Figure 4-3f** shows a typical image of the CNWF with an average diameter of approximately 9.1 μm. The pCA@CNWF is shown in **Figure 4-3g**, and its diameter is 8.3 μm. The surface morphology of pCA@CNWF changed after being coated with PDMS (**Figure 4-3h**), resulting in a diameter of 12.3 μm. PDMS coatings uniformly cover the pCA@CNWF wires, and almost no PDMS is present in the pores, which ensures that water can pass freely through the prepared PDMS-pCA@CNWF.

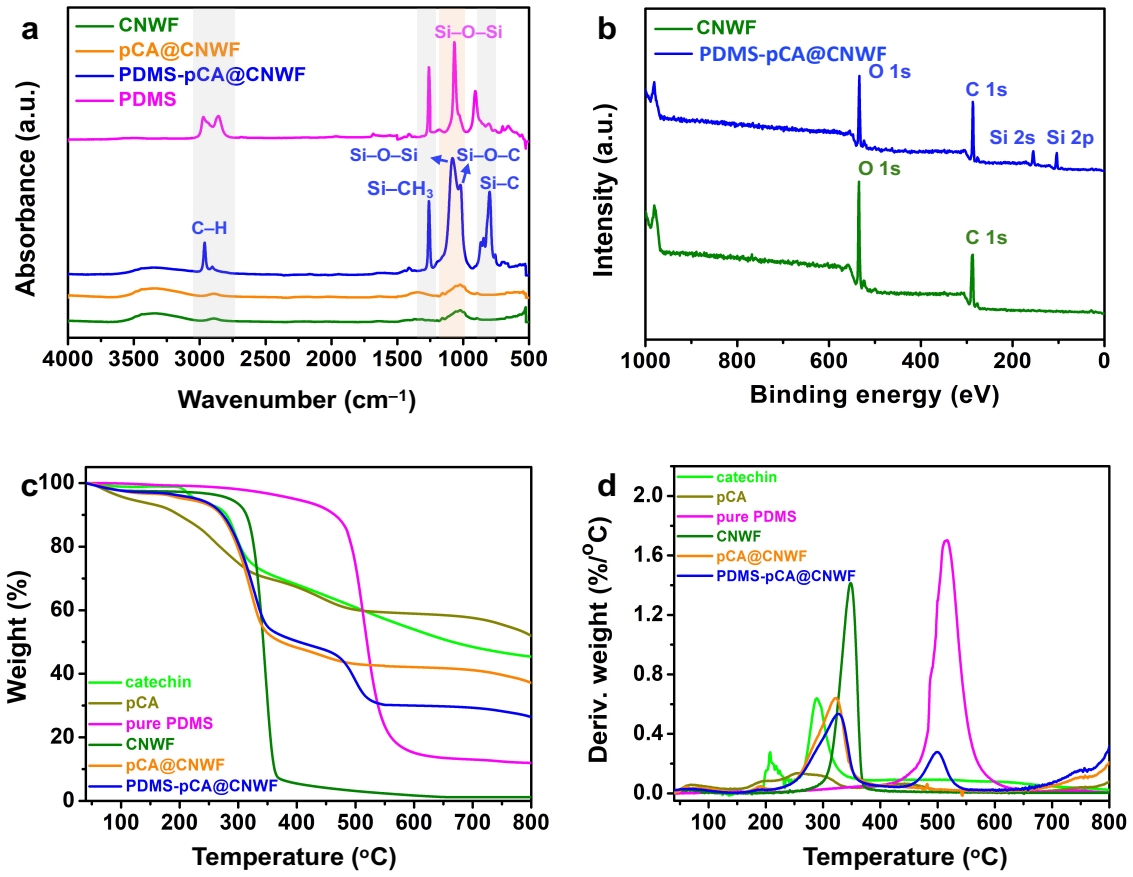

Figure 4-4. (a) Fabrication process of PDMS-pCA@CNWF. (b) Mechanism of the reaction between PDMS and pCA@CNWF surface functional groups. Photographs and SEM images of CNWF (c, f), pCA@CNWF (d, g), and PDMS-pCA@CNWF (e, h).

The surface chemical composition of the samples was investigated by FTIR. As shown in **Figure 4-4a**, peaks at 1023 and ~3400 cm^{-1} in the spectra of the CNWF and pCA@CNWF are

assigned to C–O–C and the O–H stretching vibration, respectively. PDMS-pCA@CNWF shows a peak at 1068 cm^{-1}, indicating the existence of Si–O–C bonds, while the PDMS spectrum shows a peak at 1081 cm^{-1}, which is the Si–O–Si bonds.[39] These results indicate that the hydrolyzed PDMS can be coated on the pCA@CNWF to form the PDMS-pCA@CNWF.

The chemical composition of the resultant PDMS-pCA@CNWF was examined by XPS measurements. As shown in **Figure 4-4b**, in addition to peaks for C (284.8 eV) and O (102.3 eV),[40,41] characteristic peaks for Si can be seen for the PDMS-pCA@CNWF spectrum when compared to that of the CNWF. The peaks at 102.3 eV and 152.0 eV are attributable to Si 2p and Si 2s from PDMS.[42,43] Therefore, these results indicate the successful deposition of PDMS on the pCA@CNWF surface.

Thermal stabilities of the samples were also analyzed, as shown in **Figures 4-4c** and **4d**, catechin and pCA exhibit similar curves. Lispergure et al. [44] reported that the complex aromatic structure of naturally condensed catechin-tannins results in high thermal resistance. The decomposition of Acacia dealbata tannin is almost complete at a temperature of 600 °C, and the remaining weight of tannin is approximately 44%. The weight of pCA at 600 °C was approximately 59% and that of the reference, catechin, was approximately 54%. Therefore, pCA has higher thermal stability with a comparison of natural tannin. The weight loss of the CNWF commences at 285 °C and stops at 373 °C, and the weight at 800 °C is near 0%. Compared with pCA@CNWF and PDMS-pCA@CNWF, it can be stated that both pCA@CNWF (37.3%) and PDMS-pCA@CNWF (26.3%) have higher thermal stability than CNWF.

4.3.3 Oil/water separation using PDMS-pCA@CNWF

The obtained PDMS-pCA@CNWF exhibited superhydrophobicity, which was indicated in **Figure 4-5a and 5b (inset)**. Therefore, it was expected to display excellent oil/water separation. **Figure 4-5a and 5b** shows that PDMS-pCA@CNWF can selectively adsorb oil solvents from oil-water mixtures containing Oil Red O-stained n-hexane or chloroform. As

expected, hexane and chloroform can be completely absorbed by PDMS-pCA@CNWF within a few seconds as they are superoleophilic and superhydrophobic, leaving clean and transparent water. The same results were also observed for MB-stained hexane and MB-stained chloroform mixtures. The same separation process was tested for various mixtures of DMF/water and THF/water, and the results were as good as those for the chloroform/water mixture. The adsorption capacities of the PDMS-pCA@CNWF for various oil solvents were also measured, as shown in **Figure 4-5c**. The adsorption capacities for hexane, THF, chloroform, and DMF were 15.4 g g^{-1}, 20.6 g g^{-1}, 22.4 g g^{-1}, and 21.1 g g^{-1}, respectively. The comparison with other materials reported for oil/water separation in **Table 4-1** indicates that the PDMS-pCA@CNWF in this study has the highest oil absorption capacity. Thus, it can be concluded from the above results that PDMS-pCA@CNWF can be employed as a new environmentally friendly material to achieve highly effective oil/water separation.

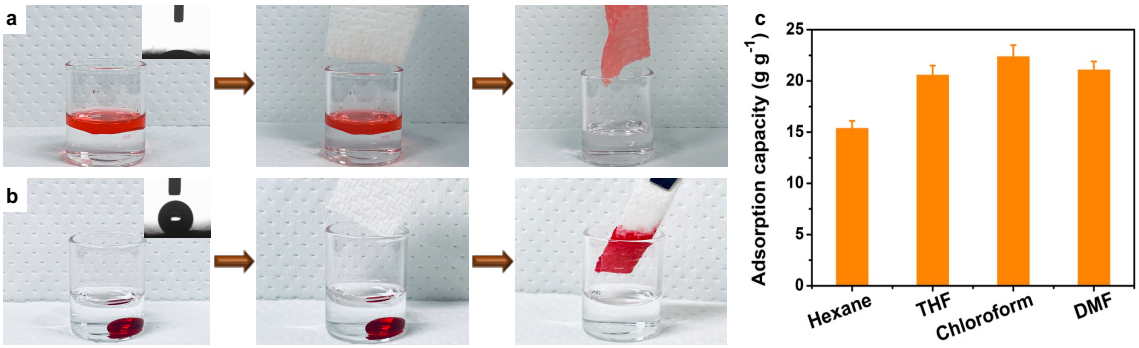

Figure 4-5. Photographs of selective absorption of the PDMS-pCA@CNWF for Oil Red O-stained (a) hexane and (b) chloroform in oil/water mixtures. (c) Adsorption capacities of PDMS-pCA@CNWF for different oil solvents.

Table. 4-1. Summary of the oil adsorption capacities of various adsorbents.

Samples	Oil adsorption capacity (g g^{-1})	Ref.
Polydivinylbenzene nanofibres	7.5	[45]
Alkenylsuccinic anhydride modified wood-based fibers	6	[46]
Cotton fibers grafted with dialkyl substituted silyl ethers	18	[47]
Polyvinyl alcohol nanofiber membranes	12.7	[48]
Raw cotton fiber	15	[49]
PDMS-pCA@CNWF	22.4	This work

The oil/water separation efficiencies of the samples were calculated and are presented in **Figure 4-6a**. The results of the PDMS-pCA@CNWF for the mixtures were always above 94.5%. However, the separation efficiency did not reach 100%, which is mainly attributed to the adsorption capacity of the superhydrophobic PDMS-pCA@CNWF for the oils.

4.3.4 Durability and self-cleaning property of PDMS-pCA@CNWF

To improve the durability of the PDMS-pCA@CNWF, solvent damage and mechanical forces during use were investigated. As an important criterion for practical applications, the long-term superhydrophobic durability of the prepared PDMS-pCA@CNWF was also investigated under various rigorous conditions. The thickness of all the samples is also summarized in **Table 4-2**. There were no significant differences in the thickness of all samples except for pH 9 and pH 13. PDMS was easily soluble in an alkaline environment, meanwhile, pCA was also unstable under these conditions. Thus, the reaction between PDMS and pCA was disrupted and further affecting the surfaces of samples, which resulted that the sample thickness decreased. The chemical resistance of the PDMS-pCA@CNWF was evaluated by immersing it in an extremely chemical environment. As shown in **Figures 4-6b and 6c**, WCAs were in the range 142° to 151° after the PDMS-pCA@CNWF samples were immersed in various organic solvents and aqueous solutions with different pH for 24 h, exhibiting desirable superhydrophobicity. Notably, the WCAs of the samples treated with strong alkali solutions and hexane were decreased, which can be attributed to the slight hydrolyzation and dissolution of PDMS under these conditions. However, even after exposure to hexane, PDMS-pCA@CNWF was still capable of achieving oil/water separation. To investigate the effect of mechanical properties on the robustness of samples, an abrasion test was conducted. With an increase in the number of abrasion cycles, the WCA of PDMS-pCA@CNWF was decreased (**Figure 4-6d**). However, it remained at approximately 110° even after 50 abrasion cycles, exhibiting durable hydrophobicity. It can be concluded from the results of mechanical and chemical durability tests that the superhydrophobic PDMS-pCA@CNWF displayed excellent stability in extremely harsh environments.

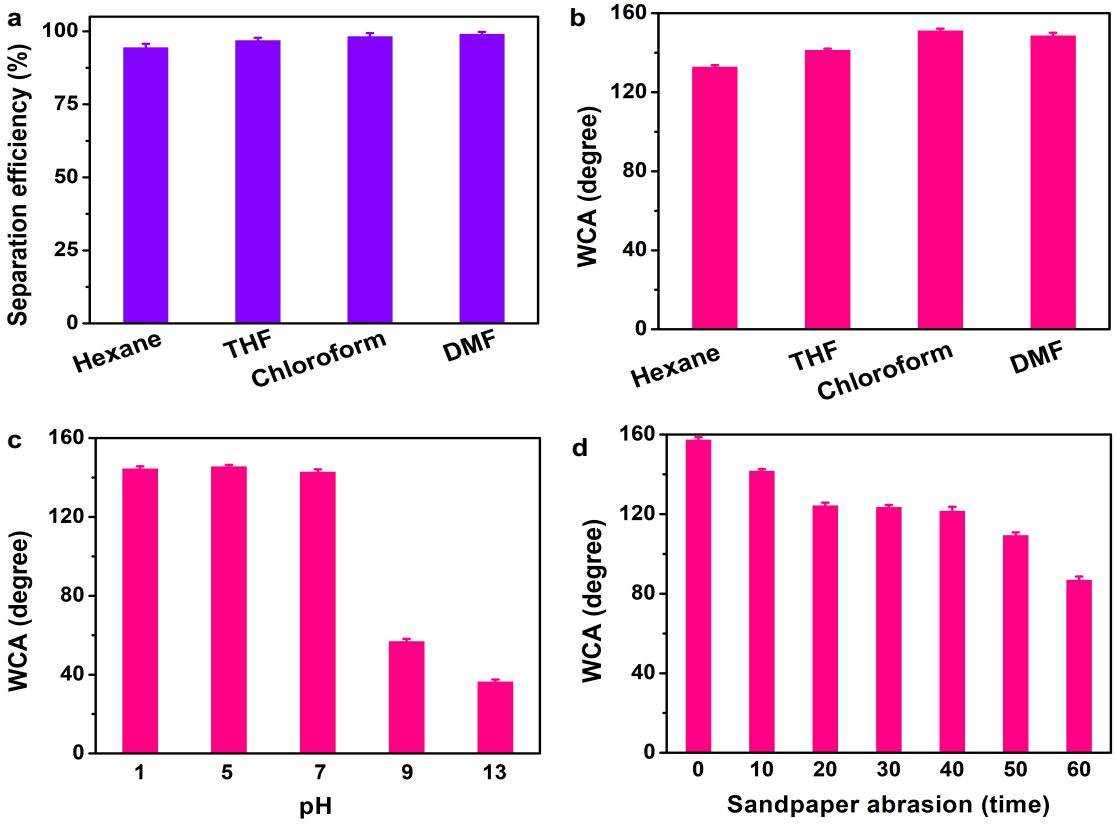

Figure 4-6. (a) Separation efficiency of different oil/water mixtures using superhydrophobic PDMS-pCA@CNWF. The water contact angle of different solvents (b), pH (c), and abrasion time using sandpaper (d) of PDMS-pCA@CNWF.

Table. 4-2. Summary of the oil adsorption capacities of various adsorbents.

Samples	Thickness[a] (µm)
CNWF	1066 ± 2.1
pCA@CNWF	1059 ± 3.0
PDMS-pCA@CNWF	1068 ± 3.5
PDMS-pCA@CNWF (Hexane)	1027 ± 3.8
PDMS-pCA@CNWF (THF)	1049 ± 4.1
PDMS-pCA@CNWF (Chloroform)	1058 ± 2.1
PDMS-pCA@CNWF (DMF)	1056 ± 2.3
PDMS-pCA@CNWF (pH 1)	1051 ± 2.5
PDMS-pCA@CNWF (pH 5)	1055 ± 2.6
PDMS-pCA@CNWF (pH 7)	1049 ± 2.7
PDMS-pCA@CNWF (pH 9)	887 ± 3.1
PDMS-pCA@CNWF (pH 13)	721 ± 4.6

[a]Values are shown as the mean ± standard deviation (SD) (n = 3).

The surface self-cleaning properties of PDMS-pCA@CNWF and CNWF were compared. The performance was verified using MB powder as a model contaminant. MB powders are randomly distributed on the surface of the pristine and modified CNWFs, which were tightly adhered to the glass slides (**Figures 4-7a** and **7c**). For PDMS-pCA@CNWF (**Figure 4-7d**), when waters were dropped to the MB-contaminated sample, the powders were immediately removed and the surface of PDMS-pCA@CNWF remained clean. In contrast, for CNWF, the MB powder immediately dissolved in the water and then contaminated its surface, leaving a blue trace (**Figure 4-7b**). A schematic diagram of this process is shown in **Figure 4-7e**. The results demonstrate the excellent self-cleaning property of PDMS-pCA@CNWF due to its high-water surface tension and low surface energy, which plays an essential role in the anti-fouling behavior.

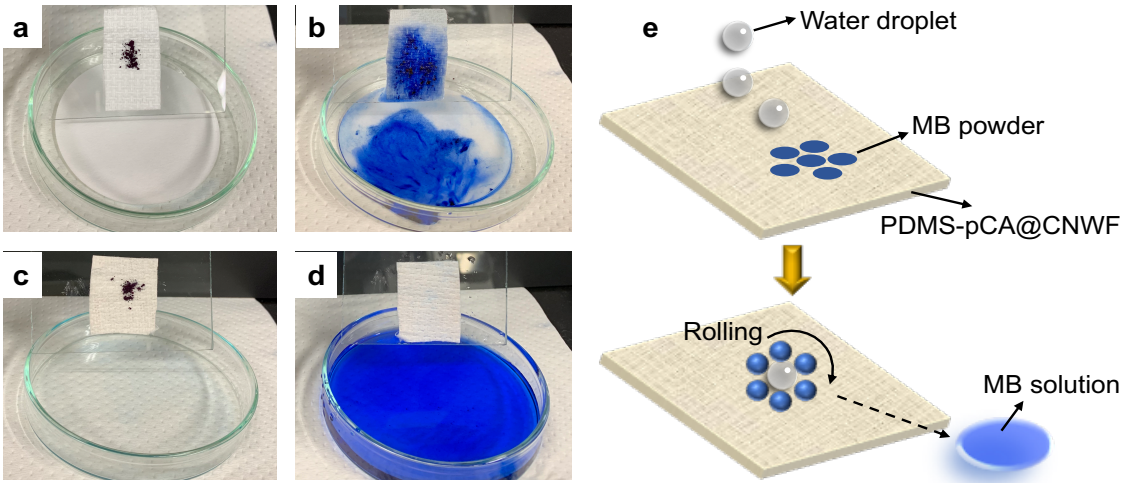

Figure 4-7. Self-cleaning of MB powder on the surface of CNWF (a, b) and PDMS-pCA@CNWF (c, d). (e) Schematic of the self-cleaning activity of PDMS-pCA@CNWF.

4.4 Conclusions

In summary, a facile and feasible approach for highly efficient oil/water separation was developed. The antioxidant PDMS-pCA@CNWF with self-cleaning properties enhances UV resistance and is proven as an environmentally friendly material for oil in oil/water mixtures (both light and heavy oils). Owing to the presence of pCA, it has high antioxidant activity, making it less susceptible to the influence of ultraviolet light and improving its stability. Due to the excellent flexibility of the CNWF, the material can be easily recycled by extrusion. In all cases, the synthetic DMS-pCA@CNWF has an oil separation efficiency of greater than 94% for all types of oil. The WCA of PDMS-pCA@CNWF remained at approximately 110° after 50 abrasion cycles, exhibiting durable hydrophobicity. More importantly, this hybrid material (PDMS-pCA@CNWF) can be applied in a variety of complex environments, particularly in strongly acidic environments, demonstrating its potential application in practical situations. The present strategy provides a simple method to fabricate a novel environmentally friendly superhydrophobic material with low cost and high efficiency in oil-water mixtures separation studies. This research result breaks through the bottleneck of traditional oil/water separation technologies and has broad application prospects.

4.5 References

1. Q. Lin, G. Zeng, G. Yan, *Chem. Eng. J.*, 2022, **427**, 131668.
2. Y. Shen, D. Li, L. Wang, *ACS Appl. Mater. Interfaces.*, 2021, **13**, 20489–20500.
3. R. Gupta, G. Dunderdale, M. England, *J. Mater. Chem. A.*, 2017, **5**, 16025–16058.
4. Y. Wei, G. Liu, J. Luo, *Front. Chem. Sci. Eng.*, 2021, **15**, 717–719.
5. Z. Guo, B. Long, S. Gao, *J. Hazard. Mater.*, 2021, **402**, 123838.
6. X. Gou, Y. Zhang, L. Long, *Colloids Surf. A Physicochem. Eng. Asp.*, 2020, **605**, 125338.
7. W. Zhang, N. Liu, Y. Cao, *Adv. Mater. Interfaces.*, 2017, **4**, 1600029.
8. S. Yan, Y. Li, F. Xie, *ACS Sustain. Chem. Eng.*, 2020, **8**, 5347–5359.
9. C. Chen, D. Weng, A. Mahmood, *ACS Appl. Mater. Interfaces.*, 2019, **11**, 11006–11027.
10. S. Zhao, Y. Liang, Y. Yang, *Nanoscale*, 2021, **13**, 15334–15342.
11. M. Padaki, R. Murali, M. Abdullah, *Desalination*, 2015, **357**, 197–207.
12. N. Junaidi, N. Othman, N. Fuzil, *Sep. Purif. Technol.*, 2021, **258**, 118000.
13. H. Zhan, T. Zuo, R. Tao, *ACS Sustain. Chem. Eng.*, 2018, **6**, 10833–10840.
14. Y. Zhu, J. Wang, F. Zhang, *Adv. Funct. Mater.*, 2018, **28**, 1804121.
15. J. Ou, W. Hu, M. Xue, *ACS Appl. Mater. Interfaces.*, 2013, **5**, 3101–3107.
16. W. Ma, Y. Ding, M. Zhang, S. Gao, Y. Li, *J. Haz-ard. Mater.*, 2020, **384**, 121476
17. D. Yuan, T. Zhang, Q. Guo, F. Qiu, *Ind. Eng. Chem. Res.*, 2018, **57**, 14758–14766.
18. L. Boinovich, A. Emelyanenko, ACS *Appl. Mater. Interfaces.*, 2015, **7**, 19500–19508.
19. K. Nayak, B. Tripathi, *Sep. Purif. Technol.*, 2021, **259**, 118068.
20. Z. Wang, Y. Wang, G. Liu, *Angew. Chem.*, 2016, **128**, 1313–1316.
21. Y. Chen, L. Zhang, C. Mei, *ACS Appl. Mater. Interfaces.*, 2020, **12**, 35513–35522.
22. H. Abdelhamid, A. Mathew, *Chem. Eng. J.*, 2021, **426**, 131733.
23. Z. Wang, Y. Wang, G. Liu, *Angew. Chem.*, 2016, **128**, 1313–1316.
24. P. Pi, K. Hou, X. Wen, *Prog. Org. Coat.*, 2016, **101**, 522–529.
25. J. Zhang, M. Zhang, C. Yang, *Adv. Mater.*, 2014, **26**, 4121–4126.
26. P. Wei, H. Lou, X. Xu, *Appl. Surf. Sci.*, 2021, **539**, 148195.

27. B. Jalvo, A. Aguilar, M. Ruiz, *Nanomaterials*, 2021, **11**, 1752.

28. Y. Zhao, X. Yang, L. Yan, *J. Membr. Sci.*, 2021, **618**, 118525.

29. S. Suner, M. Sahiner, S. Mohapatra, *Int. J. Polym. Maters*., 2021, **2021**, 1–12.

30. M. Kurisawa, J. Chung, H. Uyama, *Macromol Biosci.*, 2003, **3**, 758–764.

31. H. Wen, Y. Hsu, T. Asoh, *J. Mater. Sci.*, 2021, **56**, 12224–12237.

32. L. Wang, S. Dai, X. Liu, *Appl. Sci.*, 2019, **1**, 1–12.

33. Y. Jia, H. Asahara, Y. Hsu, *Appl. Surf. Sci.*, 2020, **530**, 147202.

34. Y. Lu, T. Chen, N. Mkhize, *ACS nano*, 2021, **15**, 19570-19580..

35. C. Zhang, J. Xue, X. Yang, *Prog. Polym. Sci.*, 2022, **125**, 101473.

36. L. Biao, S. Tan, Q. Meng, *Nanomaterials*, 2018, **8**, 53.

37. M. Kurisawa, J. Chung, Y. Kim, *Biomacromolecules*, 2003, **4**, 469–471.

38. Q. Wu, Y. Ouyang, Y. Kong, *J. Agric. Food Chem.*, 2021, **69**, 8807–8818.

39. X. Chen, F. Wen, Z. Liu, *Mater. Des.*, 2021, **207**, 109852.

40. B. Zhang, J. Duan, Y. Huang, *J Mater Sci Technol.*, 2021, **71**, 1–11.

41. L. Bauman, D. Sameoto, *Colloids Surf. A Physicochem. Eng. Asp.*, 2021, **610**, 125901.

42. D. Tantraviwat, M. Ngamyingyoud, W. Sripumkhai, *ACS omega*, 2021, **6**, 29765–29773.

43. Y. Li, Z. Luo, G. Li, *Green Chem.*, 2021, **23**, 4181–4190.

44. J. Lisperguer, Y. Saravia, E. Vergara, *J. Chil. Chem. Soc.*, 2016, **61**, 3188–3190.

45. X. Zhu, X. Wang, Y. Liu, *J. Chem. Technol. Biotechnol.*, 2019, **94**, 128–135.

46. K. Payne, C. Jackson, C. Aizpurua, *Environ. Sci. Technol.*, 2012, **46**, 7725–7730.

47. K. Jarrah, S. Hisaindee, M. Sayah, *Cellulose*, 2018, **25**, 4093–4106.

48. J. Ge, G. Wu, S. Yoon, *Nanomaterials*, 2021, **11**, 2514.

49. F. Liu, M. Ma, D. Zang, *Carbohydr. Polym.*, 2014, **103**, 480–487.

Concluding Remarks

In this doctoral thesis, GTE-based multifunctional composite materials were developed by using the functional groups from GTE. These functional composite materials showed high antioxidant activity, photocatalytic degradation property, and antifouling property to adapt to the external environment. Most importantly, the developed GTE-based multifunctional composite materials exhibited excellent good biodegradability and biocompatibility.

In Chapter 1, the author focused on the preparation and characterization of biocomposite films consisting of PVA and GTE with a small amount of glycerol as a plasticizer. The incorporation of GTE could considerably alter the optical and mechanical properties of the pure PVA film. Notably, the GTE-PVA biocomposite films presented better water vapor and UV-vis light barrier properties and higher mechanical strength than the pure PVA film. The GTE-PVA biocomposite films showed higher antioxidant activity than the pure PVA film, and the antioxidant activity increased with increasing GTE concentration. The color of the GTE-PVA biocomposite films became yellow when the pH was lower than 6 and became dark red when the pH was higher than 6. Moreover, color variations were observed in the GTE-PVA biocomposite films by changing the pH. These results suggest that GTE-PVA composite films may be used as a promising antioxidants and visible pH-sensing food packaging materials.

In Chapter 2, a simple and eco-friendly method for the synthesis and immobilization of AgNPs onto functional films using green tea extract as a reducing and capping agent has been reported. The freestanding flexible immobilized AgNPs composite was obtained from a TEMPO-mediated TTC process. SEM analysis revealed the homogeneous coating of the AgNPs on the surface of the TTC nanofibers. Ag-TTC-PVA composite film was prepared through a simple solvent casting method, which displayed higher antioxidant activity than the TTC-PVA film, and the rate of release of Ag was reduced owing to the immobilized AgNPs. The photocatalytic performance of Ag-TTC-PVA composite film was evaluated along with the investigations of the optical transparency, morphology, and thermal properties. Ag-TTC-PVA composite film showed enhanced photocatalytic properties than TTC-PVA film. This study

presents a simple approach for the green synthesis of materials with controlled leakage based on Ag-TTC-PVA composite film, which has good potential application prospects in the development for the photocatalytic degradation of certain toxic dyes, thereby paving the way for waste treatment.

In Chapter 3, a new functional PMMA antifouling film has been developed. For this purpose, the surface of a PMMA film was modified by PEI and grafted with strongly hydrophilic PEtOx-GA. PEtOx-GA was synthesized with high efficiency in the presence of $Yb(OTf)_3$ as a catalyst. GA in PEtOx-GA has functional groups that can react with the PEI-S to form the functional film (PEtOx-GA-PEI-S) via Schiff-base and Michael addition reactions. The PEtOx-GA-PEI-S functional film prevented protein adsorption, as demonstrated by water contact angle testing and an adsorption experiment with BSA protein, and the mass of adsorbed BSA was reduced by ~70%. This study indicates that PEtOx-GA-PEI-S functional film is a highly promising candidate for biomedical antifouling applications.

In Chapter 4, a new membrane with super hydrophobicity was synthesized by a facile, green, and low-cost method. First, cellulose non-woven fabric (CNWF) was modified by poly(catechin) (pCA), which has good antioxidant and antibacterial activities, to make it unaffected by UV light and improve the stability of the structure. Then, hydrolyzed polydimethylsiloxane (PDMS) was coated on the pCA@CNWF surface via chemical bonding to make the composite hydrophobic. This durable superhydrophobic fabric can be used to separate various oil/water mixtures by gravity-driven forces with high separation efficiency (over 98.9%). Additionally, the PDMS-pCA@CNWF possesses the advantages of flexibility, high efficiency, and outstanding self-cleaning performance and demonstrates significant potential for applications in various environments even under various harsh conditions, which make it very promising for the treatment of oil pollution in practical applications.

In summary, numerous strategies were developed to achieve GTE-based multifunctional composite materials: The first one utilized the GTE as the antioxidants and pH indicators to cross-linked with PVA through hydrogen bonds to make multifunctional composite materials, which employed to produce biodegradable and environment-friendly packaging films. The

second one used GTE as a reducing agent of metal ions, leading to the formation of capping AgNPs. In order to expand the application of AgNPs in the food field, the effective approach to prevent AgNPs aggregation and control its release is the immobilization of AgNPs on the TTC. Most importantly, the obtained Ag-TTC-PVA composite film possesses superior biodegradability and biocompatibility. The third one used gallic acid as the sustainable scaffold synthesized with PEtOx polymer, then grafted to the modified PMMA film surface via Schiff-base and Michael addition reactions. This functional film could prevent different pI of protein adsorptions. The advantages of materials based on polyphenol groups include the simplicity of the synthesis, the ease of applicability, and the availability of functional groups, the author believes this thesis will open a fresh and universal route to design and synthesize new multifunctional composites. The fourth one makes use of the strong oxidation property of pCA, which is obtained through the laccase-catalyzed polymerization method, and CNWF modified with pCA can be unaffected by UV light and has improved structural stability. Subsequently, the superhydrophobic material PDMS-pCA@CNWF was obtained by the condensation reaction between modified CNWF and hydrolysis PDMS. This superhydrophobic material possesses the advantages of flexibility, high efficiency, and outstanding self-cleaning performance and demonstrates significant potential for applications in various environments even under various harsh conditions, which make it very promising for the treatment of oil pollution in practical applications.

List of Publications

1. Antioxidant activity and physical properties of pH-sensitive biocomposite using poly(vinyl alcohol) incorporated with green tea extract

Hanyu Wen, Yu-I Hsu*, Taka-Aki Asoh, and Hiroshi Uyama*

Polymer Degradation and Stability, **2020**, *178*, 109215.

2. Poly(vinyl alcohol)-based composite film with Ag-immobilized TEMPO-oxidized nano-tea cellulose for improving photocatalytic performance

Hanyu Wen, Yu-I Hsu*, Taka-Aki Asoh, and Hiroshi Uyama*

Journal of Materials Science, **2021**, *56*, 21, 12224-12237.

3. Superhydrophobic PDMS-pCA@CNWF composite with UV-resistant and self-cleaning properties for oil/water separation

Hanyu Wen, Yu-I Hsu*, and Hiroshi Uyama*

Materials, **2022**, *15*, 1, 376

4. Poly(methyl methacrylate) surface grafted with poly(2-ethyl-2-oxazoline) using tea polyphenol as linker molecule

Hanyu Wen, Yu-I Hsu*, Taka-Aki Asoh, and Hiroshi Uyama*

Progress in Organic Coatings

Under revision

Acknowledgments

Firstly, I would like to express my sincere gratitude to my advisor Prof. Hiroshi Uyama for the continuous support of my Ph.D. study and related research, for his patience, motivation, and immense knowledge. His guidance helped me in all the time of research and writing of this thesis.

Besides my advisor, I would like to thank the rest of my thesis committee: Prof. Takashi Hayashi and Prof. Norimitsu Tohnai, for their insightful comments and encouragement, but also for the hard question which incented me to widen my research from various perspectives.

I am profoundly grateful to Assoc. Prof. Taka-aki Asoh, for his suggestions and inspirations, to improve the quality of my research. His novel insights and knowledge sharing promoted my thesis' accomplishment. I also thank him for his suggestions and revision about the slides art to make it easier to understand.

I appreciate Assist. Prof. Yu-I Hsu for her discussions and advice about my subject at any time and for the knowledge sharing. I also deeply thank her for the manuscript revising, inspirations, and experience sharing. Without her support, my doctoral thesis cannot be finished smoothly.

I wish to appreciate the kind help and warm-hearted support from Ms. Yoko Uenishi and Ms. Tomoko Shimizu.

I would like to thank all my friends: Dr. Zhaohang Yang, Dr. Masatoshi Kato, Dr. Chen Qian, Dr. Zhengtian Xie, Dr. Yankun Jia, Dr. Toshiki Tamiya, Dr. Shunsuke Mizuno, Ms. Yanting Lyu, Mr. Naharullah Bin Jamaluddin, Mr. Raghav Soni, Mr. Akihide Sugawara, Mr. Mark Adam Malaluan Ferry, Ms. Meng Wei, Mr. Luwei Zhang, Ms. Yan Wang, Mr. Yuxiang Jia and all past and present members of Uyama Laboratory. It was a truly unforgettable experience to study with you.

Last but not least, I would like to express appreciation to my parents Ye Wen and Yiping Ren for supporting me spiritually throughout writing this thesis and my life in general. The warm encouragement from my family motivates me to persist in my research and study. This thesis would not have been possible without their help, love, dedication, and encouragement.

January 2022

WEN HANYU